



University of  
Massachusetts  
Amherst

## **Polymer Composites and Porous Materials Prepared by Thermally Induced Phase Separation and Polymer-Metal Hybrid Methods**

Item Type	dissertation
Authors	Yoon, Joonsung
DOI	<a href="https://doi.org/10.7275/1264661">10.7275/1264661</a>
Download date	2025-01-19 16:18:47
Link to Item	<a href="https://hdl.handle.net/20.500.14394/38603">https://hdl.handle.net/20.500.14394/38603</a>

**POLYMER COMPOSITES AND POROUS MATERIALS PREPARED BY  
THERMALLY INDUCED PHASE SEPARATION AND POLYMER-METAL  
HYBRID METHODS**

A Dissertation Presented

by

JOONSUNG YOON

Submitted to the Graduate School of the  
University of Massachusetts Amherst in partial fulfillment  
of the requirements for the degree of

DOCTOR OF PHILOSOPHY

February 2010

Polymer Science and Engineering

© Copyright by Joonsung Yoon 2010

All Rights Reserved

**POLYMER COMPOSITES AND POROUS MATERIALS PREPARED BY  
THERMALLY INDUCED PHASE SEPARATION AND POLYMER-METAL  
HYBRID METHODS**

A Dissertation Presented

by

JOONSUNG YOON

Approved as to style and content by:

---

Alan J. Lesser, Co-Chair

---

Thomas J. McCarthy, Co-Chair

---

Henning H. Winter, Member

---

Shaw Ling Hsu, Department Head  
Polymer Science and Engineering

## **DEDICATION**

Sung-Eun and Seokjoo

## ACKNOWLEDGMENTS

First of all, I would like to thank my advisors, Prof. Alan Lesser and Prof. Thomas McCarthy. Prof. McCarthy is full of many interesting ideas and I learned from him how to think and how to look at things from different perspectives. Prof. Lesser is well organized and very logical in thinking. He taught me how to put ideas into practice and how to communicate effectively. I am also grateful to Prof. Henning Winter for serving on my committee. He provided me with many suggestions during my work and kindly let me use the rheometer in his lab.

I would like to thank McCarthy group members for helping me in many ways: Sung-In, Jung-Ah, Lichao, Ted, Ebru, Kevin, Ilke, Zhixiang, Jay, Scott, Yufeng, Bokyung, Dalton, Peiwen, Joe and Jack. All of them are really nice and I will miss them a lot. I would like to thank Lesser group members as well: Dr. Xianbo Hu, Kishore, Donna, Kevin, Melissa, Peter, Mohit, Jared, Andrew, Sinan, Kate, Naveen, Ruosty and Henry. We had fun together both inside and outside the lab.

All of the PSE staff are true asset to the department and I really appreciate their kind help to make my life much easier.

Finally, I would like to thank both my parents and parents-in-law for their absolute love and support for me. I thank my sister and my brother for cheering me up in difficult times. My wife, Sung-Eun, and my son, Seokjoo, have always been with me as a loving family. Sung-Eun has supported me with selfless devotion and Seokjoo has been the source of happiness in our family. I thank them for sharing life with me.

## **ABSTRACT**

### **POLYMER COMPOSITES AND POROUS MATERIALS PREPARED BY THERMALLY INDUCED PHASE SEPARATION AND POLYMER-METAL HYBRID METHODS**

FEBRUARY 2010

JOONSUNG YOON, B.S., SEOUL NATIONAL UNIVERSITY

M.S., SEOUL NATIONAL UNIVERSITY

M.S., UNIVERSITY OF MASSACHUSETTS AMHERST

Ph.D., UNIVERSITY OF MASSACHUSETTS AMHERST

Directed by: Professor Alan J. Lesser, Professor Thomas J. McCarthy

The primary objective of this research is to investigate the morphological and mechanical properties of composite materials and porous materials prepared by thermally induced phase separation. High melting crystallizable diluents were mixed with polymers so that the phase separation would be induced by the solidification of the diluents upon cooling. Theoretical phase diagrams were calculated using Flory-Huggins solution thermodynamics which show good agreement with the experimental results.

Porous materials were prepared by the extraction of the crystallized diluents after cooling the mixtures (hexamethylbenzene/polyethylene and pyrene/polyethylene). Anisotropic structures show strong dependence on the identity of the diluents and the composition of the mixtures. Anisotropic crystal growth of the diluents was studied in terms of thermodynamics and kinetics using DSC, optical microscopy and SEM. Microstructures of the porous materials were explained in terms of supercooling and dendritic solidification.

Dual functionality of the crystallizable diluents for composite materials was evaluated using isotactic polypropylene (iPP) and compatible diluents that crystallize upon cooling. The selected diluents form homogeneous mixtures with iPP at high temperature and lower the viscosity (improved processability), which undergo phase separation upon cooling to form solid particles that function as a toughening agent at room temperature. Tensile properties and morphology of the composites showed that organic crystalline particles have the similar effect as rigid particles to increase toughness; de-wetting between the particle and iPP matrix occurs at the early stage of deformation, followed by unhindered plastic flow that consumes significant amount of fracture energy. The effect of the diluents, however, strongly depends on the identity of the diluents that interact with the iPP during solidification step, which was demonstrated by comparing tetrabromobisphenol-A and phthalic anhydride.

A simple method to prepare composite surfaces that can change the wettability in response to the temperature change was proposed and evaluated. Composite surfaces prepared by nanoporous alumina templates filled with polymers showed surface morphology and wettability that depend on temperature. This effect is attributed to the significant difference in thermal conductivity and the thermal expansion coefficient between the alumina and the polymers. The reversibility in thermal response depends on the properties of the polymers.

## TABLE OF CONTENTS

ACKNOWLEDGMENTS .....	v
ABSTRACT .....	vi
LIST OF TABLES .....	xi
LIST OF FIGURES .....	xii
CHAPTER	
1. INTRODUCTION .....	1
1.1. Phase Transformations in Polymer Systems .....	1
1.2. Toughening of Plastics .....	13
1.3. Wetting of Polymers inside Nanoporous Alumina Template .....	18
1.4. Dissertation Overview .....	23
2. LOCALLY ANISOTROPIC POROUS MATERIALS FROM POLYETHYLENE AND CRYSTALLIZABLE DILUENTS .....	25
2.1. Introduction .....	26
2.2. Materials and Sample Preparation .....	27
2.2.1. Materials .....	27
2.2.2. Sample Preparation .....	29
2.3. Experimental .....	31
2.3.1. Thermal Analysis .....	31
2.3.2. Optical Microscopy .....	31
2.3.3. Scanning Electron Microscopy (SEM) .....	32
2.4. Results and Discussion .....	32
2.4.1. Equilibrium Phase Diagrams .....	32

2.4.2. Phase Separation by Crystallization.....	38
2.4.3. Morphology.....	49
2.4.4. Effect of Cooling Conditions .....	53
2.4.5. Effect of the Polymer .....	56
2.5. Conclusions.....	56
3. SELF-REINFORCING ISOTACTIC POLYPROPYLENE PREPARED USING CRYSTALLIZABLE SOLVENTS .....	59
3.1. Introduction.....	59
3.2. Materials and Sample Preparation .....	62
3.2.1. Materials .....	62
3.2.2. Sample Preparation .....	64
3.3. Characterization and Testing .....	65
3.3.1. Thermal Analysis .....	65
3.3.2. Mechanical Characterization .....	66
3.3.3. X-ray Scattering.....	66
3.3.4. Optical Microscopy.....	66
3.3.5. Scanning Electron Microscopy (SEM) .....	67
3.3.6. Viscometry.....	67
3.4. Results and Discussion .....	68
3.4.1. Thermally Induced Phase Separation (TIPS).....	68
3.4.2. Crystallization .....	73
3.4.3. Viscosity .....	81
3.4.4. Morphology of Composites .....	81

3.4.5. Tensile Properties.....	84
3.4.6. Fracture Toughness.....	86
3.4.7. Effect of Diluent Identity.....	99
3.5. Conclusions.....	114
4. THERMALLY ACTIVE COMPOSITE SURFACES USING POLYMER- METAL HYBRID METHODS .....	116
4.1. Introduction.....	117
4.2. Materials and Sample Preparation .....	119
4.2.1. Materials .....	119
4.2.2. Sample Preparation.....	119
4.3. Characterization and Testing .....	122
4.3.1. Microscopy .....	122
4.3.2. Contact Angle Measurements.....	122
4.4. Results and Discussion .....	123
4.4.1. Morphology.....	123
4.4.2. Wettability.....	125
4.5. Conclusions.....	129
APPENDIX ALIGNED STRUCTURES USING A HIGH MELTING IONIC LIQUID (MOLTEN SALT) UNDER AN ELECTRIC FIELD .....	130
BIBLIOGRAPHY.....	148

## LIST OF TABLES

Table	Page
<b>1.1.</b> Self-ordering regimes for anodization of aluminum.....	18
<b>2.1.</b> Materials properties .....	28
<b>3.1.</b> Materials properties .....	63
<b>3.2.</b> Fracture toughness calculated from three point bending test at 50 mm/min crosshead speed.....	91
<b>3.3.</b> Physical properties of phthalic anhydride and TBBPA .....	99
<b>3.4.</b> Qualitative comparison between PA and TBBPA of their effect on material properties of polypropylene-based composites. ....	113
<b>4.1.</b> Materials properties .....	119
<b>A.1.</b> Materials properties.....	133

## LIST OF FIGURES

Figure	Page
<b>1.1.</b> Example of the free energy of mixing for a polymer system at certain fixed temperature. $\chi$ , known as Flory-Huggins interaction parameter, is assumed to be a function of temperature only.....	4
<b>1.2.</b> Straight lines that are tangential to the free energy of mixing curve at two different compositions can be found at different $\chi$ 's.....	5
<b>1.3.</b> L-L demixing as represented by binodal (coexistence) curve .....	6
<b>1.4.</b> Stability of polymer system against fluctuations. The boundary between stable state and unstable state can be found by $\frac{\partial^2}{\partial \phi_2^2} \left( \frac{\Delta F_m}{k_B T} \right) = 0$ . .....	8
<b>1.5.</b> Spinodal curve as constructed from Equation 1.6. ....	9
<b>1.6.</b> Typical phase transition boundary curves and the resulting phase diagram for a mixture of semi-crystalline polymer and crystallizable diluents that show limited miscibility in both liquid phase and solid phase. (a) phase transition boundary curves, (b) equilibrium phase diagram. ....	12
<b>1.7.</b> Change in brittle-ductile transition temperature ( $T_b$ ) under various conditions (known as Davidenkov diagram). $\sigma_Y$ represents yield strength and $\sigma_B$ represents brittle strength. (a) material is brittle at room temperature, (b) material becomes ductile by decreasing deformation rate, (c) material becomes ductile by reducing plastic resistance, (d) material becomes highly brittle by introducing a flaw. ....	14
<b>1.8.</b> Critical ligament thickness that can be used to predict the fracture behavior of the materials. (a) oriented layers of the polymer crystallized from the surface of the particle offer reduced plastic resistance due to easy slip between the layers, (b) brittle behavior caused by overall high plastic resistance when the inter-particle distance is greater than the critical ligament thickness, (c) ductile behavior caused by reduced plastic resistance when inter-particle distance is shorter than the critical ligament thickness. ....	17
<b>1.9.</b> Procedures to make ordered nanoporous alumina. (a) high purity aluminum with rough surface, (b) smooth surface after electropolishing step, (c) first anodization. Pores are growing in self-ordered way, (d) elimination of the anodized layer formed in the first anodization step, (e) second anodization, (f) pore widening (optional step).....	19

<b>1.10.</b> Expansion of aluminum during anodic oxidation. Left picture depicts the level of unoxidized aluminum surface. <sup>11</sup> .....	20
<b>1.11.</b> Wetting of porous templates with polymeric melts or polymer-containing solutions. ‘A’ denotes adhesion and ‘C’ denotes cohesion. Cohesion takes much longer time than adhesion.....	22
<b>2.1.</b> Thermal gravimetric analysis (TGA) to determine the composition of the mixtures. (a) pyrene / LLDPE mixtures, (b) hexamethylbenzene / LLDPE mixtures. ....	30
<b>2.2.</b> Temperature calibration using organic molecules with sharp melting points. ....	33
<b>2.3.</b> Thermal analysis results for mixtures of pyrene and LLDPE. (a) DSC thermograms of selected mixtures for melting temperature determination; heating rate was 5 °C/min; $\phi_2$ is LLDPE volume fraction, (b) melting temperature plotted on the calculated equilibrium phase diagram. $\alpha$ : solid pyrene; $\beta$ : solid LLDPE; L, L', L'': liquid mixture of pyrene and LLDPE. Note that L-L demixing (binodal, spinodal) was not confirmed under these experimental conditions. ....	35
<b>2.4.</b> Thermal analysis results for mixtures of HMB and LLDPE. (a) DSC thermograms of selected mixtures for melting temperature determination; heating rate was 5 °C/min; $\phi_2$ is LLDPE volume fraction, (b) melting temperature plotted on the calculated equilibrium phase diagram. $\alpha$ : solid HMB; $\beta$ : solid LLDPE; L: liquid mixture of HMB and LLDPE. ....	36
<b>2.5.</b> DSC melting (dashed lines) and crystallization (solid lines) thermograms of pure diluents at 5 °C/min heating and cooling rates. (a) HMB, small melting peak at around 120 °C and small crystallization peak at around 110 °C are assumed to be from impurities, (b) pyrene.....	40
<b>2.6.</b> Crystallization process analysis for binary mixtures of LLDPE with HMB and pyrene. The volume fraction of LLDPE in the mixture was fixed at $\phi_2 = 0.25$ . (a) crystallization peaks from DSC obtained at a cooling rate of 5 °C/min, (i): neat LLDPE, (ii) HMB/LLDPE, (iii) pyrene/LLDPE, (b) micrographs from optical microscopy. Samples were cooled from 200 °C to 30 °C at a 5 °C/min cooling rate, (i) crystallization of HMB began at 156 °C for HMB/LLDPE, (ii) crystallization of HMB was complete at 107 °C for HMB/LLDPE (cross-polarized image), (iii) crystallization of pyrene began at 127 °C for pyrene/LLDPE, (iv) crystallization of pyrene was complete at 108 °C for pyrene/LLDPE (cross-polarized image).....	41
<b>2.7.</b> Polarized optical microphotographs of the solid-liquid interface. Thin samples of diluent/polymer (3/1, w/w) mixtures were quickly quenched from 200 °C to 20 °C. (a) HMB / LLDPE, (b) pyrene / LLDPE.....	43

<b>2.8.</b> Crystallization temperatures determined by DSC cooling at a 5 °C/min scanning rate. (a) pyrene and LLDPE mixtures, (b) HMB and LLDPE mixtures, (c) crystallization temperature of mixtures of pyrene and LLDPE plotted on the calculated equilibrium phase diagram, (d) crystallization temperature of mixtures of HMB and LLDPE plotted on the calculated equilibrium phase diagram.....	45
<b>2.9.</b> Optical microscopy images of pyrene/LLDPE mixtures. Samples were cooled from 200 °C to 30 °C at 5 °C/min. $\phi_2$ is the volume fraction of LLDPE.....	47
<b>2.10.</b> Optical microscopy images of HMB/LLDPE mixtures. Samples were cooled from 200 °C to 30 °C at 5 °C/min. $\phi_2$ is the volume fraction of LLDPE.....	48
<b>2.11.</b> SEM micrographs showing the morphology of fractured cross-sections of pyrene/LLDPE mixtures after extraction of pyrene. $\phi_2$ represents the volume fraction of LLDPE.....	50
<b>2.12.</b> SEM micrographs showing the morphology of fractured cross-sections of HMB/LLDPE mixtures after extraction of HMB. $\phi_2$ represents the volume fraction of LLDPE.....	51
<b>2.13.</b> Morphology of fractured cross-sections of pyrene/LLDPE (3/1) mixtures prepared at different cooling conditions. SEM micrographs were taken after the extraction of pyrene. (a) relatively slow cooling rate of 5 °C/min, (b) quenched with ice water at 0 °C, (c) quenched with liquid nitrogen at -196 °C.....	54
<b>2.14.</b> Gradually changing morphology of fractured cross-sections of pyrene/LLDPE (3/1) mixtures prepared under non-uniform cooling temperature. SEM micrographs were taken after the extraction of pyrene. ....	55
<b>2.15.</b> Effect of the viscosity of the polymer. (a) pyrene / high Mw HDPE (3/1), (b) pyrene / low Mw HDPE (3/1), (c) steady state viscosity (at the shear rate of 0.01 s <sup>-1</sup> ) of neat HDPE. SEM micrographs were taken after the extraction of pyrene. ....	57
<b>3.1.</b> TGA thermogram for iPP and TBBPA measured at a 10 °C/min heating rate.....	64
<b>3.2.</b> Photomicrographs taken by 45° polarized optical microscopy while mixtures of TBBPA and iPP were cooled from 200 °C at 10 °C/min. (a) iPP/TBBPA=9/1(v/v) at 200 °C, (b) iPP/TBBPA=9/1(v/v) at 160 °C, (c) iPP/TBBPA=9/1(v/v) at 140 °C, (d) iPP/TBBPA=8/2 (v/v) at 200 °C, (e) iPP/TBBPA=8/2(v/v) at 170 °C, (f) iPP/TBBPA=8/2(v/v) at 140 °C. ....	70
<b>3.3.</b> Equilibrium phase diagram for a mixture of TBBPA and iPP (Liquidus lines are calculated results and circles are melting temperatures measured by DSC at a 10 °C/min heating rate).....	71

<b>3.4.</b> DSC thermograms of selected samples for melting temperature determination (Reheating run at 10 °C/min).....	72
<b>3.5.</b> Dynamic mechanical analysis result measured at 1 Hz, 3 °C/min heating rate. (a) loss factor ( $\tan \delta$ ) versus temperature, (b) $T_g$ versus TBBPA content. ....	74
<b>3.6.</b> DSC thermograms of selected iPP/TBBPA mixtures obtained by cooling runs from 200 °C at 10 °C/min. ....	75
<b>3.7.</b> Micrographs of iPP spherulites taken by cross-polarized optical microscopy at room temperature. (a) neat iPP, (b) 10 wt.% TBBPA/iPP, (c) 20 wt.% TBBPA/iPP. ....	77
<b>3.8.</b> Wide-angle X-ray scattering results for mixtures of iPP and TBBPA. ....	78
<b>3.9.</b> Relative crystallinity ( $X_t$ in equation 3.1) as a function of time as measured by quenching each molten sample to predetermined temperatures ( $T_q$ ). (a) $T_q$ : 117 °C, (b) effect of TBBPA content at $T_q$ : 117 °C, (c) $T_q$ : 120 °C, (d) effect of TBBPA content at $T_q$ : 120 °C, (e) $T_q$ : 123 °C, (f) effect of TBBPA content at $T_q$ : 123 °C. ....	80
<b>3.10.</b> Crystallization kinetics as analyzed using the Avrami equation. (a) $n$ versus quenching temperature, (b) $\ln(K)$ versus quenching temperature, (c) crystallization half-time ( $t_{1/2}$ ) versus quenching temperature. ....	82
<b>3.11.</b> Steady state shear viscosity. (a) 180 °C, (b) 200 °C, (c) steady state shear viscosity as a function of TBBPA content (at a shear rate of 0.01 s <sup>-1</sup> ). ....	83
<b>3.12.</b> SEM micrographs of composite materials. (a) 5 wt.% TBBPA/iPP, (b) 10 wt.% TBBPA/iPP, (c) 15 wt.% TBBPA/iPP, (d) 20 wt.% TBBPA/iPP.....	85
<b>3.13.</b> Engineering stress versus strain curve measured at room temperature (Curves are shifted along the strain axis for clarity). ....	87
<b>3.14.</b> Summary of tensile properties measured at room temperature. (a) yield stress versus TBBPA content, (b) Young's modulus versus TBBPA content with error bars, (c) tensile toughness versus TBBPA content, as calculated from the area under the stress versus strain curve.....	88
<b>3.15.</b> SEM micrographs of iPP + 15 wt.% TBBPA (Cross-sections are obtained by cryo-cutting of the tensile specimens after the tension test along the direction of deformation). (a) outside of necking region at high magnification, (b) outside of necking region at low magnification, (c) necking region at high magnification, (d) necking region at low magnification. ....	89
<b>3.16.</b> Load versus displacement curve from the three point bending test for single-edge notched bend specimens performed at room temperature with cross-head	

speed of 50 mm/min (Curves are shifted along the displacement axis for clarity). .....	91
<b>3.17.</b> SEM micrographs of the fractured surface after the three point bending test. (a) neat iPP; near crack tip region, (b) TBBPA 10 vol.%; near the crack tip region, (c) TBBPA 10 vol.%; far-away region from the crack tip (scale bar is 10 $\mu$ m). .....	93
<b>3.18.</b> DSC thermograms of neat TBBPA. (a) first cycle of heating and cooling at 10 $^{\circ}$ C/min, (b) second cycle of heating and cooling at 5 $^{\circ}$ C/min. ....	95
<b>3.19.</b> Four-point double notched specimen to investigate the crack propagation path.....	97
<b>3.20.</b> Morphology along the crack propagation path (Crack tip region is indicated with an arrow). (a) optical microscopy, (b) confocal microscopy, (c) SEM (oversized flaws in the crack path are indicated inside a circle). .....	98
<b>3.21.</b> Melting temperature of PA/iPP composites as measured by DSC at 10 $^{\circ}$ C/min. (a) thermograms from DSC reheating runs, (b) melting temperature of PA/iPP composites and TBBPA/iPP composites.....	101
<b>3.22.</b> Crystallization temperature of PA/iPP composites as measured by DSC at 10 $^{\circ}$ C/min. (a) thermograms from DSC cooling runs, (b) crystallization temperature of PA/iPP composites and TBBPA/iPP composites. ....	102
<b>3.23.</b> Glass transition temperature of PA/iPP composites as measured by DMA at 1 Hz, 3 $^{\circ}$ C/min heating rate. (a) PA/iPP composites, (b) TBBPA/iPP composites, (c) comparison of $T_g$ between PA/iPP composites and TBBPA/iPP composites. ....	103
<b>3.24.</b> Micrographs of iPP spherulites taken by cross-polarized optical microscopy at room temperature. Each sample was cooled from 200 $^{\circ}$ C to room temperature at 10 $^{\circ}$ C/min. (a) neat iPP, (b) 10 wt.% PA/iPP, (c) 20 wt.% PA/iPP.....	104
<b>3.25.</b> Steady state shear viscosity at the shear rate of 0.01 $s^{-1}$ , using a parallel plate rheometer. (a) test temperature: 180 $^{\circ}$ C, (b) test temperature: 200 $^{\circ}$ C. ....	106
<b>3.26.</b> Engineering stress versus strain curve of PA/iPP composites. (curves are shifted along the strain axis for clarity). Inset plot is an initial response to compare the stiffness. ....	107
<b>3.27.</b> Summary of tensile properties. (a) yield stress, (b) Young's modulus, (c) tensile toughness as calculated from the area under the stress versus strain curve. ....	108
<b>3.28.</b> Fracture toughness as measured by stress intensity factor ( $K_Q$ ) using 3mm thick single edge notched bend (SENB) specimens. (a) load versus displacement for TBBPA/iPP composites, (b) load versus displacement for	

PA/iPP composites, (c) stress intensity factor as a function of organic filler content. ....	111
<b>3.29.</b> SEM micrographs of PA/iPP composite materials. (a) 5 wt.% PA in iPP, (b) 10 wt.% PA in iPP, (c) 15 wt.% PA in iPP, (d) 20 wt.% PA in iPP. ....	112
<b>4.1.</b> Morphology of nanoporous alumina templates. (a) top view, (b) side view .....	120
<b>4.2.</b> Scheme for preparing polymer-metal composite surfaces. ....	121
<b>4.3.</b> Surface morphology of composite materials (SEBS in porous alumina template) prepared at different abrasion temperature ( $T_o$ ). (a) $T_o = 0$ °C (SEM), (b) $T_o = 40$ °C (SEM), (c) $T_o = 20$ °C (AFM). ....	124
<b>4.4.</b> Etching of closed-end of alumina template containing polymers inside the pores (pore-opening) using 5% phosphoric acid solution at different etching times. (a) 0 minute, (b) 30 minutes, (c) 60 minutes, (d) 90 minutes, (e) 120 minutes, (f) 150 minutes. After complete removal of the alumina layer, empty holes were observed. ....	126
<b>4.5.</b> Contact angles of composite surfaces (FEP/alumina, a-c; SEBS/alumina, d-f) measured at different temperatures. Temperature was changed from 20 °C to 60 °C then returned to 20 °C. (a) FEP/alumina at 20 °C, instant wetting; (b) FEP/alumina at 60 °C, $\theta_{adv} = 40^\circ$ ; (c) FEP/alumina at 20 °C, $\theta_{adv} = 32^\circ$ ; (d) SEBS/alumina at 20 °C, instant wetting; (e) SEBS/alumina at 60 °C, $\theta_{adv} = 44^\circ$ ; (f) SEBS/alumina at 20 °C, instant wetting. ....	128
<b>A.1.</b> Expected influence of the electric field on the ionic component in the mixture. (a) Without electric field (unpolarized state), (b) With electric field (polarized). ...	134
<b>A.2.</b> Schematic description of sample preparation. (a) sample is sealed between the Kapton films and then placed between the aluminum/Kapton composite films, (b) positive and negative poles from the high voltage generator are connected to the aluminum layers of the composite films, (c) electric field is applied while the sample is melted inside the convection oven at 200 °C for 5 minutes and cooled at room temperature. ....	136
<b>A.3.</b> DSC thermograms of the ionic liquid / polymer mixtures as measured by heating at 10 °C/min. IL stands for ionic liquid and Pol stands for polymer. ....	138
<b>A.4.</b> (a) melting temperatures of the mixtures, (b) glass transition temperatures of the mixtures. ....	139
<b>A.5.</b> Change in temperature and electric current during melting and cooling of the samples under the influence of 10 V/ $\mu\text{m}$ of electric field. The mixture was composed of 80 wt.% ionic liquid and 20 wt.% polymer. (a) melting, (b) cooling. ....	142

<b>A.6.</b> Morphology of the cross-sections of the solidified mixtures prepared with an electric field (a – c) and without an electric field (d – f). The strength of electric field was 10 V/ $\mu$ m. (a) ionic liquid / polymer: 8/2, (b) ionic liquid / polymer: 7/3, (c) ionic liquid / polymer: 5/5, (d) ionic liquid / polymer: 8/2, (e) ionic liquid / polymer: 7/3, (f) ionic liquid / polymer: 5/5. ....	144
<b>A.7.</b> TGA thermogram of pure 1-butyl-4-methylpyridinium chloride. Sample was exposed to air for less than one minute while being placed inside the TGA chamber. ....	146

# CHAPTER 1

## INTRODUCTION

### 1.1. Phase Transformations in Polymer Systems

Mechanical and other properties of polymeric materials depend on their microstructures, which are often produced as a result of phase transformations – an alteration in the number and/or character of the phases. Since phase transformation phenomena play a major role in controlling the morphology of polymer products in many cases, significant research effort has been expended to understand phase transformation phenomena in polymer science.<sup>1</sup> The majority of the work presented in this thesis is based on phase separation processes in selected polymer systems to develop unique microporous materials and self-reinforcing thermoplastic materials. It is, therefore, helpful to understand the phase transformation processes in polymer systems with relevant equilibrium phase diagrams.

There are generally two kinds of phase separation in polymer systems, neglecting the more complex behaviors of block copolymers: liquid-liquid (L-L) demixing and solid-liquid (S-L) demixing due to crystallization.<sup>2</sup> Since the phase behavior of polymer systems can be analyzed by the equilibrium phase diagrams, the first step in dealing with the polymer systems is often the construction of phase diagrams. Even though most phase diagrams represent only equilibrium states and microstructures, they are nevertheless useful in understanding the development of nonequilibrium structures and properties. While it is possible to construct phase diagrams by various experimental methods, calculation of phase diagrams is also

possible in many cases and has advantages over experimental methods. In addition to the obvious advantages in time and cost, calculation allows material properties to be adjusted more conveniently to predict new phenomena.

Equilibrium phase diagrams for polymer systems with limited miscibility in both solid and liquid phases can be calculated using Flory-Huggins solution thermodynamics.<sup>2-4</sup> According to the lattice treatment of Flory-Huggins theory, the free energy of mixing can be expressed as

$$\left. \frac{\Delta F_m}{k_B T} \right|_{site} = \phi_1 \ln(\phi_1) + \frac{\phi_2}{N} \ln(\phi_2) + \chi \phi_1 \phi_2 \quad (1.1)$$

where  $\Delta F_m$  denotes the free energy of mixing,  $\phi$  is volume fraction,  $N$  is degree of polymerization,  $\chi$  is the Flory-Huggins interaction parameter and subscripts 1 and 2 represent diluent and polymer, respectively. If we assume that the interaction parameter is purely enthalpic, then the temperature dependence of  $\chi$  can be expressed as

$$\chi = \frac{\beta}{T} = \frac{(\delta_1 - \delta_2)^2 V_1}{RT} \quad (1.2)$$

where  $\delta$  is solubility parameter and  $V_1$  is molar volume of diluent.

The equilibrium between phase A and phase B can be reached if the chemical potential ( $\Delta\mu$ ) of each component ( $i$ ) in each phase ( $A, B$ ) is equal (equation 1.3).

$$\Delta\mu_i^A = \Delta\mu_i^B \quad (i = 1, 2) \quad (1.3)$$

The binodal curve, also called as coexistence curve, represents the boundary between a homogeneous liquid phase and the two liquid phase regime, which can be found from the locus of solutions to equation 1.3 as  $\chi$  varies with the temperature. The detailed procedure to find the binodal curve is illustrated using an example as follows. If the free

energy of mixing for a polymer system at a certain temperature is negative, as shown in Figure 1.1, mixing will occur since free energy can be lowered by mixing in this case. However, if the free energy of mixing can be further decreased by phase separation, then the polymer system may undergo phase separation to minimize the free energy. This happens when there exists one straight line that is tangential to the free energy of mixing at two different points. Since the slope of the tangential line is the chemical potential of the component in the system, two phases (phase A with composition of  $\phi_a$  and phase B with composition of  $\phi_b$  in this example) can coexist when the slope of the tangential line at each composition (which is the chemical potential of each phase) is the same. Since the expression for the free energy of mixing is nonlinear, solutions are found either graphically or numerically. This procedure can be repeated at different  $\chi$ 's as shown in Figure 1.2. This allows us to find the compositions of two phases that can coexist at each  $\chi$  value, and a binary curve (or coexistence curve) can be constructed as shown in Figure 1.3. Since the interaction parameter ( $\chi$ ) is assumed to be a function of temperature only, it is possible to plot the phase diagram either as  $\chi$  versus composition or as temperature versus composition.

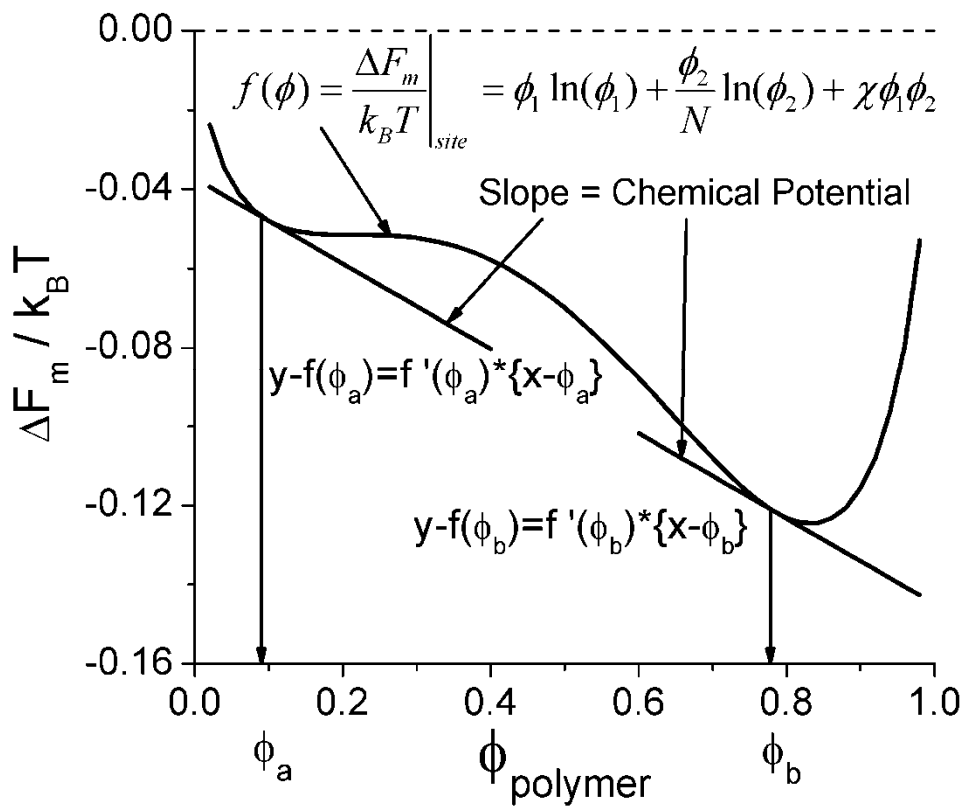


**Figure 1.1.** Example of the free energy of mixing for a polymer system at certain fixed temperature.  $\chi$ , known as Flory-Huggins interaction parameter, is assumed to be a function of temperature only.

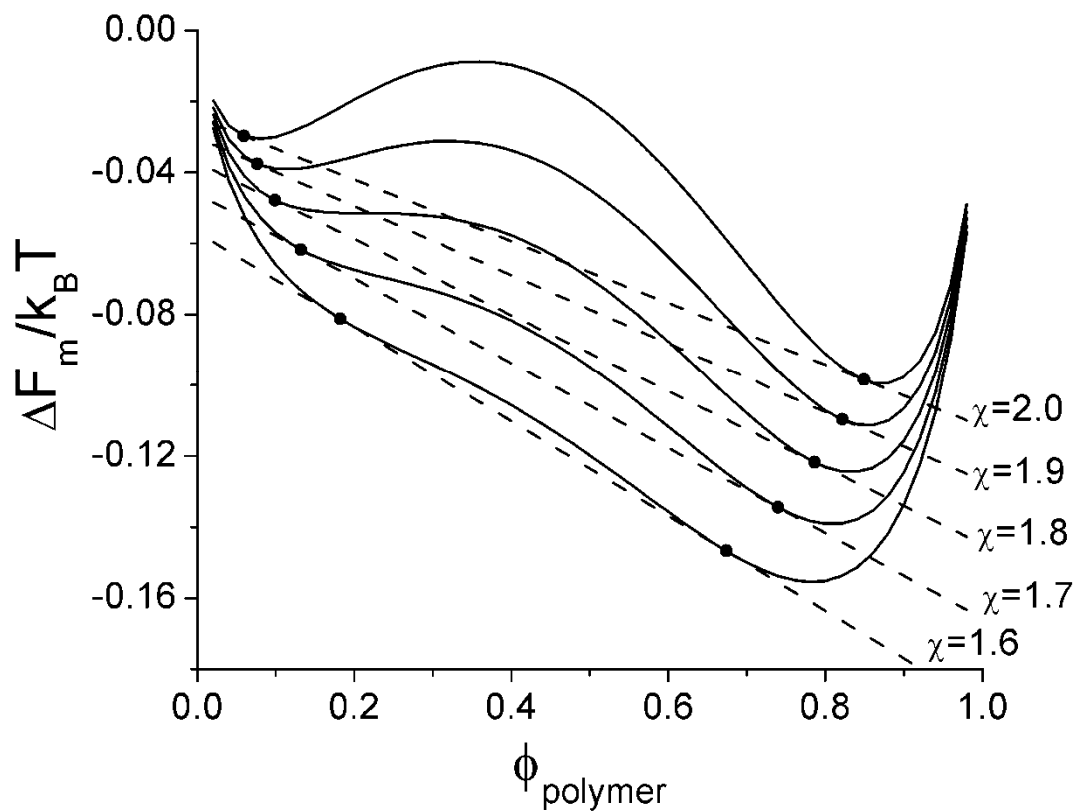


**Figure 1.2.** Straight lines that are tangential to the free energy of mixing curve at two different compositions can be found at different  $\chi$ 's.

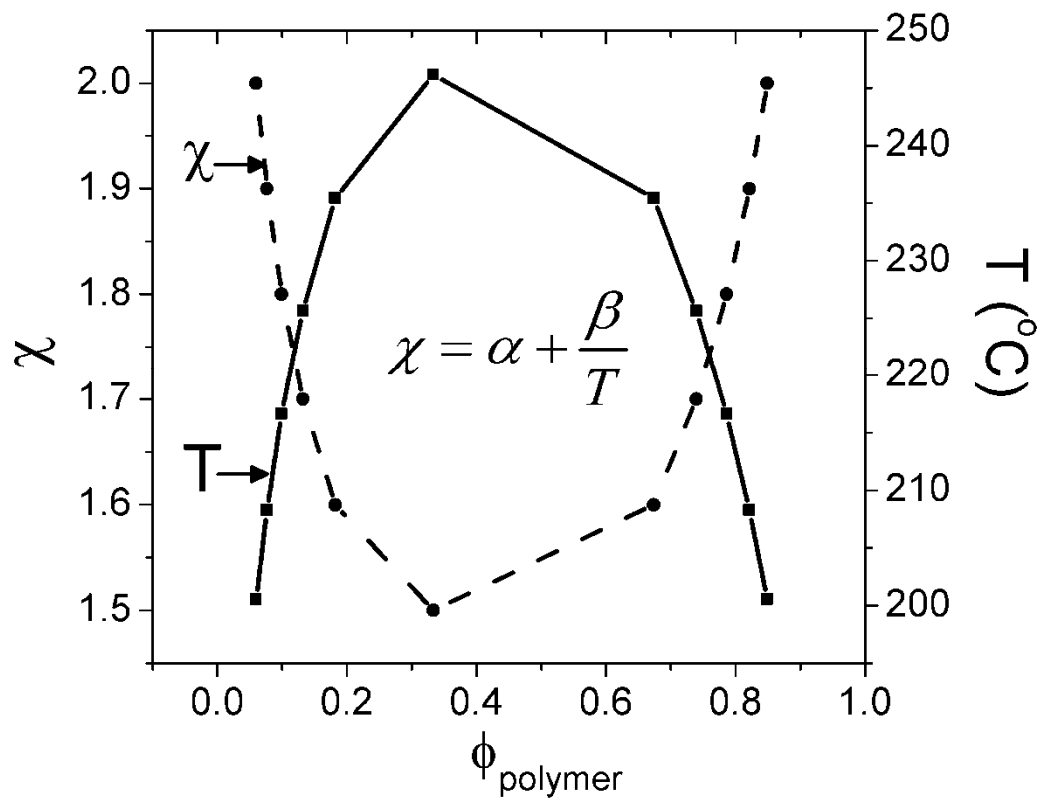


**Figure 1.3.** L-L demixing as represented by binodal (coexistence) curve

The two liquid phase regime can be subdivided into two regions, one of them unstable and the other metastable. As illustrated in Figure 1.4, a polymer system is stable against fluctuation if the second derivative of the free energy with respect to composition is positive. If it is negative, then the polymer system is unstable. Therefore, the boundary between the stable region and unstable one can be found by considering the stability of the polymer solution as

$$\left. \frac{\partial^2}{\partial \phi_2^2} \left( \frac{\Delta F_m}{k_B T} \right) \right|_{p,T} = 0 \quad (1.4)$$

If the Flory-Huggins expression is used for free energy, then equation 1.4 can be expressed as

$$\frac{\partial^2}{\partial \phi_2^2} \left( \frac{\Delta F_m}{k_B T} \right) = -\frac{1}{(1-\phi_2)} + \left( 1 - \frac{1}{N} \right) + 2\chi\phi_2 = 0 \quad (1.5)$$

The solution of equation 1.5 is

$$\phi_2 = \frac{(1-N+2\chi N) \pm \sqrt{-8\chi N + (-1+N-2\chi N)^2}}{4\chi N} \quad (1.6)$$

from which the spinodal curve can be constructed as shown in Figure 1.5.

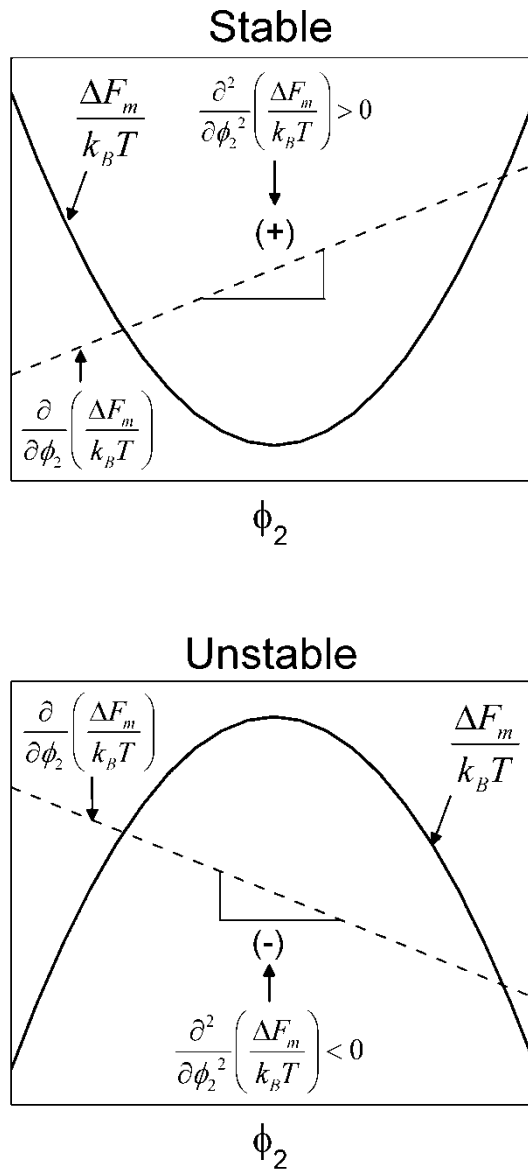
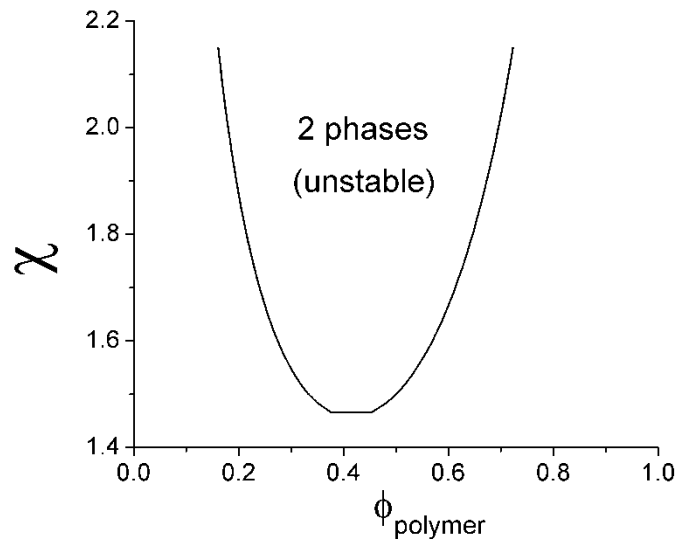


**Figure 1.4.** Stability of polymer system against fluctuations. The boundary between stable state and unstable state can be found by  $\frac{\partial^2}{\partial \phi_2^2} \left( \frac{\Delta F_m}{k_B T} \right) = 0$ .



$\chi = \alpha + \frac{\beta}{T}$

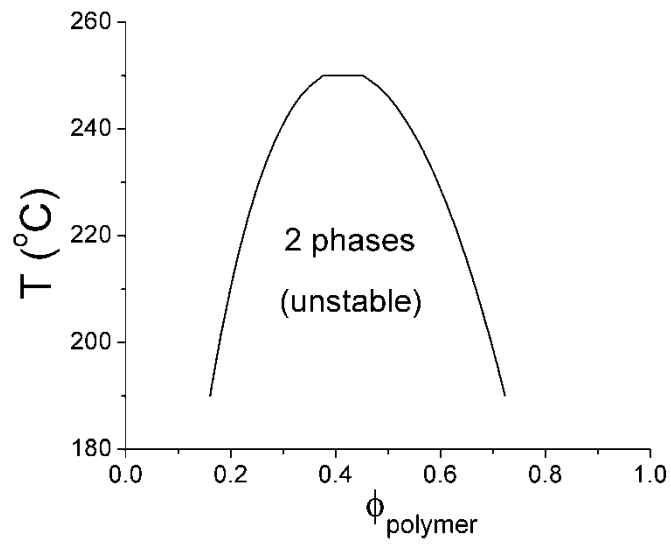


**Figure 1.5.** Spinodal curve as constructed from Equation 1.6.

S-L demixing may occur by the solidification of either the polymer or the diluent. If the S-L demixing occurs by the solidification of the semi-crystalline polymer, then the equilibrium between a crystalline polymer and a polymer in solution should be established which requires that the chemical potential of the polymer in each phase is equal (equation 1.7),

$$\Delta\mu_u^L = \Delta\mu_u^C \quad (1.7)$$

where superscript  $L$  denotes liquid phase,  $C$  denotes crystalline phase and subscript  $u$  denotes polymer repeat unit. The chemical potential of the polymer repeat unit in each phase can be written in the following way (equations 1.8 and 1.9),

$$\Delta\mu_u^C = -\Delta F_u = -(\Delta H_u - T_m \Delta S_u) = -\Delta H_u (1 - T_m / T_m^0) \quad (1.8)$$

$$\Delta\mu_u^L = RT_m \left( \frac{V_u}{V_1} \right) \left[ \frac{\ln \phi_2}{N} - \left( 1 - \frac{1}{N} \right) (1 - \phi_2) + \chi (1 - \phi_2)^2 \right] \quad (1.9)$$

where  $T_m$  is the melting temperature of crystalline polymer in polymer solution,  $T_m^0$  is the melting temperature of neat polymer,  $\Delta H_u$  is the enthalpy of fusion per repeat unit,  $V_u$  is the molar volume of the polymer repeat unit and  $V_1$  is the molar volume of the diluent. If equation 1.2 is used for  $\chi$  and substituted in equation 1.9, then the equilibrium melting temperature for a polymer in solution can be found from equations 1.7, 1.8 and 1.9 as

$$\frac{1}{T_m} = \left[ 1 + \frac{R\beta}{\Delta H_u} \left( \frac{V_u}{V_1} \right) (1 - \phi_2)^2 \right]^{-1} \left[ \frac{1}{T_m^0} + \frac{R}{\Delta H_u} \left( \frac{V_u}{V_1} \right) \left\{ \left( 1 - \frac{1}{N} \right) (1 - \phi_2) - \frac{\ln(\phi_2)}{N} \right\} \right] \quad (1.10)$$

where  $\beta$  is a constant that is equal to  $(\delta_1 - \delta_2)^2 V_1 / R$ . Burghardt obtained a similar expression assuming that  $V_u$  and  $V_1$  are the same.<sup>2</sup>

If the S-L demixing occurs by the solidification of the crystallizable diluent, then equilibrium between a crystalline diluent and a polymer in solution should be established which requires that the chemical potential of the diluents in each phase is equal (equation 1.11),

$$\Delta\mu_1^L = \Delta\mu_1^C \quad (1.11)$$

Again, the chemical potentials in equation 1.11 can be written as

$$\Delta\mu_1^C = -\Delta F_1 = -(\Delta H_1 - T_{m,1} \Delta S_1) = -\Delta H_1 (1 - T_{m,1} / T_{m,1}^0) \quad (1.12)$$

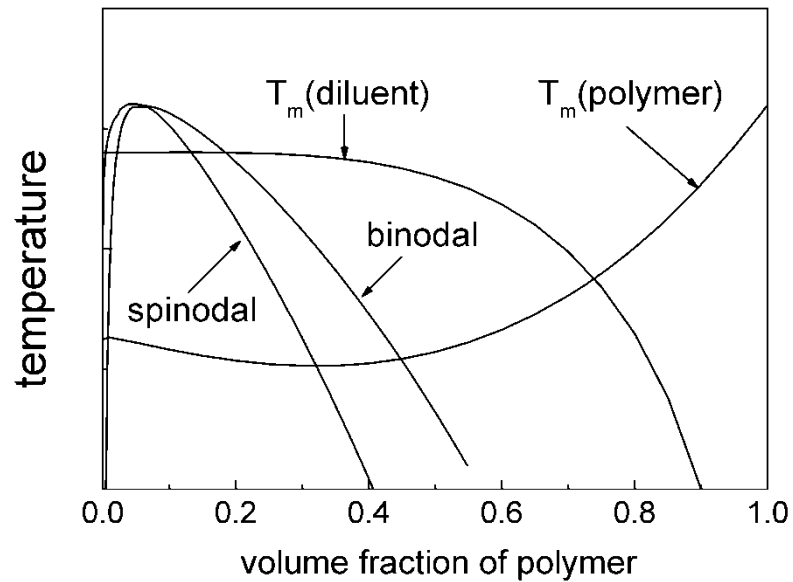
$$\Delta\mu_1^L = RT_{m,1} \left[ \ln(1 - \phi_2) + \left(1 - \frac{1}{N}\right) \phi_2 + \chi \phi_2^2 \right] \quad (1.13)$$

where  $T_{m,1}$  is the melting temperature of the diluent in solution,  $T_{m,1}^0$  is the melting temperature of neat diluent and  $\Delta H_1$  is the enthalpy of fusion for diluent. By using equations 1.2, 1.11, 1.12 and 1.13, the equilibrium melting temperature of a diluent can be found as

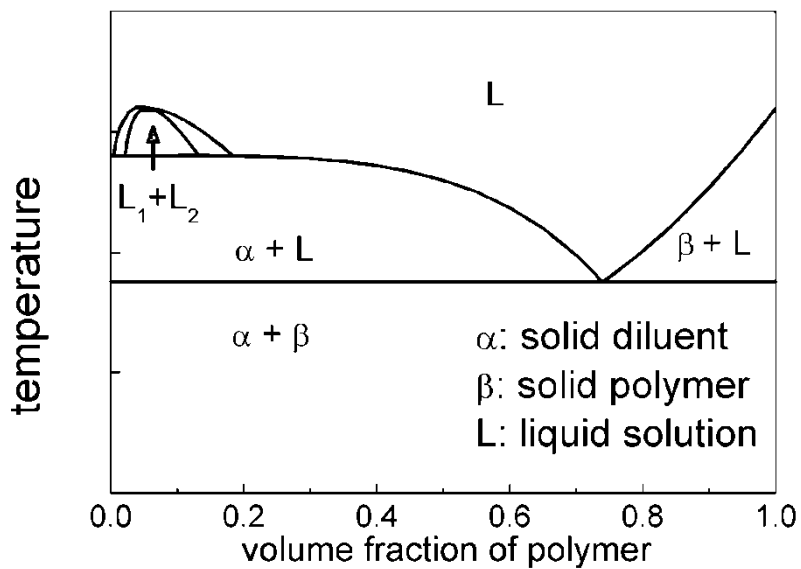
$$\frac{1}{T_{m,1}} = \left[ 1 + \frac{R\beta\phi_2^2}{\Delta H_1} \right]^{-1} \left[ \frac{1}{T_{m,1}^0} - \frac{R}{\Delta H_1} \left\{ \left(1 - \frac{1}{N}\right) \phi_2 + \ln(1 - \phi_2) \right\} \right] \quad (1.14)$$

A typical phase diagram as calculated according to this procedure is shown in Figure 1.6.

Phase diagrams will be calculated for mixtures of polyethylene and high-melting crystallizable diluents to investigate the morphology of the selected polymer systems in Chapter 2. The same procedure will also be used to construct the phase diagram for a mixture of isotactic polypropylene and crystallizable diluents in Chapter 3 in which a novel strategy of toughening thermoplastic materials with enhanced processability is introduced.



(a)



(b)

**Figure 1.6.** Typical phase transition boundary curves and the resulting phase diagram for a mixture of semi-crystalline polymer and crystallizable diluents that show limited miscibility in both liquid phase and solid phase. (a) phase transition boundary curves, (b) equilibrium phase diagram.

## 1.2. Toughening of Plastics

A new approach to reinforce and toughen isotactic polypropylene (iPP) with improved processability is discussed in Chapter 3. Although the strategy involved is different from conventional particle toughening, the underlying toughening mechanism is similar to the general theory of toughening. It is, therefore, worthwhile reviewing the current understanding of toughened plastics.

General fracture behavior of materials can be looked at simply by considering the brittle-ductile transition temperature as shown in Figure 1.7.<sup>5</sup> Fracture of material can be either brittle or ductile, which is determined by the lowest resistance. If the yield strength ( $\sigma_Y$ ) is lower than the brittle strength ( $\sigma_B$ ) at a given temperature, the material will show an energy absorbing, ductile response. However, the material will show a brittle response if the brittle strength is lower than the yield strength at a given temperature. Brittle fracture does not consume appreciable energy. The brittle strength is a flaw-governed property and shows negligible dependence on temperature or deformation rate. In contrast, yield strength decreases as temperature increases or deformation rate increases. The crossover point of the lines that represent yield strength and brittle strength in a stress versus temperature plot gives the brittle-ductile transition temperature. For example, if the material's yield strength and brittle strength show characteristic behaviors as illustrated in Figure 1.7a, a brittle response will be observed at room temperature. If, however, the deformation rate is reduced, yield strength will decrease more than brittle strength and the material will show an energy-absorbing, ductile response (Figure 1.7b). If the plastic resistance is reduced so that the yield strength is decreased, the material will show a ductile response (Figure 1.7c).

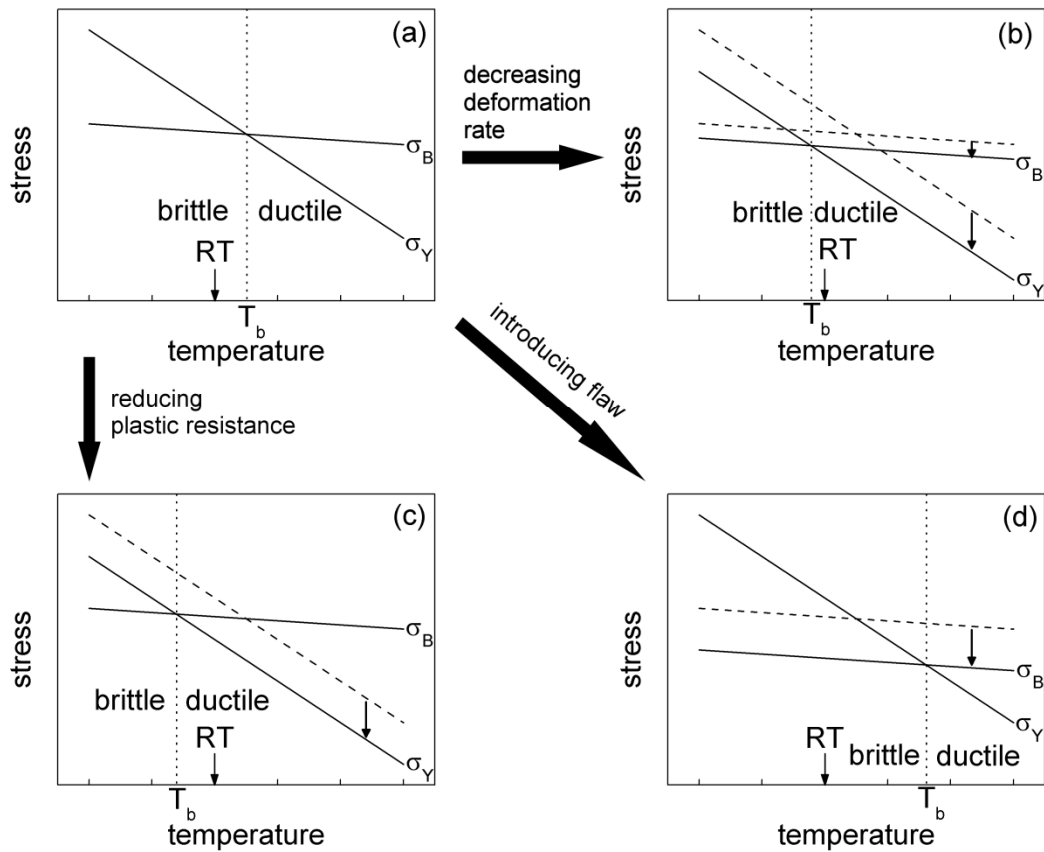


**Figure 1.7.** Change in brittle-ductile transition temperature ( $T_b$ ) under various conditions (known as Davidenkov diagram).  $\sigma_Y$  represents yield strength and  $\sigma_B$  represents brittle strength. (a) material is brittle at room temperature, (b) material becomes ductile by decreasing deformation rate, (c) material becomes ductile by reducing plastic resistance, (d) material becomes highly brittle by introducing a flaw.

Introducing a flaw will cause the brittle strength to decrease significantly and the material will show highly brittle behavior (Figure 1.7d). This simple analysis clearly shows that fracture toughness will be increased by inducing a ductile response, which can be made possible by reducing plastic resistance, decreasing deformation rate and avoiding any flaws.

Plastic resistance can be easily reduced by introducing soft particles in the polymer matrix. In this case, cavitation occurs at the early stage of deformation so that the initial resistance of deformation can be reduced significantly. Although cavitation itself does not consume an appreciable amount of the total fracture energy, it allows the subsequent yielding and total plastic flow to occur, which consume a significant amount of energy. This strategy, however, inevitably causes the material's stiffness to decrease significantly. If rigid particles are used as a reinforcement, stiffness of the material increases but toughness shows mixed results; depending on the particle size, concentration and interfacial adhesion between the particle and the polymer matrix, toughness can either increase or decrease.

Wu first suggested that interparticle distance, which is determined by the volume fraction of the particle and the size of the particle, is the key factor governing the material's fracture behavior using a soft particle-toughened system.<sup>6</sup> Argon and coworkers generalized Wu's idea and showed that the source of the toughness is the plastic extensibility of the matrix material in the interparticle ligament and that the mechanical properties of the filler particles are of little importance for toughness.<sup>7-11</sup> They argued that the crystallization of polymers is initiated from the surface of the particles (since heterogeneous nucleation occurs more easily than homogeneous

nucleation) and low energy planes of oriented crystals are formed in the near-interparticle layer of the polymer with specific thickness (since the oriented crystals can slip over each other easily, offering low resistance of deformation). If the thickness of this oriented layer between particles is below a certain critical value (critical ligament thickness, which depends on the polymer matrix only), easily stretchable ligaments with reduced plastic resistance will percolate throughout the structure promoting a plastic response of the entire material. If not, the overall plastic resistance will be significantly elevated and the material is likely to fail by extrinsic flaws leading to premature brittle fracture (Figure 1.8). Prerequisite conditions for this mechanism are that particles should cavitate (soft particle) or de-wet (rigid particle) to allow unhindered plastic deformation around the particles, and that big agglomerates should be avoided to prevent brittle response. It will be shown in Chapter 3 that a similar toughening mechanism as that described here can be effective for crystalline organic compounds, with the additional benefit of enhanced processability.

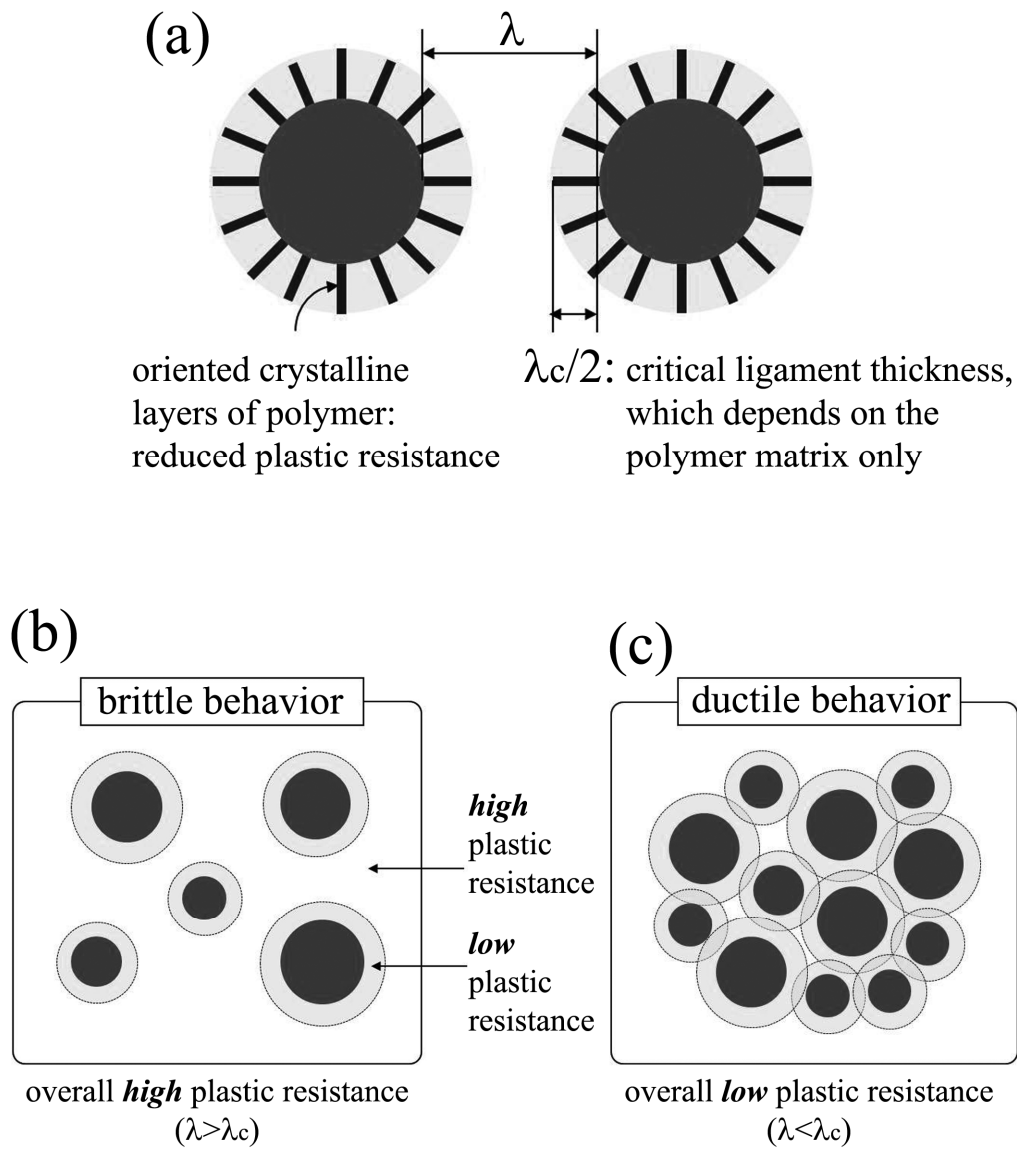


**Figure 1.8.** Critical ligament thickness that can be used to predict the fracture behavior of the materials. (a) oriented layers of the polymer crystallized from the surface of the particle offer reduced plastic resistance due to easy slip between the layers, (b) brittle behavior caused by overall high plastic resistance when the inter-particle distance is greater than the critical ligament thickness, (c) ductile behavior caused by reduced plastic resistance when inter-particle distance is shorter than the critical ligament thickness.

### 1.3. Wetting of Polymers inside Nanoporous Alumina Template

Ordered nanoporous aluminum oxide materials have attracted increasing attention in recent years due to their utilization for the development of various functional nanostructures.<sup>7-8</sup> This trend originated from the discovery of self-ordered porous anodic aluminum oxide (AAO) membranes by Masuda and Fukuda in 1995.<sup>9</sup> They reported self-organized pore growth, leading to a densely packed hexagonal pore structure for certain sets of parameters. The self-ordered alumina pore arrays can be prepared under certain anodization conditions which require several days of processing time and very narrow processing windows, known as ‘self-ordering regimes’. Table 1.1 summarizes selected processing conditions to produce self-ordered porous alumina structures.<sup>10</sup>

**Table 1.1.** Self-ordering regimes for anodization of aluminum

Electrolyte	Voltage	Pore diameter	Inter-pore distance
Sulfuric acid (1M)	19 V	~ 14 nm	~ 50 nm
Sulfuric acid (0.3M)	25 V	~ 19 nm	~ 65 nm
Oxalic acid (0.3M)	40 V	~ 35 nm	~ 100 nm
Phosphoric acid (1M)	160 V	~ 120 nm	~ 400 nm
Phosphoric acid (0.1M)	195 V	~ 180 nm	~ 500 nm

The typical procedure to prepare self-ordered AAO requires 2-step anodization as shown in Figure 1.9.<sup>9</sup> High purity aluminum (> 99.99 %) is cleaned with acetone and water, followed by annealing for 3 hours at 500 °C in N<sub>2</sub> environment to obtain large single crystalline grains. Surface roughness is reduced by electropolishing which is usually done in a mixture of HClO<sub>4</sub>/ C<sub>2</sub>H<sub>5</sub>OH (1/3) at 5 V for 5~15 minutes. After

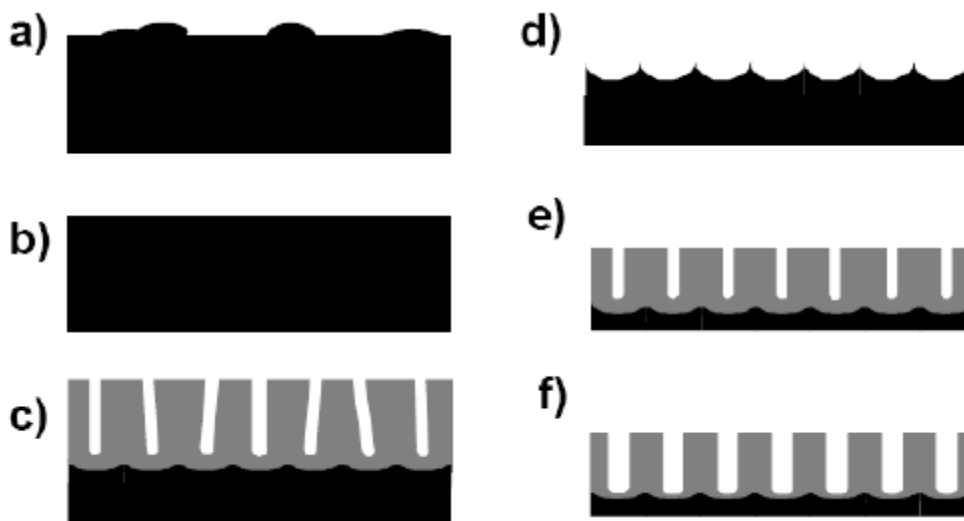


**Figure 1.9.** Procedures to make ordered nanoporous alumina. (a) high purity aluminum with rough surface, (b) smooth surface after electropolishing step, (c) first anodization. Pores are growing in self-ordered way, (d) elimination of the anodized layer formed in the first anodization step, (e) second anodization, (f) pore widening (optional step).

the pretreatment, anodization is performed under one of the conditions as listed in Table 1.1 for more than 1 day. Pores are randomly created on the surface at the early stage of anodization, but self-ordering occurs due to the repulsive interaction between the neighboring pores as the anodization proceeds. Then, the porous alumina layer is selectively removed in a solution containing chromic acid. Patterns that are replicas of the hexagonal pore array are preserved on the fresh aluminum surface after etching by chromic acid solution. This allows the preparation of pores with high regularity by a subsequent second anodization under the same conditions as the first anodization. Pores in the final structure can be isotropically widened by chemical etching with 0.5 ~ 1 M phosphoric acid, if needed. (Figure 1.9f)

Self-organization is most likely driven by the mechanical stress between neighboring pores which is associated with the volume expansion during oxide formation at the metal/oxide interface (Figure 1.10).<sup>11</sup> This claim is supported by the fact that the porosity of highly ordered membranes is always equal to  $\sim 10\%$  which is identical to the calculated value based on the mechanical stress model.<sup>12</sup> When aluminum is oxidized to alumina, the volume expands by roughly a factor of 2 since the atomic density of aluminum in alumina is a factor of 2 lower than in metallic aluminum. However, the volume expansion coefficient ( $\xi$ ) is less than twice under usual experimental conditions due to the loss of  $\text{Al}^{3+}$  ion to the electrolyte solution and hydration reaction of the oxide layer at the oxide/electrolyte interface which leads to a dissolution and thinning of the oxide layer. According to the results from Jessensky et al.,<sup>11</sup> self-ordered porous alumina is best formed when the volume expansion coefficient ( $\xi$ ) is close to 1.2.

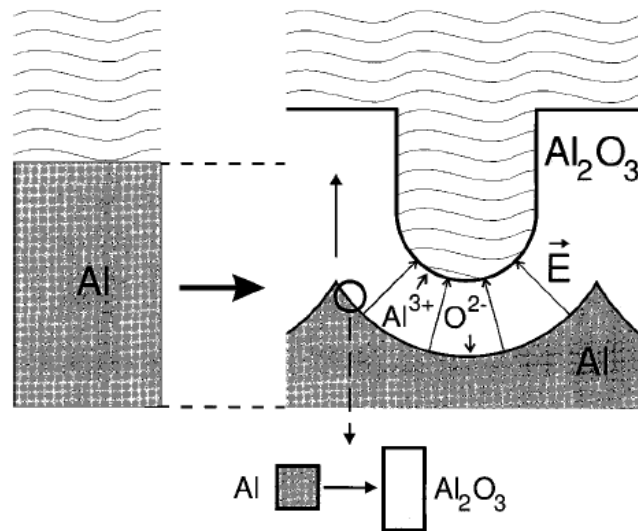


**Figure 1.10.** Expansion of aluminum during anodic oxidation. Left picture depicts the level of unoxidized aluminum surface.<sup>11</sup>

Since solutions, mixtures, or melts with low surface energies spread over substances with high surface energies, nanoporous AAO templates have been widely used to produce nanotubes and nanowires by wetting with various polymers.<sup>13-17</sup> This is possible because most organic polymers have low surface energy (typically under 100 mN/m) while inorganic oxides such as AAO have high surface energy (ranging from a few hundred to several thousand mN/m). Depending on the interfacial tensions, either complete wetting or partial wetting may occur, which can be defined by the spreading coefficient ( $S$ )<sup>18</sup>

$$S = \gamma_{SG} - \gamma_{SL} - \gamma_{GL} \quad (1.13)$$

in which  $\gamma_{SG}$  is the interfacial tension between solid and gas (air),  $\gamma_{SL}$  is the interfacial tension between solid and liquid (molten polymer), and  $\gamma_{GL}$  is the interfacial tension between gas (air) and liquid (molten polymer). Complete wetting occurs when  $S$  is positive and a thin liquid layer spontaneously spreads on the solid surface very quickly, typically in a few seconds. Nanotubes can be obtained from the complete wetting of molten polymer on the cylindrical nanopores of the templates. When  $S$  is negative, partial wetting occurs and the liquid forms a finite contact angle ( $\theta = \cos^{-1}((\gamma_{SG} - \gamma_{SL})/\gamma_{GL})$ ) with the solid surface. Nanometer-scale capillarity may occur when the molten polymer is in contact with cylindrical nanopores of the templates and nanowires can be produced as a result. Wetting is strongly affected by the temperature and a wetting transition from partial wetting to complete wetting may be observed at a certain temperature (wetting transition temperature).<sup>19</sup> Contact angle generally becomes zero at the wetting transition temperature. Wetting may also be affected by the diameter of the

template pores; if the diameter of the template pores become smaller than the wall thickness of the nanotubes, massive nanowires should form instead.<sup>20</sup>

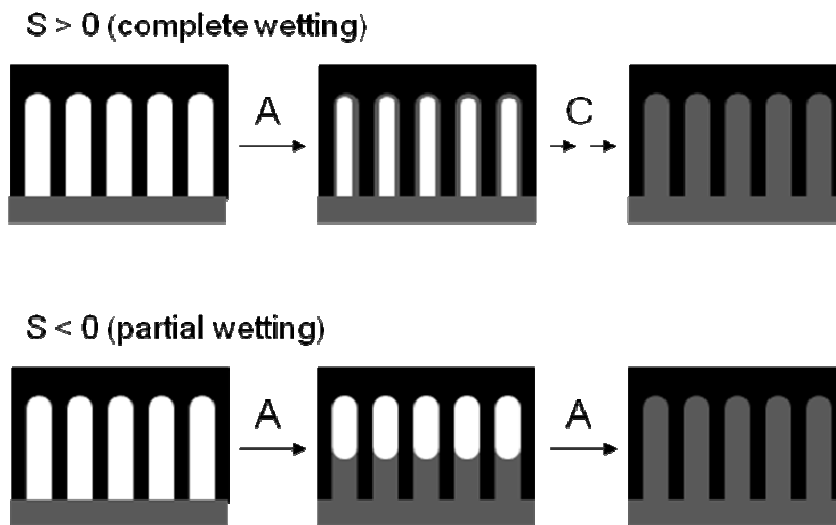


**Figure 1.11.** Wetting of porous templates with polymeric melts or polymer-containing solutions. ‘A’ denotes adhesion and ‘C’ denotes cohesion. Cohesion takes much longer time than adhesion.

Nanoporous alumina templates filled with polymers may exhibit interesting properties because they are composite materials composed of two completely different components. Thermal property is one example. While alumina is an excellent thermal conductor with a low coefficient of thermal expansion, polymers are relatively poor thermal conductors with high coefficients of thermal expansion. Upon heating, polymer rods that fill the inside of the pores should expand more than the alumina, causing the surface properties of the composite material to be governed by the protruded polymer bumps through chemical (from alumina to organic polymer) and topographical (from

flat surface to rough surface due to polymer bumps) changes. The idea of thermally active composite surfaces will be discussed in Chapter 4.

#### **1.4. Dissertation Overview**

Chapter 2 deals with the preparation and characterization of locally anisotropic porous materials using polyethylene and crystallizable high melting diluents. The effect of diluent identity and the composition of the polymer solutions will be discussed in terms of thermodynamics and kinetics. Phase diagrams are calculated and the characteristic behavior of the mixtures is discussed to provide a thermodynamic understanding of phase transformation processes. Optical microscopy and DSC results are provided to elucidate the effect of kinetics on the morphology of the mixtures.

Chapter 3 demonstrates how the idea as developed in Chapter 2 can be utilized for a quite different application. A new type of reinforced thermoplastic as developed by a thermally induced phase separation process is discussed in Chapter 3. The dual functionality of crystallizable diluents, which act as a processing aid at high temperature but undergo phase separation upon cooling to form solid particles that act as a toughening agent at service temperature, is explored. Processability as evaluated by shear viscosity measurements is discussed. The mechanical properties of the composite materials (tensile properties and fracture toughness) are discussed based on experimental results and relevant theories.

While the topics in Chapters 2 and 3 are based on phase transformation processes in polymer solutions, thermally active composite surfaces in Chapter 4 are based on polymer-metal hybrid strategies. Composite surfaces composed of a nanoporous alumina template filled with polymers are prepared using a simple wetting

process and the surface morphology and surface properties are probed using SEM, AFM and a goniometer equipped with a temperature controller. The effect of the polymer identity on the wettability of the surface and the reversibility of the thermal response is discussed. Limitations of the current methodology are discussed and future research directions are suggested.

## CHAPTER 2

### LOCALLY ANISOTROPIC POROUS MATERIALS FROM POLYETHYLENE AND CRYSTALLIZABLE DILUENTS

Locally anisotropic porous materials were prepared using linear low density polyethylene (LLDPE) and crystallizable organic diluents by thermally induced phase separation processes. Pyrene and hexamethylbenzene (HMB) were selected as crystallizable diluents because of their miscibility with LLDPE at elevated temperature, higher crystallization temperatures than that of LLDPE and their individual (very different) crystallization behaviors. Equilibrium phase diagrams were calculated using the Flory-Huggins theory of solution thermodynamics and show good agreement with experimental observations. The phase separation process, which was monitored visually using an optical microscope equipped with a temperature controller, shows strong dependence on solution composition as well as the diluent identity. Solidified materials after extraction of pyrene from pyrene/LLDPE mixtures exhibit locally aligned layers of pores, with features that depend on solution composition. The pores inside semicrystalline polyethylene domains are aligned in the crystal growth direction of pyrene, which crystallizes before LLDPE upon cooling. When HMB is used as the crystallizable diluent, plate-like pore structures, much larger in size than the pyrene-derived pores are observed, consistent with reports of other investigators. These observations are discussed in terms of the phase transformation processes caused by the different crystallization behavior of the diluents.

## 2.1. Introduction

Thermally induced phase separation (TIPS) processes are widely used to prepare microporous polymeric membranes due to their simplicity and ability to control phase separation.<sup>21-22</sup> Typical TIPS processes proceed by either liquid-liquid phase separation, resulting in a polymer-rich continuous phase and a polymer-lean droplet phase, or by liquid-solid (L-S) phase separation, in which the polymer solidifies from solution.<sup>22</sup> Systems exhibiting an upper critical solution temperature (UCST), in which a homogeneous mixture of a polymer with a diluent at an elevated temperature does not form a single phase at a lower temperature are often used.<sup>23</sup> In these cases, the homogeneous polymer solution undergoes L-L phase separation upon cooling. The droplet phase, composed of nearly pure diluent, is uniformly dispersed in the polymer-rich matrix phase, and can be removed from the solidified mixture to yield a cellular structured microporous membrane. Since the droplet phase determines the cellular structure of the porous membrane, the cellular morphology of the membrane can be controlled by changing temperature profiles and using a variety of combinations of polymers and diluents.<sup>24</sup> While there is a significant literature regarding this control,<sup>21-26</sup> relatively little effort has been expended to control the shape of the pores. Narkis et al. observed three modes of crystallization (needle-like, dendritic and tiny crystalline particles) when low molecular weight organic compounds were used in amorphous polymers.<sup>27</sup> Smith et al. reported a rodlike eutectic microstructure from the quasi binary system of unfractionated isotactic polypropylene and the dendritic growing diluent, pentaerythrityl tetrabromide.<sup>28</sup> This group also reported cleaved, truncated HMB needles grown in a polyethylene matrix.<sup>29</sup> Alwattari et al. used isotactic polypropylene

blended with HMB to investigate the effects of melt composition and crystallization temperature on the microstructure of the resulting membranes, which were composed of rectangular pores with secondary needle-like structures.<sup>30</sup> It is not, however, clear how different high melting, crystallizable diluents lead to different morphologies or how this process might be used to control structure in porous materials.

This chapter describes research aimed at the preparation and characterization of porous polymeric materials with controlled pore shape and size using linear low density polyethylene (LLDPE) in combination with high melting diluents, pyrene and hexamethylbenzene (HMB). Different morphologies of the resulting porous structures were investigated and discussed in terms of phase diagrams and crystallization behaviors of each diluent in the polymer solutions. These studies suggest that crystallizable diluents may be useful for polymer structure control.

## **2.2. Materials and Sample Preparation**

### **2.2.1. Materials**

Linear low density polyethylene (Dowlex LLDPE-2553) was obtained from Dow Chemical. Pyrene (98% purity) and HMB (99% purity) were purchased from Fisher Scientific and used without further purification. The crystallizable diluents were selected by considering their melting temperatures and structural similarity with the known solvents for polyethylene (e.g. xylenes). Information about the crystallography of the diluents can be found in the literature.<sup>31-32</sup> The molecular weight of the polyethylene was determined by gel permeation chromatography (GPC, PL-GPC 220)

at 145 °C using trichlorobenzene as the elution solvent. Thermal properties were determined by differential scanning calorimetry (DSC-2910, TA instruments) at 5 °C/min heating and cooling rates. Other properties are obtained from referenced literature and summarized in Table 2.1.

**Table 2.1.** Materials properties

Properties	Units	LLDPE	HMB	Pyrene
Molecular Weight	g / mol	18,000 (Mn) 108,000 (Mw)	162	202
Degree of Polymerization	-	642	N/A	N/A
Molar Volume	cm <sup>3</sup> / mol	33.03 <sup>a</sup> (ethylene unit)	175 <sup>b</sup>	179 <sup>c</sup>
Density	g / cm <sup>3</sup>	0.935	0.926 <sup>b</sup>	1.27
Heat of Fusion	J / mol	3,780 (ethylene unit)	21,840	17,310
Melting Temperature	K (°C)	402 (129)	440 (167)	426 (153)
Crystallization Temperature	K (°C)	382 (109)	436 (163)	394 (121)
Solubility Parameter	MPa <sup>1/2</sup>	17 <sup>d</sup>	17 <sup>b</sup>	20.7 <sup>c</sup>

<sup>a</sup>Representative value from reference.<sup>33</sup>

<sup>b</sup>Experimental value from reference.<sup>34</sup>

<sup>c</sup>Experimental value from reference.<sup>35</sup>

<sup>d</sup>Representative value from references.<sup>33, 36</sup>

### 2.2.2. Sample Preparation

LLDPE powder was prepared by dissolution of the provided pellets in refluxing xylene, precipitation in excess methanol, and subsequent drying in a vacuum oven at 80 °C overnight. The powdered sample obtained was mechanically crushed to prepare free flowing powders. Pyrene and HMB were crushed to make fine powders. Diluent powder samples were premixed with LLDPE powder in various compositions in a glass vial to yield a total weight of  $1 \pm 0.05$  g. The vials were purged with nitrogen for 30 minutes, sealed (screw cap) and immersed in an oil bath at 200 °C for 10 hours. Compositions prepared ranged from 10 to 90 wt.% diluent at 5~10 wt.% intervals. After completion of thermal mixing, samples were rapidly cooled by immersion in liquid nitrogen to prevent macroscopic phase separation. Quenched samples were chopped and weighed before being used to make plaque specimens with a compression molding machine (PW2256, PHI). Each sample was weighed into a square mold (25 mm x 25 mm, 0.5 mm in thickness), melted at 200 °C for 3 minutes under 35 MPa pressure, and then cooled rapidly using a second compression molder (Carver Laboratory Press) which was maintained at 20 °C and operated under 35 MPa pressure. The composition of each sample after the compression molding was determined by thermal gravimetric analysis (TGA-2950, TA instruments, Figure 2.1). Diluents were removed by overnight Soxhlet extraction using appropriate solvents (methanol for pyrene, acetone for HMB). After extraction, samples were dried in a vacuum oven at 60 °C overnight. The extraction efficiency was checked by TGA and found to be higher than 95% for all samples.

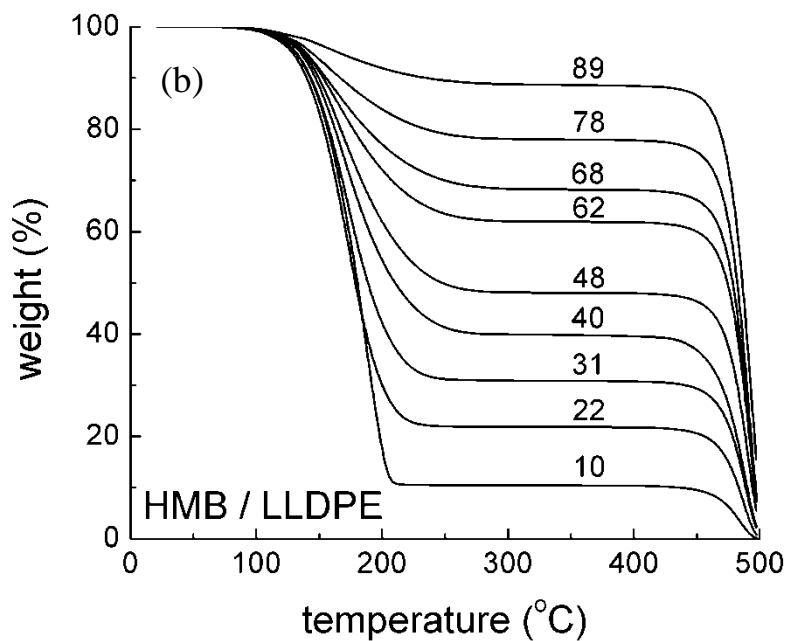
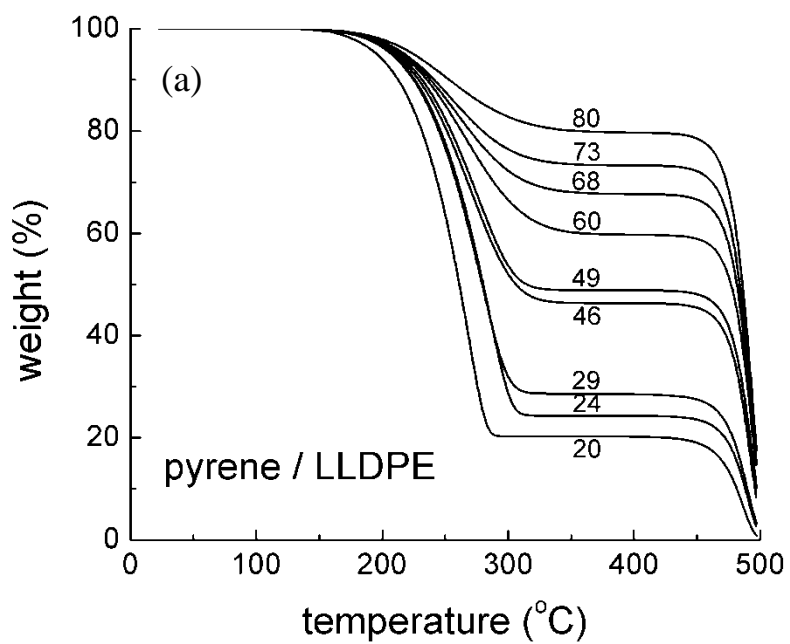


**Figure 2.1.** Thermal gravimetric analysis (TGA) to determine the composition of the mixtures. (a) pyrene / LLDPE mixtures, (b) hexamethylbenzene / LLDPE mixtures.

## **2.3. Experimental**

### **2.3.1. Thermal Analysis**

Differential scanning calorimetry (DSC-2910, TA instruments) was used to determine the melting and crystallization temperatures. Each diluent-polymer mixture sample was hermetically sealed in an aluminum DSC pan, heated from 25 °C to 200 °C at 10 °C/min and maintained at 200 °C for 3 minutes. Samples were then cooled to 50 °C at 5 °C/min to measure crystallization temperature. Samples were heated again to 200 °C at 5 °C/min to measure melting temperature. Peak maxima were taken as melting and crystallization temperatures.

### **2.3.2. Optical Microscopy**

An Olympus BX51 microscope was used to visualize the phase separation process. A small section was sliced from each diluent-polymer mixture sample and placed between pairs of microscope slides. The edges of the slides were sealed with Teflon tape to prevent material loss by evaporation. A hot stage (Linkam TMS-93) with a temperature controller (Linkam THMS-600) was used to heat the sample at 5 °C/min to 200 °C at which temperature they were maintained for 3 minutes, and then cooled to 30 °C at 5 °C/min. The thermocouple for temperature measurement was located near the heating block of the hot stage and the slide/sample assemblies were not insulated, thus the actual temperature of the sample is lower than that recorded by the thermocouple. This issue was addressed by calibrating the temperature reading from the thermocouple using several organic molecules with sharp melting temperatures (naphthalene: 80.6 °C, phthalic anhydride: 130.8 °C, pyrene: 156 °C, hexamethylbenzene: 164 °C) in the

temperature range suitable for our experiments (Figure 2.2). Temperatures at which the sample suddenly became turbid and/or diluent crystals began to grow in the polymer-rich matrix were recorded.

### 2.3.3. Scanning Electron Microscopy (SEM)

Morphology of the cross-sections of the samples after removal of the diluents was examined by field emission scanning electron microscopy (JEOL FX-6210) with an accelerating voltage of 10 kV. Cross-sections of the samples were prepared by immersion in liquid nitrogen (5 minutes) followed by fracture of the samples (sharp razor blade). The exposed cross-section was coated with Au using a sputter coating instrument (Cressington Sputter Coater 108). SEM images were obtained from at least 5 different locations on each sample.

## 2.4. Results and Discussion

### 2.4.1. Equilibrium Phase Diagrams

Equilibrium phase diagrams were calculated for binary mixtures of pyrene/LLDPE and HMB/LLDPE based on Flory-Huggins solution thermodynamics. Details of the methods used can be found in Chapter 1. Theoretical melting temperature depression of LLDPE in which a crystalline LLDPE is in equilibrium with a polymer solution is calculated using equation 1.10 as derived in Chapter 1,

$$\frac{1}{T_m} = \left[ 1 + \frac{R\beta}{\Delta H_u} \left( \frac{V_u}{V_1} \right) (1 - \phi_2)^2 \right]^{-1} \left[ \frac{1}{T_m^0} + \frac{R}{\Delta H_u} \left( \frac{V_u}{V_1} \right) \left\{ \left( 1 - \frac{1}{N} \right) (1 - \phi_2) - \frac{\ln(\phi_2)}{N} \right\} \right] \quad (1.10)$$

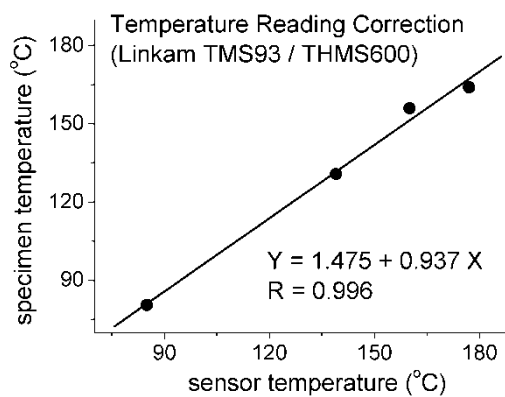
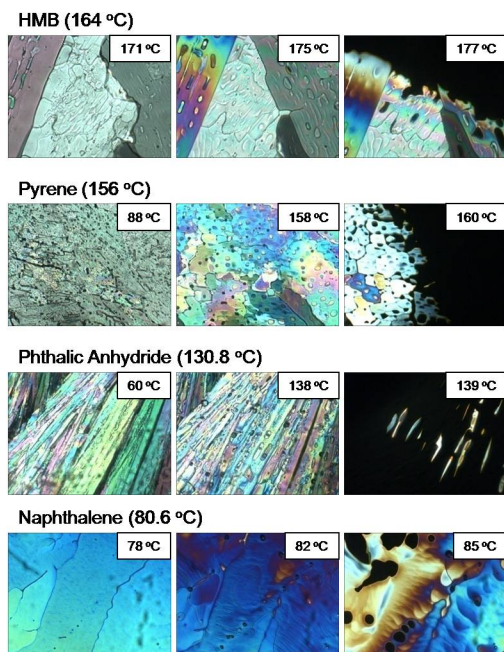
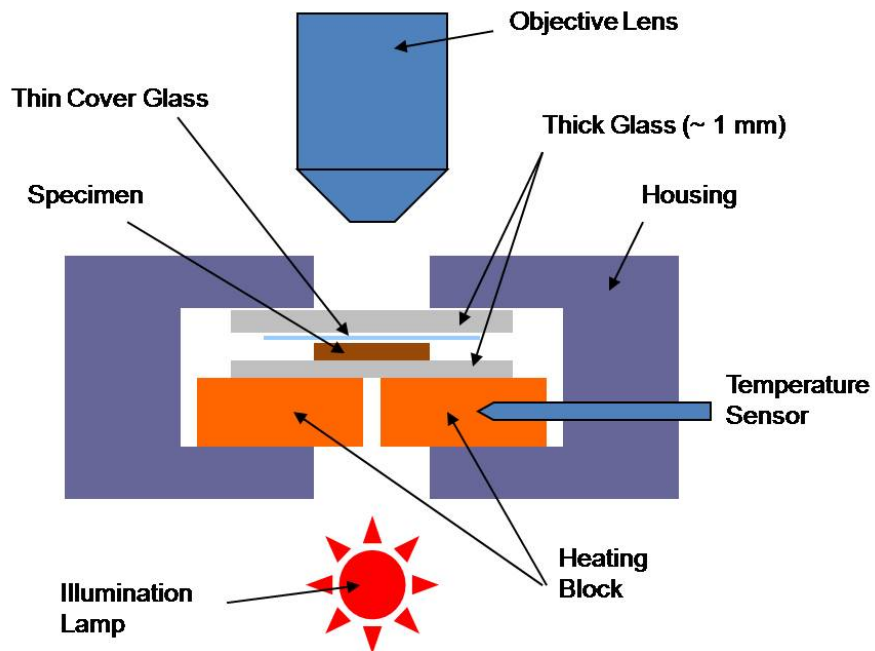


**Figure 2.2.** Temperature calibration using organic molecules with sharp melting points.

where  $T_m$  is the melting temperature of LLDPE in a polymer solution,  $T_m^0$  is the melting temperature of neat LLDPE,  $\Delta H_u$  is the enthalpy of fusion per repeat unit of LLDPE,  $N$  is degree of polymerization,  $\phi_2$  is the volume fraction of LLDPE,  $R$  is the gas constant and  $\beta$  is a constant which is calculated from the solubility parameters of LLDPE ( $\delta_2$ ) and diluent ( $\delta_1$ ) along with the molar volume of diluent ( $V_1$ ), using the equation  $(\delta_1 - \delta_2)^2 V_1 / R$ . Six ethylene units are considered as a repeat unit so that the molar volume of LLDPE repeat unit ( $V_u$ ) and that of diluent ( $V_1$ ) are similar, as assumed in Flory-Huggins theory. Thus, the values of the degree of polymerization ( $N$ ), enthalpy of fusion ( $\Delta H_u$ ) and molar volume of LLDPE repeat unit ( $V_u$ ) in equation 1.10 are adjusted by considering six ethylene units as a repeat unit. Similarly, the melting temperature depression of diluent in which the crystalline diluent is in equilibrium with the polymer solution is calculated using equation 1.14 as derived in Chapter 1,

$$\frac{1}{T_{m,1}} = \left[ 1 + \frac{R\beta\phi_2^2}{\Delta H_1} \right]^{-1} \left[ \frac{1}{T_{m,1}^0} - \frac{R}{\Delta H_1} \left\{ \left( 1 - \frac{1}{N} \right) \phi_2 + \ln(1 - \phi_2) \right\} \right] \quad (1.14)$$

where  $T_{m,1}$  is the melting temperature of crystalline diluent in a polymer solution,  $T_{m,1}^0$  is the melting temperature of neat diluent and  $\Delta H_1$  is the enthalpy of fusion for neat diluent. Experimental values of melting temperatures measured using DSC at a 5 °C/min heating rate show good agreement with calculated results as shown in Figures 2.3 and 2.4. Since the melting temperature ( $T_m$ ) depression as represented by the liquidus lines in Figures 2.3 and 2.4 is a colligative property,  $T_m$  depression of the diluent depends on the ‘number’ of molecules of the polymer and vice versa. Due to the high molecular weight of the polymer, the melting point of the diluent does not decrease sharply as the volume fraction of the polymer increases while that of the polymer

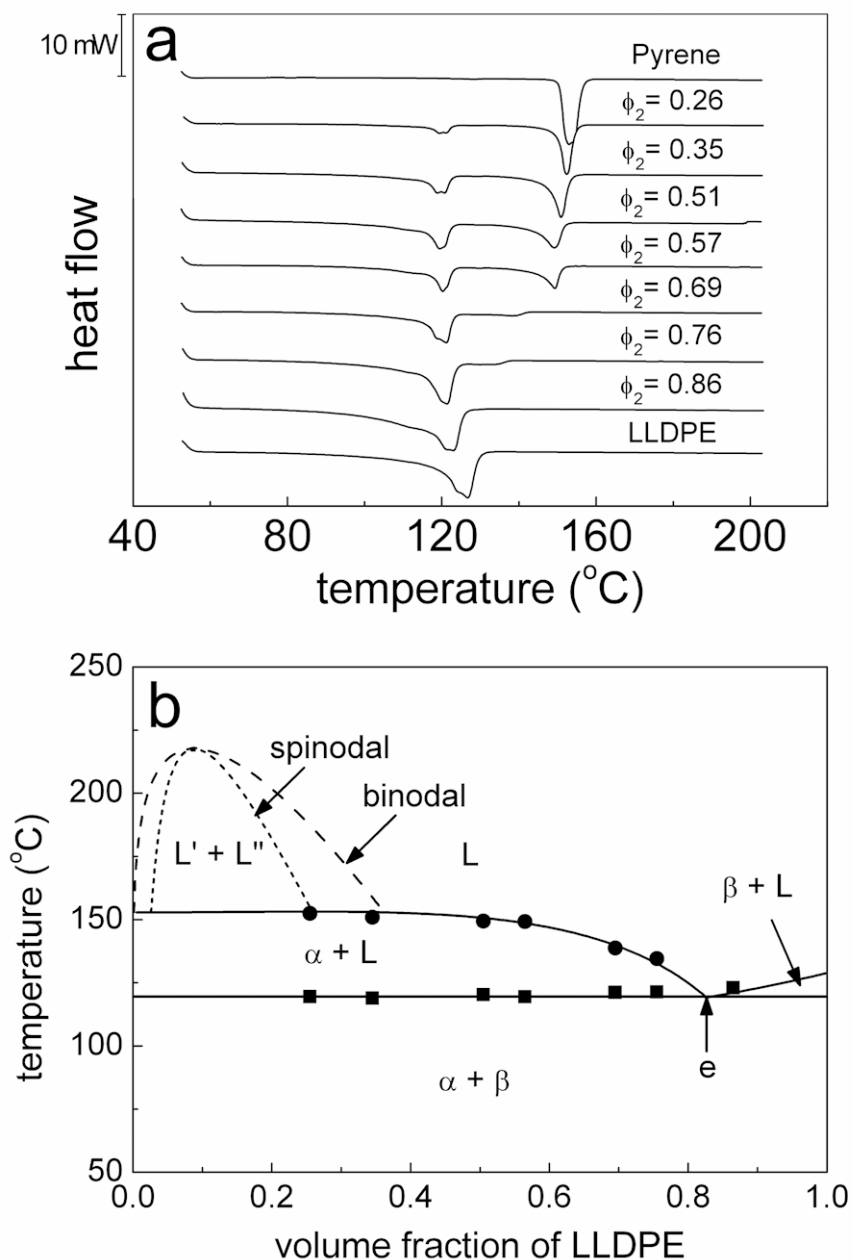


**Figure 2.3.** Thermal analysis results for mixtures of pyrene and LLDPE. (a) DSC thermograms of selected mixtures for melting temperature determination; heating rate was 5 °C/min;  $\phi_2$  is LLDPE volume fraction, (b) melting temperature plotted on the calculated equilibrium phase diagram.  $\alpha$ : solid pyrene;  $\beta$ : solid LLDPE; L, L', L'': liquid mixture of pyrene and LLDPE. Note that L-L demixing (binodal, spinodal) was not confirmed under these experimental conditions.

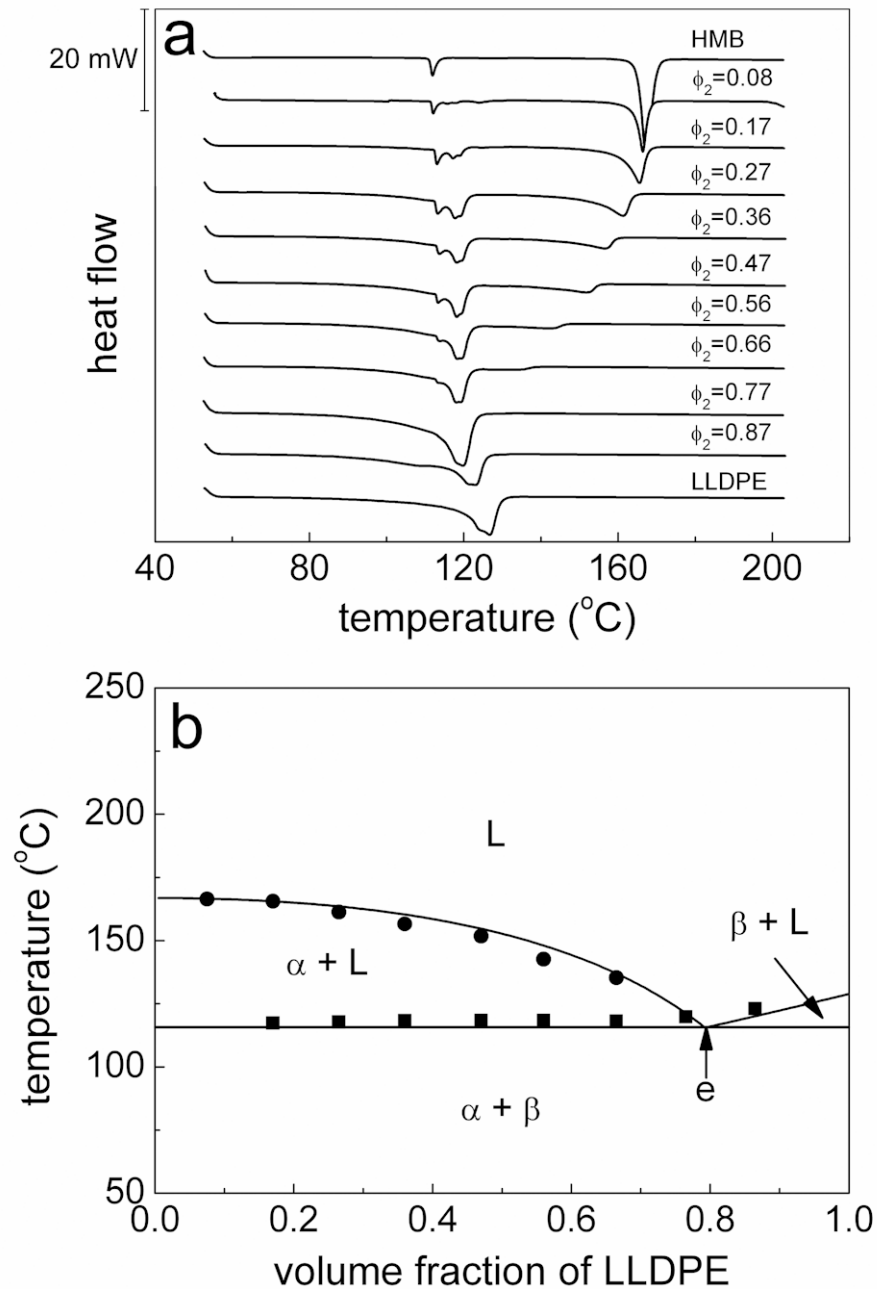


**Figure 2.4.** Thermal analysis results for mixtures of HMB and LLDPE. (a) DSC thermograms of selected mixtures for melting temperature determination; heating rate was 5 °C/min;  $\phi_2$  is LLDPE volume fraction, (b) melting temperature plotted on the calculated equilibrium phase diagram.  $\alpha$ : solid HMB;  $\beta$ : solid LLDPE; L: liquid mixture of HMB and LLDPE.

decreases relatively sharply as the volume fraction of the diluent increases because of the low molecular weight of the diluent. As a result, the eutectic composition (marked 'e' in Figures 2.3 and 2.4) is located in the polymer-rich regime. The resulting equilibrium phase diagrams suggest that phase separation is most likely induced by the crystallization of the diluent rather than that of the polymer, unless the initial composition is highly polymer-rich.

If the polymer content in the initial mixture is lower than the eutectic composition, phase separation is initiated by the crystallization of the diluent upon cooling. Under the idealized equilibrium crystallization conditions, the diluent will begin to crystallize and will be precipitated from the polymer solution when the temperature reaches the melting temperature of the diluent at that composition. Upon further cooling, more crystals of diluent will be formed from the liquid solution, causing the polymer content in the liquid solution to increase until it reaches the eutectic composition. Both the polymer and the diluent crystallize at the same time when the composition of the liquid solution reaches the eutectic composition. Eutectic transformation ( $L \rightarrow \alpha + \beta$ ) occurs at a constant temperature, shown as eutectic horizontal lines in Figures 2.3b and 2.4b, because of the zero degree of freedom at that condition.<sup>4</sup> Gibb's phase rule at fixed pressure states that  $F = C - P + 1$  (F: degree of freedom, C: number of components, P: number of phases) and  $F = 0$  at eutectic conditions since there are two components ( $C = 2$ ) and three phases (L,  $\alpha$ ,  $\beta$ ) coexisting ( $P = 3$ ), making the temperature invariant. It should also be noted that solid solubility (solubility of solid solute in solid solvent) is assumed to be negligible in Figures 2.3b and 2.4b because of the significant difference in crystal structure and size between the

polymer and each diluent; crystals of each component are assumed to be pure, which is often the case for organic binary mixtures.<sup>37</sup>

Due to the poor solvent quality of pyrene for LLDPE, mixing becomes difficult as the pyrene content increases. Since the  $\chi$  parameter is a function of temperature and solvent quality improves as temperature increases for these mixtures, thermal mixing was carried out at as high as 200 °C. The mixing temperature is limited by the thermal stability of pyrene; at temperatures higher than 200 °C, severe discolorization of pyrene is observed. The highest possible content of pyrene in the mixture is about 75% by volume; homogeneous mixtures of greater pyrene concentration cannot be formed at 200 °C. Since the calculated phase diagram predicts L-L de-mixing at 200 °C if the volume fraction of pyrene is greater than 0.8, incomplete mixing in this composition regime is most likely due to L-L de-mixing. However, L-L de-mixing (Figure 2.3b) could not be confirmed experimentally due to the thermal instability of pyrene. In contrast, mixing is straight-forward for HMB and LLDPE due to their good miscibility and similar densities in the liquid state. Since the solubility parameters of LLDPE and HMB are identical, L-L de-mixing is not expected. Neat HMB as received from Fisher Scientific exhibits two melting peaks, a major one at 167 °C and a minor one at 112 °C (Figure 2.4a); the minor peak is assumed to be caused by impurities and is ignored in the analysis.

#### **2.4.2. Phase Separation by Crystallization.**

Analyses in the previous section are from a solely thermodynamic perspective and kinetic factors could be important if the cooling is fast and thermodynamic equilibrium is not maintained during crystallization. Under non-equilibrium cooling

conditions, both composition and temperature distribution in each phase may not be uniform. In this regard, dynamic crystallization processes were investigated using DSC and optical microscopy. The difference in crystallization behavior between pure pyrene and pure HMB is shown in Figure 2.5. HMB nucleates easily and crystallizes with relatively little supercooling while pyrene requires significant supercooling for crystallization. The width of the crystallization peak suggests that HMB crystallizes relatively slowly while pyrene crystallizes very quickly. These differences in crystallization kinetics may be intrinsic properties of the diluents or due to impurities functioning as nucleating agents; regardless the kinetics are reproducible. The crystallization characteristics of each diluent directly affect the crystallization behavior of the mixtures of LLDPE with pyrene and HMB. The effect of the diluent identity on the phase separation process is emphasized in Figure 2.6 that shows data for HMB and pyrene samples with the same LLDPE volume fraction ( $\phi_2 = 0.25$ ). It is evident from Figure 2.6a that the temperature at which pyrene crystallizes in the polymer solution is much lower than that of HMB (127 °C vs 159 °C). Also apparent in Figure 2.6a is that the width of the crystallization peak of pyrene for the pyrene/LLDPE mixture is significantly narrower than that of HMB for the HMB/LLDPE mixture. This indicates that the crystallization rate of pyrene in the pyrene/LLDPE mixture is much higher than that of HMB in the HMB/LLDPE mixture. Optical microscopy shows that the solidification of pyrene is characterized by dendritic growth with a much higher rate than that of HMB (Figure 2.6b). Solidification of pyrene can be explained by the general theory of dendritic solidification,<sup>38-41</sup> which is characterized by a morphology

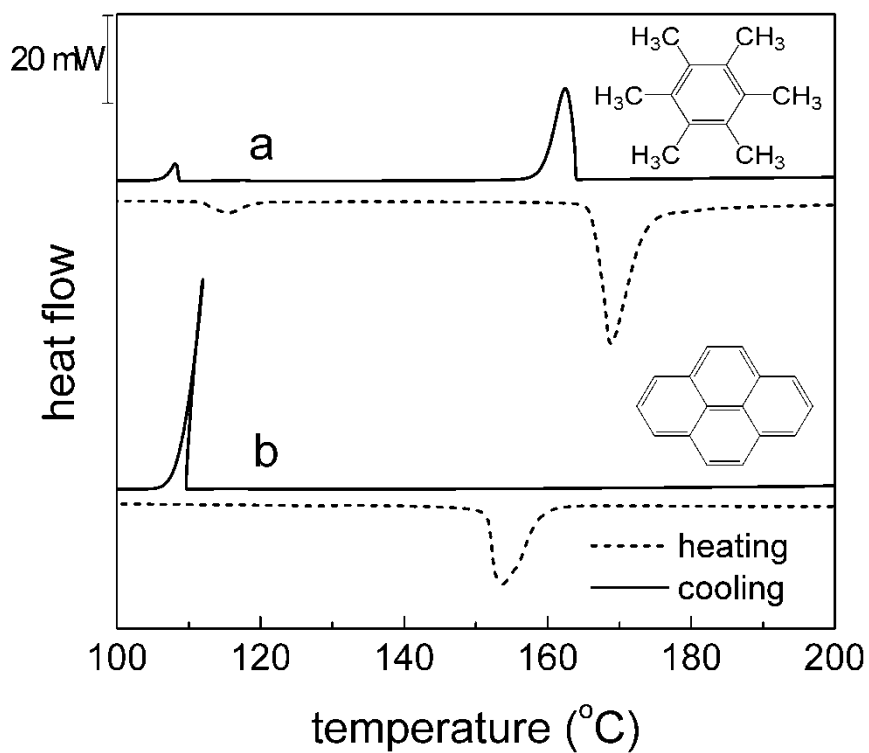


**Figure 2.5.** DSC melting (dashed lines) and crystallization (solid lines) thermograms of pure diluents at 5 °C/min heating and cooling rates. (a) HMB, small melting peak at around 120 °C and small crystallization peak at around 110 °C are assumed to be from impurities, (b) pyrene.

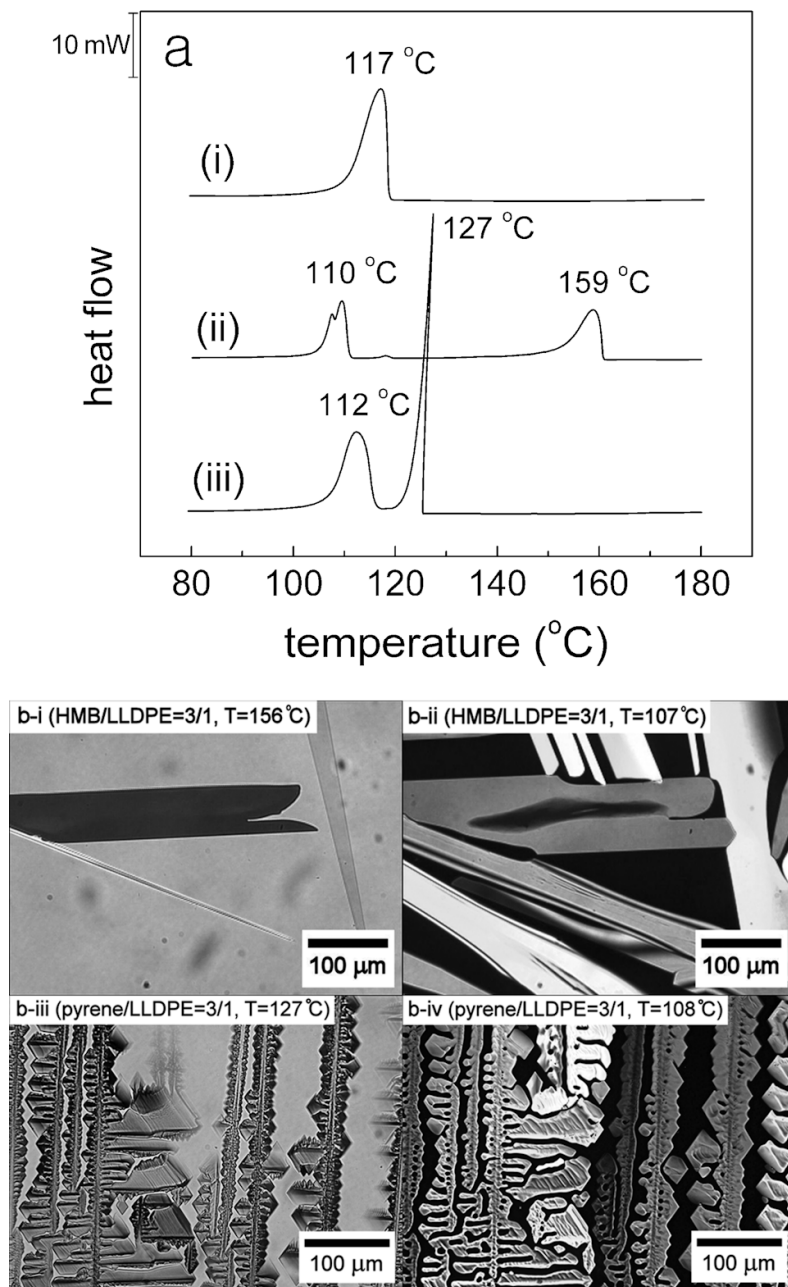


**Figure 2.6.** Crystallization process analysis for binary mixtures of LLDPE with HMB and pyrene. The volume fraction of LLDPE in the mixture was fixed at  $\phi_2 = 0.25$ . (a) crystallization peaks from DSC obtained at a cooling rate of 5 °C/min, (i): neat LLDPE, (ii) HMB/LLDPE, (iii) pyrene/LLDPE, (b) micrographs from optical microscopy. Samples were cooled from 200 °C to 30 °C at a 5 °C/min cooling rate, (i) crystallization of HMB began at 156 °C for HMB/LLDPE, (ii) crystallization of HMB was complete at 107 °C for HMB/LLDPE (cross-polarized image), (iii) crystallization of pyrene began at 127 °C for pyrene/LLDPE, (iv) crystallization of pyrene was complete at 108 °C for pyrene/LLDPE (cross-polarized image).

resulting from the growth of long, thin spikes in specific crystallographic directions, with regular branches in other equivalent directions. It is known that dendritic growth takes place when, and only when the melt is supercooled and the growth rate is determined by the supercooling (temperature difference between the actual temperature of the interface and the equilibrium temperature). Experimental results in the literature indicate that the advancing rate of the tip of a dendrite ( $v$ ) is roughly proportional to the square of supercooling ( $(\Delta T)^2$ ).<sup>38</sup> This is in qualitative agreement with our observation that pyrene, which crystallizes after significant supercooling, shows fast dendritic solidification while HMB, which crystallizes after a much lower degree of supercooling, shows slow non-dendritic solidification.

The solid-liquid interface present during crystallization of diluents was further investigated by polarized optical microscopy as shown in Figure 2.7. Thin ( $\sim 10 \mu\text{m}$ ) samples of diluent/LLDPE (3/1, w/w) mixtures were quickly quenched from 200 °C to 20 °C so that the crystallization process would be kinetically trapped and could be observed. Figure 2.7a shows that HMB easily nucleates and that crystals of HMB grow in random orientation in the liquid phase. Both HMB crystals and LLDPE spherulites are seen in the liquid phase near the solid-liquid interface, indicating that both components crystallize independently in the same region. In contrast, pyrene shows dendritic growth and new crystals do not form in the liquid phase (Figure 2.7b). Only LLDPE spherulites are seen in the liquid phase. Dendritic growth of pyrene is observed and crystallization proceeds into the highly supercooled liquid. The heat of crystallization (generated in the solid-liquid interface where crystallization takes place)

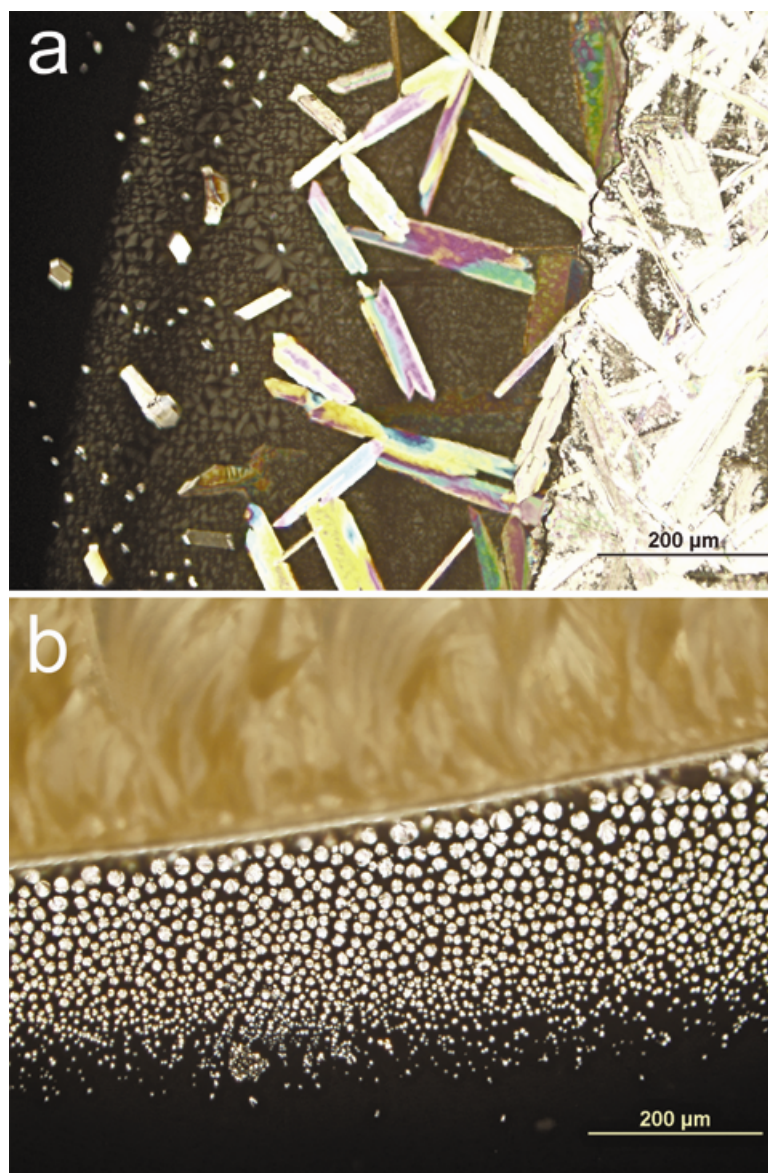


**Figure 2.7.** Polarized optical microphotographs of the solid-liquid interface. Thin samples of diluent/polymer (3/1, w/w) mixtures were quickly quenched from 200 °C to 20 °C. (a) HMB / LLDPE, (b) pyrene / LLDPE.

causes the temperature of the S-L interface to be higher than that of the neighboring phases. Temperature gradients decreasing in both directions away from the S-L interface into both solid and liquid phases are present. Initially flat S-L interfaces tend to undergo fluctuation that is induced by thermal and/or concentration field if the crystallization is fast and/or is limited by diffusion. In these situations, any projection into the supercooled liquid experiences a lower temperature than the unperturbed interface, and crystallization of the projected tip is accelerated. Thus a flat interface between a crystallizing solid and a supercooled liquid is inherently unstable and dendritic growth of crystals occurs. Since the crystallization of pyrene takes place under highly supercooled condition and the crystallization rate is very high, a significant amount of heat due to crystallization is rapidly generated at the S-L interface and the resulting temperature gradient leads to strong dendritic growth of pyrene crystals.

Figure 2.7b also shows that the size of the LLDPE spherulites decreases as the distance from the interface increases. The concentration of LLDPE in the liquid phase would be highest near the interface (due to consumption of pyrene caused by crystallization) and decreases with distance from the interface. The resulting size distribution of LLDPE spherulites is likely due to this concentration gradient. Eutectic solidification in the liquid phase is not expected under the fast-cooling condition since significant inhomogeneity in concentration and temperature distribution exists in the liquid phase.

Samples with different compositions show similar behavior. DSC thermograms in cooling runs and measured crystallization temperatures are shown in Figure 2.8. The gap between crystallization temperatures of pyrene and LLDPE decreases as the volume

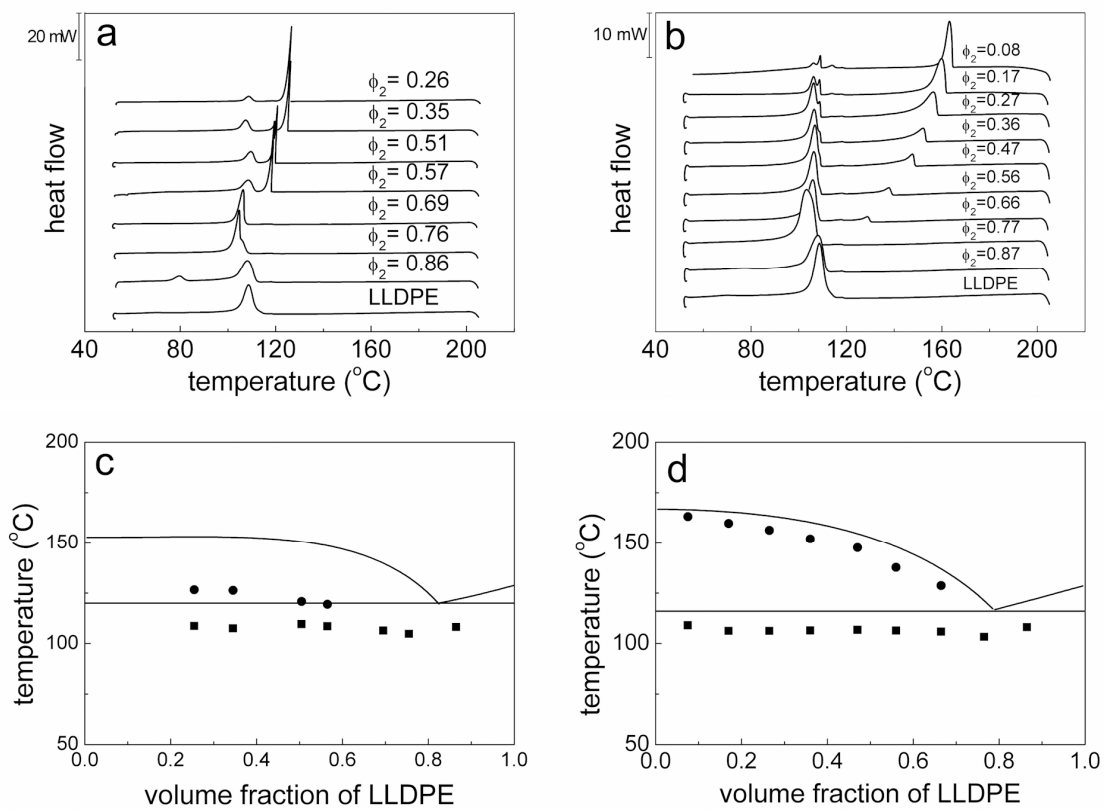


**Figure 2.8.** Crystallization temperatures determined by DSC cooling at a 5 °C/min scanning rate. (a) pyrene and LLDPE mixtures, (b) HMB and LLDPE mixtures, (c) crystallization temperature of mixtures of pyrene and LLDPE plotted on the calculated equilibrium phase diagram, (d) crystallization temperature of mixtures of HMB and LLDPE plotted on the calculated equilibrium phase diagram.

fraction of LLDPE increases (Figures 2.8a and 2.8c) until it reaches the eutectic composition, after which only one crystallization temperature is observed. A similar trend is observed for the crystallization of HMB/LLDPE mixtures (Figure 2.8b and 2.8d). The gaps between the two crystallization peaks of the HMB/LLDPE mixtures are larger than those of pyrene/LLDPE mixtures at similar composition levels.

The crystal growth of diluents in samples with different compositions as observed by optical microscopy is shown in Figures 2.9 and 2.10. Dendritic solidification is clearly seen for pyrene/LLDPE mixtures when the initial composition is pyrene-rich (Figures 2.9a – 2.9d). Dendrite arms grow in specific crystallographic directions, these being uniquely determined by the crystal structure of pyrene.<sup>42</sup> The reason for this observation is not fully understood, but the dendrite direction has been interpreted simply as the fastest growing direction that is determined by the crystal structure of pyrene.<sup>37</sup> As the LLDPE content increases and the initial composition of the mixture approaches the eutectic composition, both components tend to crystallize competitively. Since the eutectic composition is located far from the 50/50 (pyrene/LLDPE) composition, irregular or needle-like solidification is observed in eutectic solidification (Figures 2.9e – 2.9j).<sup>38</sup> Due to their different crystal structure and size, both components apparently crystallize independently. Figures 2.9e, 2.9g and 2.9i show that the phase separation is initiated by LLDPE crystallization promptly followed by pyrene crystallization and both components crystallize at the same time (eutectic solidification), which is observed as one crystallization peak in DSC cooling experiments (Figure 2.8a). In the case of HMB/LLDPE mixtures, dendritic solidification of HMB is less obvious due to the small supercooling for crystallization.

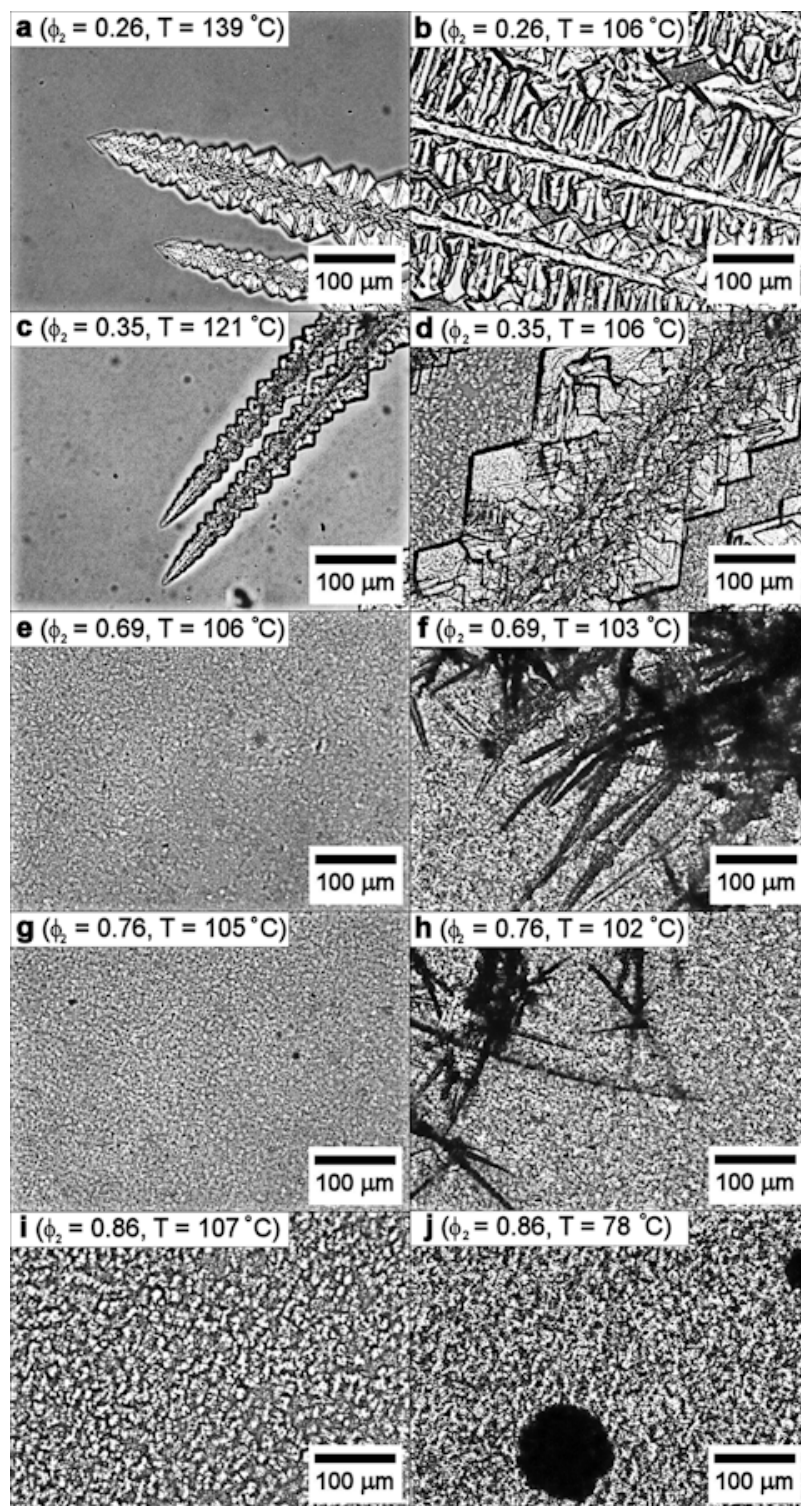


**Figure 2.9.** Optical microscopy images of pyrene/LLDPE mixtures. Samples were cooled from 200 °C to 30 °C at 5 °C/min.  $\phi_2$  is the volume fraction of LLDPE.

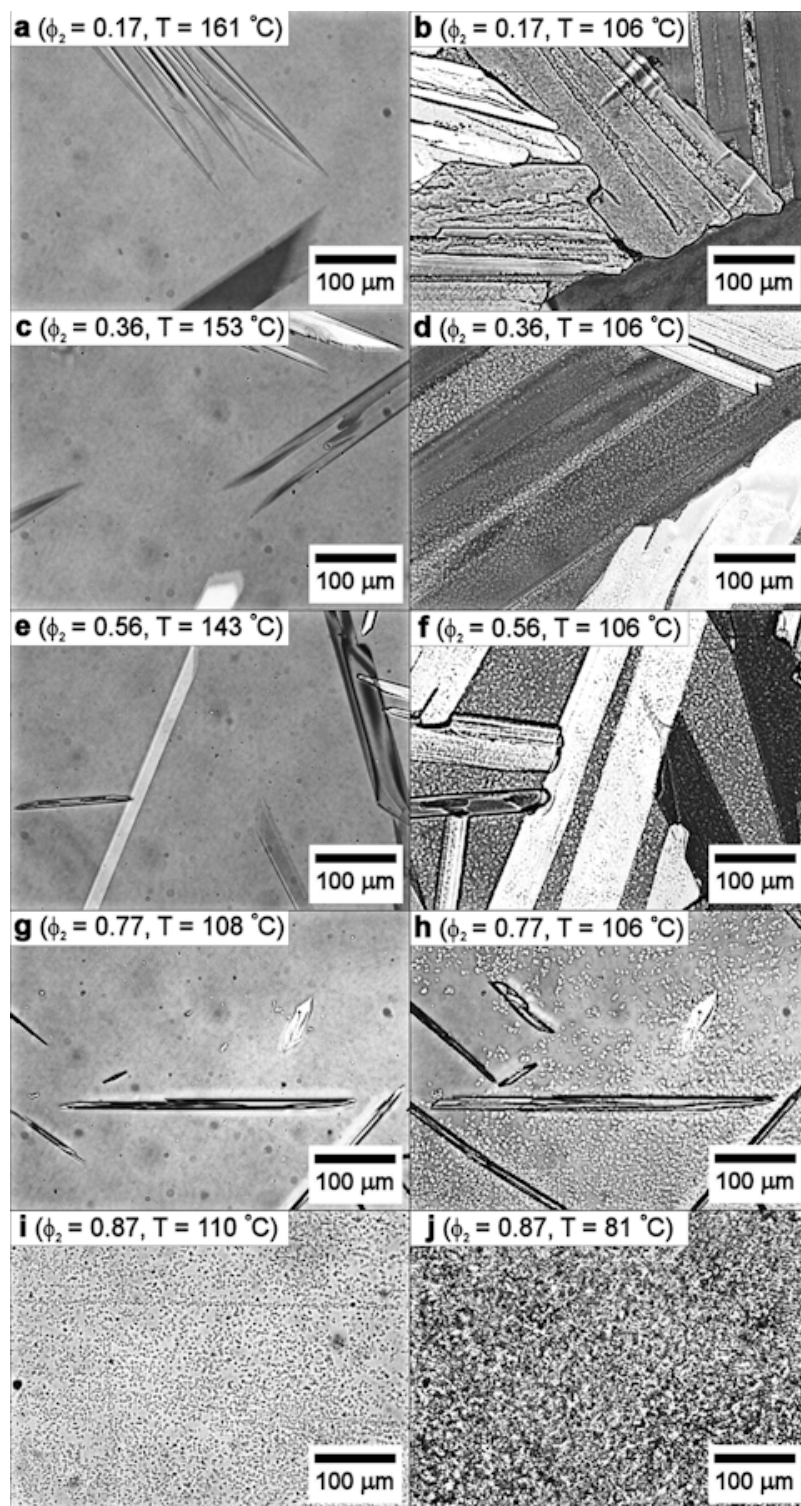


**Figure 2.10.** Optical microscopy images of HMB/LLDPE mixtures. Samples were cooled from 200  $^\circ\text{C}$  to 30  $^\circ\text{C}$  at 5  $^\circ\text{C}/\text{min}$ .  $\phi_2$  is the volume fraction of LLDPE.

Phase separation is initiated by the crystallization of HMB unless the initial LLDPE content in the mixture is greater than the eutectic composition (Figures 2.10a – 2.10f). In this case, plate-like or needle-like crystals of HMB without any higher order branches are observed. When the initial composition is close to the eutectic composition, both components crystallize competitively, but independent of each other (Figure 2.10g, 2.10h).

If the LLDPE content in the mixture is higher than the eutectic composition, phase separation is initiated by LLDPE; HMB crystallization is not obvious in this case (Figures 2.10i, 2.10j). These observations indicate that the morphology as determined by the phase separation process strongly depends on the identity of the crystallizable diluents as well as the initial composition of the mixtures.

### **2.4.3. Morphology**

Figure 2.11 shows SEM micrographs of fractured cross-sections taken from mixtures of LLDPE and pyrene after extraction of pyrene. Porous structures inside of each sample were formed by the crystallization of pyrene; the pores were occupied by pyrene crystals prior to extraction. Phase separation is triggered by the crystallization of pyrene for pyrene-rich samples as shown in the DSC and optical microscopy experiments (Figures 2.8 and 2.9) and the resulting porous morphology reflects the crystal growth characteristics of pyrene. The resulting porous material shows locally aligned porous layers stacked together (Figure 2.11a). As observed by optical microscopy, pyrene crystals grow in relative preferential directions. As the amount of pyrene in the sample decreases, less pyrene is available for crystal growth and the resulting porous structure becomes smaller in size and each porous layer is not vacant

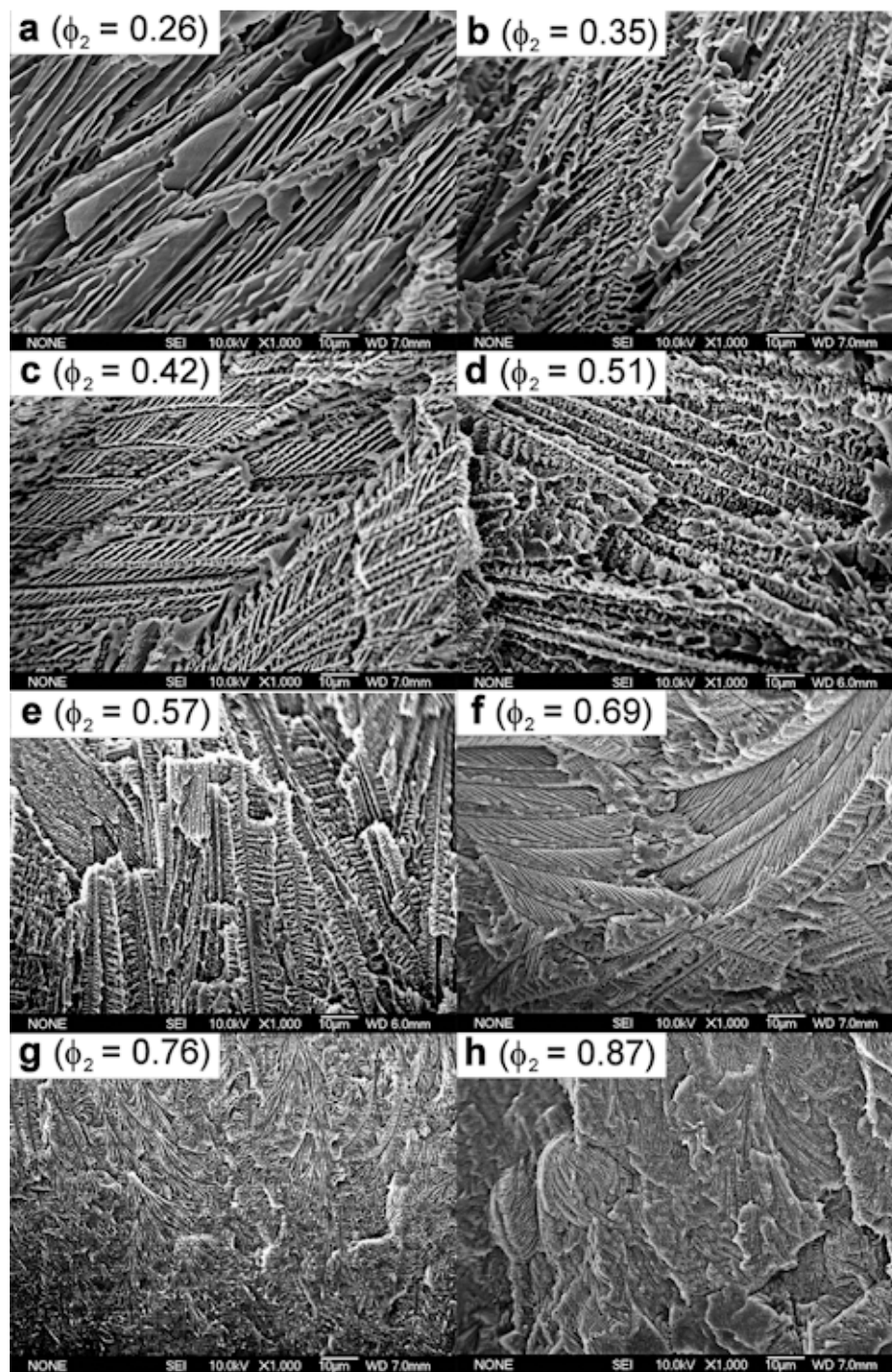


**Figure 2.11.** SEM micrographs showing the morphology of fractured cross-sections of pyrene/LLDPE mixtures after extraction of pyrene.  $\phi_2$  represents the volume fraction of LLDPE.

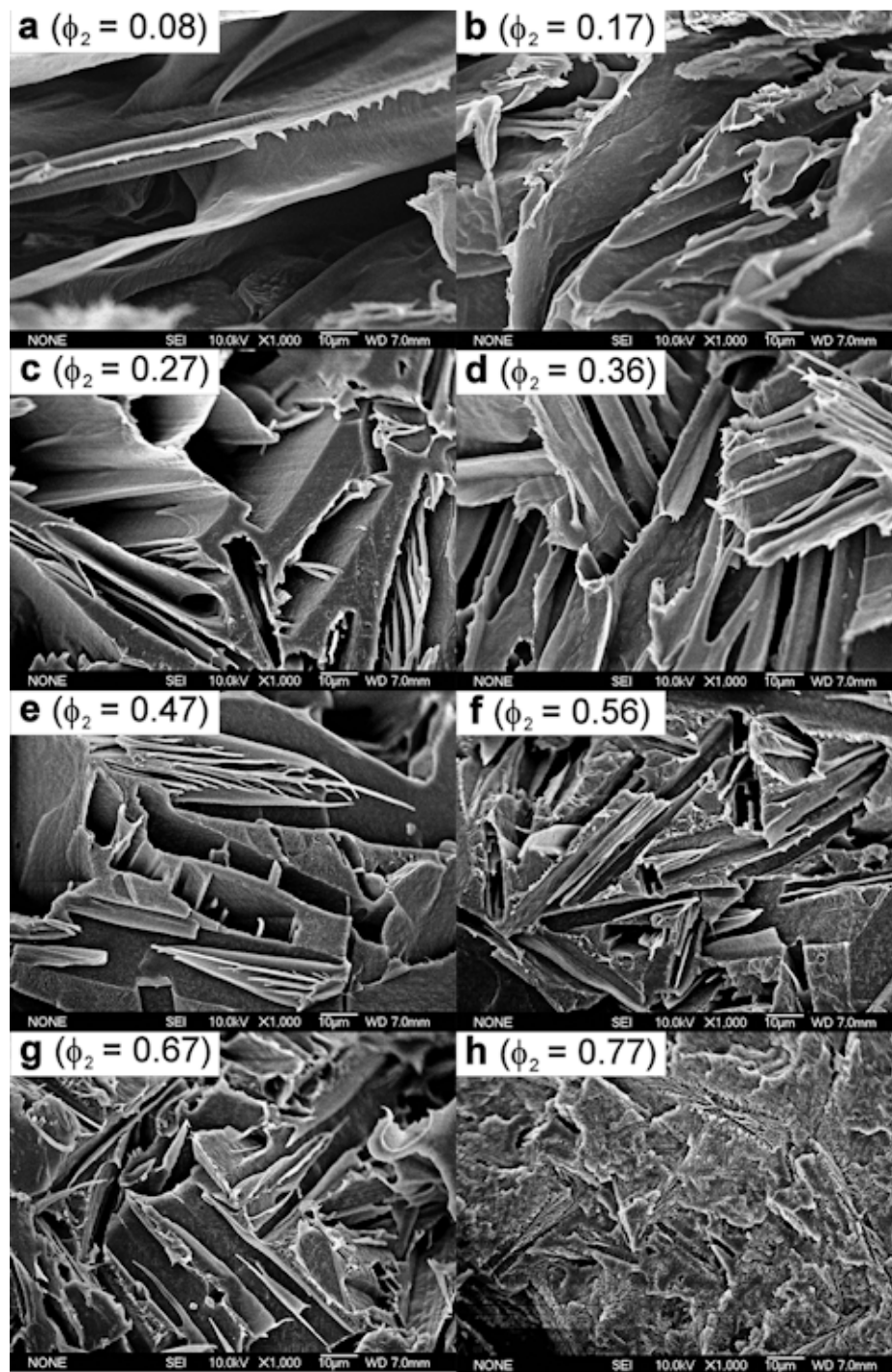


**Figure 2.12.** SEM micrographs showing the morphology of fractured cross-sections of HMB/LLDPE mixtures after extraction of HMB.  $\phi_2$  represents the volume fraction of LLDPE.

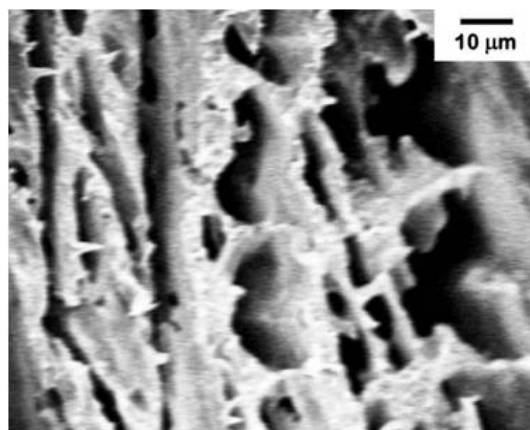
but is filled with smaller pores (Figures 2.11b and 2.11c). Preferential direction of crystal growth is still apparent. When pyrene concentration is further decreased so that the LLDPE volume fraction in the sample is 0.51 and 0.57, pore size becomes even smaller and the internal structure inside each porous layer becomes more complex (Figures 2.11d and 2.11e). At LLDPE volume fractions of 0.69 and 0.76, the layered structure of pores is mostly lost (Figures 2.11f and 2.11g). In this composition regime, the majority of pyrene crystallizes at the same temperature as LLDPE (Figures 2.8a and 2.8c). Pores become so small that they can hardly be seen at the micrometer scale, and the morphology reflects the precipitation pattern of the pyrene crystals visualized in optical microscopy experiments (Figures 2.9f and 2.9h).

Porous structures from mixtures of LLDPE and HMB are very different from those of pyrene/LLDPE mixtures as shown in Figure 2.12. HMB produces plate-like pores much larger in size than those of pyrene at similar LLDPE volume fractions. The local direction of HMB crystal growth is less aligned. Porous structures directed by HMB crystallization are observed when the LLDPE volume fraction is below 0.67 (Figures 2.12a through 2.12g). HMB crystallizes before LLDPE upon cooling in these samples as confirmed by DSC experiments (Figures 2.8b and 2.8d). With a volume fraction of LLDPE of 0.77 (close to eutectic composition), plate-like porous structures are no longer seen. HMB and LLDPE crystallize at the same temperature in these samples as observed by DSC (Figures 2.8b and 2.8d). The morphology as observed by SEM indicates that the microporous structure can be controlled by the identity of the crystallizable diluents as well as the composition of the mixtures under fixed cooling conditions.

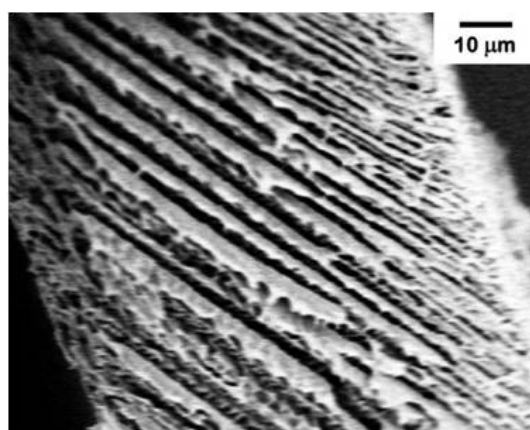
#### 2.4.4. Effect of Cooling Conditions

In addition to the nature of the mixtures (identity of the diluents and composition of the mixture), morphology strongly depends on the cooling conditions as can be inferred from the discussion in the previous sections. Figure 2.13 shows that different morphologies can be obtained from the same mixture (pyrene/LLDPE, 3/1) by changing cooling conditions. If the mixture is cooled from its liquid state at a relatively slow cooling rate ( $\sim 5\text{ }^{\circ}\text{C}/\text{min}$ ), supercooling is not significant and pyrene develops large crystals under these cooling conditions (Figure 2.13a). If the mixture is quenched from  $200\text{ }^{\circ}\text{C}$  to  $0\text{ }^{\circ}\text{C}$  using ice water bath, supercooling is significant and pyrene crystallization is characterized by strong directional growth which is a result of dendritic growth (Figure 2.13b). If the molten liquid mixture is quenched using liquid nitrogen ( $-196\text{ }^{\circ}\text{C}$ ), there is not enough time for pyrene crystals to grow and the resulting morphology shows relatively small crystals of pyrene, which are seen as pores in Figure 2.13c after the extraction of pyrene crystals.

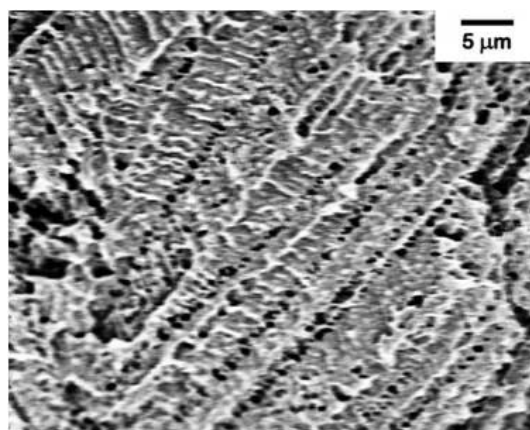
If the solidification of the mixture proceeds under non-uniform cooling, the corresponding morphology shows a mixed structure. Figure 2.14 shows that when the solidifying mixture is in contact with different temperatures at each side (the upper side is maintained at  $35\text{ }^{\circ}\text{C}$  and the lower side is maintained at  $100\text{ }^{\circ}\text{C}$  during solidification), the resulting morphology shows gradually changing structure. A higher cooling temperature ( $100\text{ }^{\circ}\text{C}$ ) leads to larger, less-aligned pores while a lower cooling temperature ( $35\text{ }^{\circ}\text{C}$ ) imposes large supercooling that leads to smaller, better aligned pores, each type of which exists in one sample (Figure 2.14).



(a)



(b)



(c)

**Figure 2.13.** Morphology of fractured cross-sections of pyrene/LLDPE (3/1) mixtures prepared at different cooling conditions. SEM micrographs were taken after the extraction of pyrene. (a) relatively slow cooling rate of 5 °C/min, (b) quenched with ice water at 0 °C, (c) quenched with liquid nitrogen at -196 °C.

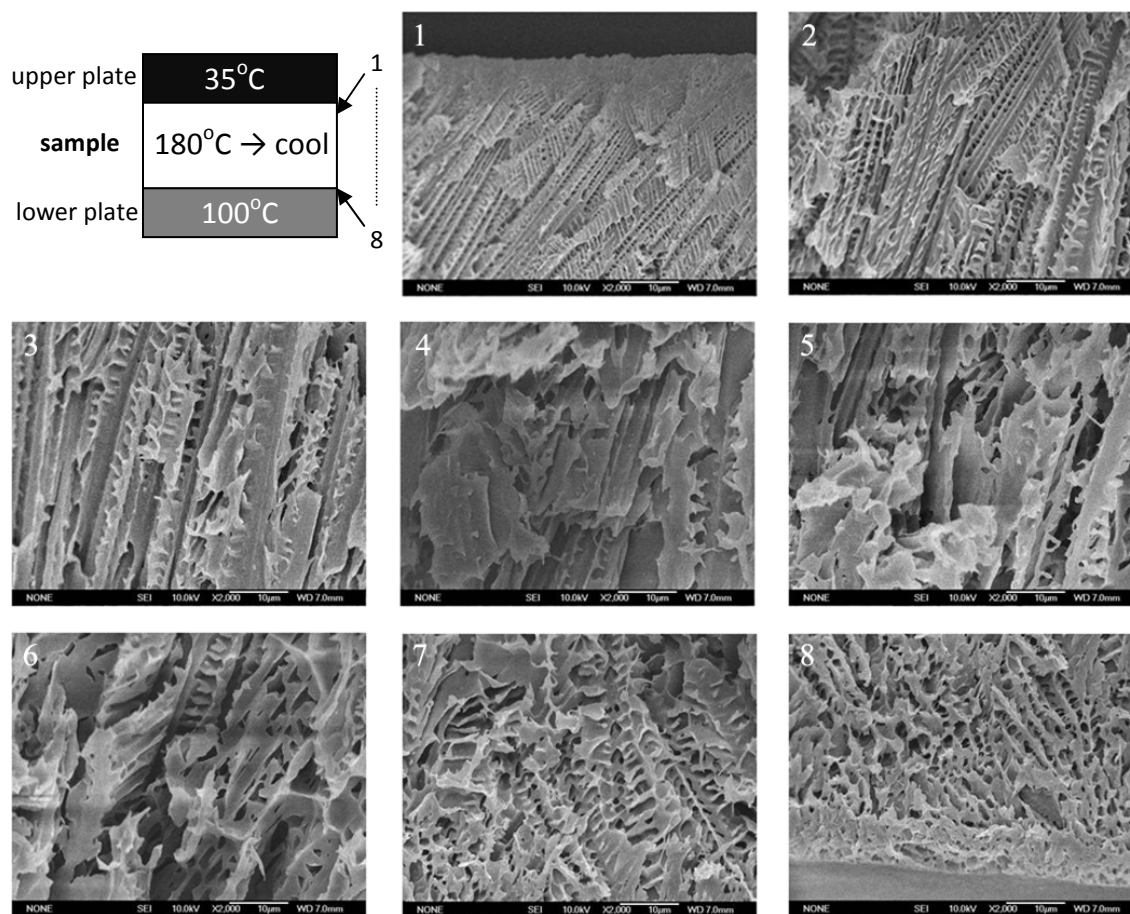


**Figure 2.14.** Gradually changing morphology of fractured cross-sections of pyrene/LLDPE (3/1) mixtures prepared under non-uniform cooling temperature. SEM micrographs were taken after the extraction of pyrene.

#### **2.4.5. Effect of the Polymer**

Locally anisotropic structure is developed primarily by the crystallization of the diluents and the effect of polymer on the final structure is negligible. However, the molecular weight of the polymer (hence, the viscosity of the mixture) may affect the crystallization of the diluents and subsequently affect the final morphology. Figure 2.15a shows that the dendritic growth of pyrene crystals is hindered when the viscosity of the mixture is high due to the high molecular weight of the polyethylene. In contrast, well aligned pores, smaller in size, are seen when low molecular weight polyethylene is used (Figure 2.15b).

#### **2.5. Conclusions**

Locally anisotropic porous materials have been prepared using high melting temperature diluents and a semi-crystalline polymer. Diluents were selected that form homogeneous mixtures with the polymer at elevated temperature, but undergo phase separation upon cooling. Since the crystallization temperatures of the selected diluents are higher than that of the polymer, phase separation is triggered by the crystallization of the diluent in the polymer solution, providing that there is a sufficient amount of diluent in the mixture. The crystallization of diluent continues until eutectic solidification begins, after which the structure is fixed. Porous materials are obtained by extracting the diluent crystals from the solidified samples. Phase separation can also be triggered by the crystallization of the polymer if the initial composition of the mixture is

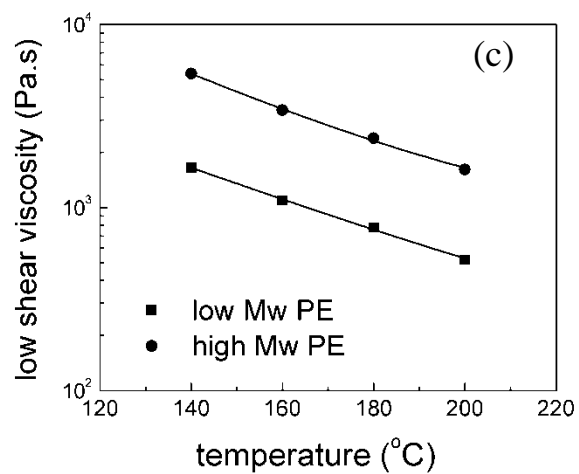
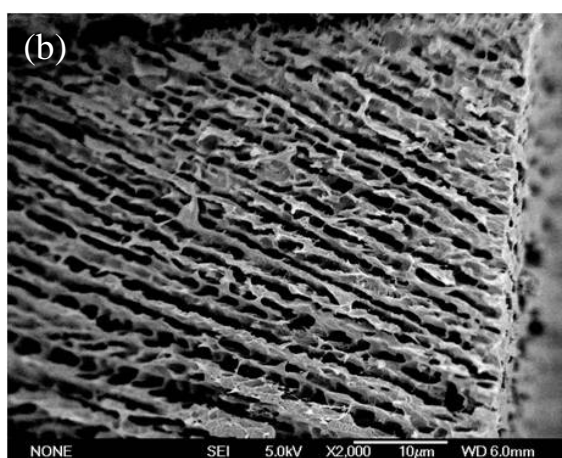
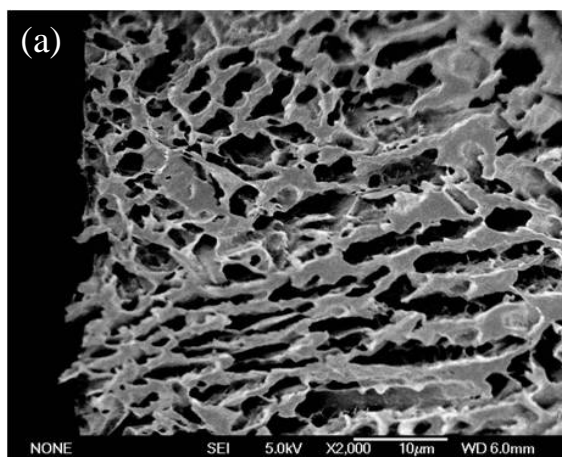


**Figure 2.15.** Effect of the viscosity of the polymer. (a) pyrene / high Mw HDPE (3/1), (b) pyrene / low Mw HDPE (3/1), (c) steady state viscosity (at the shear rate of  $0.01 \text{ s}^{-1}$ ) of neat HDPE. SEM micrographs were taken after the extraction of pyrene.

highly polymer-rich (higher than the eutectic composition). In this case, samples do not show visible porous structures at the micrometer scale. Since the porous structures obtained from diluent-rich samples are determined by the crystal growth characteristics of the diluent, the final shape and size of the pores depend strongly on the types of diluent as well as the composition of the mixtures. Hexamethylbenzene (HMB) forms relatively large, plate-like pores while pyrene produces relatively small, better aligned layers of pores. Crystallization of pyrene requires much greater supercooling than that of HMB, leading to dendritic solidification which is characterized by a morphology resulting from the formation of slender spikes in specific crystallographic directions with regular branches in other equivalent directions. HMB, on the other hand, crystallizes at small supercooling and does not develop any noticeable dendritic structure. It is also shown that different cooling conditions lead to different morphologies. Slow cooling leads to large, less-aligned porous structures while fast cooling leads to small, better-aligned porous structures. The molecular weight of the polymer may affect the final morphology since the crystal growth of the diluents is affected by the viscosity of the polymer medium. All of these results demonstrate that the microstructure of porous polymeric materials can be controlled by the choice of the high melting diluents, composition of the polymer solutions and the cooling conditions.

## CHAPTER 3

### SELF-REINFORCING ISOTACTIC POLYPROPYLENE PREPARED USING CRYSTALLIZABLE SOLVENTS

A new approach to reinforce and toughen isotactic polypropylene (iPP) with improved processability is evaluated. The concept involves using a crystallizable solvent that is molten at process temperatures and miscible with the polymer thereby reducing its process viscosity. As the polymer cools, the solvent undergoes thermally induced phase separation (TIPS) to produce crystallites that increase the modulus of the solid through reinforcement, and promote an increase in impact resistance by mechanisms similar to rubber-toughened materials. Tetrabromobisphenol-A (TBBPA) is introduced to iPP which forms a homogeneous mixture at elevated temperature and acts as a processing aid, but undergoes phase separation and subsequent crystallization upon cooling to form rigid particles which, in turn, acts as a toughening agent at room temperature. A phase diagram constructed using Flory-Huggins solution thermodynamics shows good agreement with the experimental results. The steady state shear viscosity decreases as TBBPA content increases for mixtures in melt state, indicating improved processability. The decrease in viscosity significantly enhances the crystallization rate of iPP, most likely due to increased diffusivity. The structure of the iPP crystals is unchanged. Tensile tests show that as TBBPA content increases (up to 15 wt.%), the yield stress decreases while elongation at break increases.

#### 3.1. Introduction

Toughening mechanisms in semi-crystalline polymers have been studied extensively, both experimentally and theoretically, in the last few decades.<sup>43-44</sup> Among

the many strategies to increase toughness, introducing soft rubber particles has proven most successful, despite the concurrent decrease in stiffness.<sup>45</sup> Many studies have shown how rubber particle size and concentration affect the increase in measured toughness. The general conclusion from these studies is that the rubber concentration should be greater than a critical value, which is a function of the particle size. Several mechanisms have been suggested to explain the toughening effect of rubbers such as multiple-crazing, damage competition, shear-yielding, microvoiding and cavitation. However, it is generally accepted that rubber cavitation followed by either matrix shear-yielding (pseudo-ductile polymers) or crazing (brittle polymers) are major toughening mechanisms.

If cavitation occurs well before the bulk matrix failure, plastic deformation around and between particles is facilitated and the fracture event is delocalized. While cavitation depends on the size of the rubber particles (larger particles cavitate before smaller ones),<sup>46-47</sup> matrix yielding and subsequent plastic flow depend on the particle concentration. Wu<sup>6</sup> combined two interdependent parameters, rubber particle size and concentration, in a single parameter, the inter-particle distance. According to his argument, toughening is primarily originated by the preferential orientation of crystal planes which provides the lowest shear resistance between rubber particles. If the surface-to-surface inter-particle distance is less than the critical ligament thickness, the preferentially oriented layers percolate throughout the structure and reduce plastic resistance, leading to plastic deformation. If not, the overall matrix plastic resistance is substantially elevated and this prevents plastic deformation and leads to premature brittle fracture which is governed by extrinsic flaws. The other requirement for this

mechanism is that the particles cavitate in the early stages of deformation to allow for unhindered stretching of the ligaments.

In contrast, rigid particles have been used primarily to improve composite stiffness and strength. Unfortunately, a notable decrease in fracture toughness is also normally caused by the addition of rigid particles. This occurs because the rigid particles are introduced at much higher volume fractions compared to soft particles and treatments are done to the particles to promote high levels of adhesion. This combination results in a high composite modulus and strength since the particles become load bearing constituents. However, once the particles fail, severe strain localization occurs in the matrix under the highly multiaxially constrained conditions and the matrix fails locally by brittle fracture rather than shear flow. The net consequence of this process usually results in a reduction of material ductility and energy absorption during fracture.

However, Argon and coworkers<sup>48-49</sup> reported that toughness and stiffness can be increased simultaneously by the incorporation of rigid fillers under certain conditions: First, the concentration of rigid fillers should be close to that of conventional rubber toughened systems, which is usually lower than that used to optimize strength and stiffness. Second, the inter-particle distance must be below a threshold value (critical ligament thickness). Third, there must be low to moderate levels of adhesion between the polymer matrix and the particles. Argon surmised that under these conditions, the rigid particles provide some modulus enhancement at lower stress levels in contrast to conventional soft particle-toughened systems. As the stress level in the material is increased, particle-matrix debonding can occur relieving multiaxial stresses in the

matrix and dissipating energy much like cavitation in soft particle toughened systems. Based on their experimental results for semi-crystalline polymers (Nylon, HDPE and iPP) mixed with either soft particles or rigid particles, Argon and coworkers concluded that the source of the toughness is the plastic extensibility of the matrix material in the inter-particle ligament and that the mechanical properties of the filler particles are of little importance.<sup>48-53</sup> However, it should be noted that another major drawback of this toughening approach is the detrimental effects that the filler particles have on the polymer processability. The incorporation of either soft particles or rigid particles into a polymer inevitably causes the melt viscosity to increase significantly.

In this chapter, a new approach to reinforce and toughen polymers is described. It involves using a crystallizable solvent as a single additive to produce a composite material with improved processability, toughness and stiffness. The additive is part of a homogeneous polymer solution at process temperatures and functions as a processing aid (i.e. plasticizer), but the solution undergoes phase separation and subsequent crystallization upon cooling to form an appropriate morphology (i.e. a dispersion of crystallites) for enhanced toughness and stiffness. This chapter reports initial attempts of this strategy as it is applied to iPP.<sup>54-55</sup>

## **3.2. Materials and Sample Preparation**

### **3.2.1. Materials**

Tetrabromobisphenol-A (TBBPA) was provided by Grace Chemical and used without further purification. Low molecular weight, high flow isotactic polypropylene

(iPP) was provided by Exxon Mobil and used as received. The molar mass of iPP was determined by gel permeation chromatography (GPC, PL-GPC 220) at 145 °C using trichlorobenzene as a solvent. Thermal properties were determined by differential scanning calorimetry (DSC-2910, TA instruments) at 10 °C/min heating and cooling rates. Thermal stability of TBBPA was evaluated by thermogravimetric analysis (TGA-2950, TA instruments) at 10 °C/min heating rate (Figure 3.1). Other properties were obtained from the literature and are listed in Table 3.1.

**Table 3.1.** Materials properties

Properties	Unit	iPP	TBBPA
Molar Mass	g / mol	49,000 (Mn) 354,000 (Mw)	544
Degree of Polymerization	-	1164	N/A
Molar Volume	cm <sup>3</sup> / mol	48.06 <sup>a</sup> (propylene unit)	257
Density	g / cm <sup>3</sup>	0.905	2.12
Heat of Fusion	J / mol	3,900 (propylene unit)	32,600
Melting Temperature	K (°C)	439 (166)	460 (187)
Crystallization Temperature	K (°C)	382 (109)	N/A
Solubility Parameter	MPa <sup>1/2</sup>	17.2 <sup>a</sup>	20.2 <sup>b</sup>

<sup>a</sup> Typical value from references,<sup>33, 56</sup>

<sup>b</sup> Estimated value from reference.<sup>57</sup>

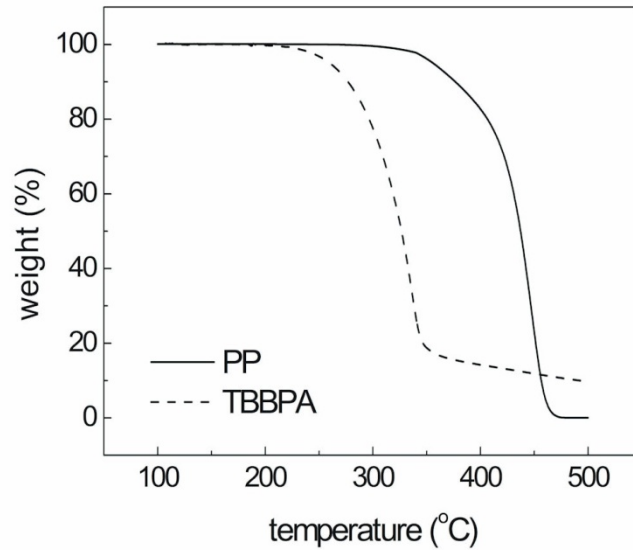


**Figure 3.1.** TGA thermogram for iPP and TBBPA measured at a 10 °C/min heating rate.

### 3.2.2. Sample Preparation

Blends of iPP with TBBPA ranging in volume fractions from 0 to 0.2 of TBBPA were prepared by pre-mixing iPP pellets with TBBPA powders in desired proportions followed by melt blending using a single screw extruder (Brabender , 25:1 L/D ¾” Independent Extruder) at temperatures of 200 - 220 °C. The extrudate was quenched using a cooling water bath and subsequently dried at 80 °C overnight. Dried samples were chopped and molded with compression molding machines. One of the compression molding machines was maintained at 220 °C for melting and the other one was maintained at 40 °C for cooling; both machines were operated at about 10 MPa. Tensile test specimens were cut from 1 mm thick plaques and fracture toughness test samples were cut from 6 mm thick plaques. Dog bone-shaped tensile specimens were prepared according to ASTM D638-02a, type V specification. Fracture toughness test

bars ( $76 \times 12 \times 6$  mm) were prepared according to ASTM D5045-99. Notches were made using a disc-saw (about 3 mm deep) followed by a sharp razor blade cut (about 2 mm deep) under liquid nitrogen.

### **3.3. Characterization and Testing**

#### **3.3.1. Thermal Analysis**

Differential scanning calorimetry (DSC-2910, TA instruments) was used to measure the melting temperatures and crystallization temperatures of the samples. Each sample was sealed in a hermetic aluminum DSC pan, heated from 25 °C to 200 °C at 10 °C/min and held at 200 °C for 3 minutes, and then cooled to 25 °C at 10 °C/min to measure crystallization temperature. This procedure was repeated to determine melting temperature (reheating peak). The peak maxima were taken as melting and crystallization temperatures. Crystallization kinetics was also investigated by DSC. Each sample was heated to 200 °C at 10 °C/min and held at 200 °C for complete melting, followed by fast quenching to three different temperatures (123 °C, 120 °C, 117 °C). Heat flow as a function of time was recorded during crystallization at constant temperature. The results were analyzed using the Avrami equation.

Glass transition temperatures ( $T_g$ ) were measured by dynamic mechanical analysis (DMA-2980, TA instruments) which was performed using testing bars ( $25 \times 10 \times 3$  mm) in the 3-point bending mode at 1 Hz as temperature was increased from -150 °C to 100 °C at 3 °C/min. The storage modulus and loss factor ( $\tan \delta$ ) were measured as a function of temperature and  $T_g$  was determined as the peak value of  $\tan \delta$ .

### **3.3.2. Mechanical Characterization**

Tensile properties of the samples were studied at room temperature using an Instron 4200 machine. The tests were performed according to ASTM D 638-02a using type V specimens at 10 mm/min cross-head speed. Fracture toughness properties were studied at room temperature according to ASTM D 5045-96 using single-edge notched bend (SENB) specimens at 50 mm/min cross-head speed. All samples were conditioned at room temperature overnight before testing. At least five specimens were tested and results are reported as averages.

### **3.3.3. X-ray Scattering**

Crystal structure was examined by wide-angle X-ray scattering (WAXS, Molecular Methology M2, Cu K $\alpha$  radiation) using 1 mm thick plaque specimens.

### **3.3.4. Optical Microscopy**

The phase separation process was observed using an optical microscope (Olympus BX51) equipped with a hot stage (Linkam TMS-93) and a temperature controller (Linkam THMS-600). Each sample was placed between a pair of microscope slides and heated from 25 °C to 200 °C at 10 °C/min, held at 200 °C for 1 minute, and then cooled to 25 °C at 10 °C/min. Dispersion of TBBPA particles was observed by both optical microscopy and confocal microscopy (Leica TCS SP2). A sample was obtained from a four-point bend double crack specimen as suggested by Sue et al.<sup>58</sup> A core portion of the incomplete crack was cut and cryo-microtomed (Leica Ultracut) at -120 °C so that the dispersion of the particles and the morphology along the crack propagation path could be analyzed.

### **3.3.5. Scanning Electron Microscopy (SEM)**

The morphology of each sample was examined by field-emission scanning electron microscopy (JEOL FX-6210) using an accelerating voltage of 5 – 10 kV. Undeformed samples were prepared by splitting 1 mm thick plaque specimens under liquid nitrogen on top of a sharp razor blade to examine the morphology and visualize the TBBPA particles. Cryo-cutting the tensile specimens subsequent to the tension test along the direction of deformation was carried out to investigate the morphology around TBBPA particles under tension. The fractured surfaces were investigated using broken pieces of SENB specimens that had been subjected to three point bending testing. The exposed cross-section was coated with Au using a sputter coating machine (Cressington Sputter Coater 108). Four-point bend double crack specimens were also investigated with SEM.

### **3.3.6. Viscometry**

The steady state shear viscosity of the samples was measured using a parallel plate rheometer (AR-2000, TA instruments) at 180 °C and 200 °C. Each sample was placed between the parallel disc plates (gap: 0.8 mm) and heated until the temperature was equilibrated at the target value. Once thermal equilibrium was reached, shear viscosity was measured at constant temperature as a function of shear rate ( $0.001 \text{ s}^{-1}$  –  $1 \text{ s}^{-1}$ ). Since the shear viscosity decreased slightly as shear rate increased, the viscosity at a shear rate of  $0.01 \text{ s}^{-1}$  was chosen as the low shear viscosity to evaluate the processability.

### 3.4. Results and Discussion

#### 3.4.1. Thermally Induced Phase Separation (TIPS)

The phase separation process of mixtures of iPP and TBBPA that occurs during cooling was investigated by optical microscopy (Figure 3.2). Equilibrium phase diagram was calculated based on Flory-Huggins solution thermodynamics<sup>3</sup> and shows good agreement with results obtained from DSC as shown in Figure 3.3. The theoretical melting temperature of iPP (crystalline iPP in equilibrium with polymer solution) can be calculated using equation 1.10 in Chapter 1.

$$\frac{1}{T_m} = \left[ 1 + \frac{R\beta}{\Delta H_u} \left( \frac{V_u}{V_1} \right) (1 - \phi_2)^2 \right]^{-1} \left[ \frac{1}{T_m^0} + \frac{R}{\Delta H_u} \left( \frac{V_u}{V_1} \right) \left\{ \left( 1 - \frac{1}{N} \right) (1 - \phi_2) - \frac{\ln(\phi_2)}{N} \right\} \right] \quad (1.10)$$

where  $T_m$  is the melting temperature of iPP in a polymer solution,  $T_m^0$  is the melting temperature of neat iPP,  $\Delta H_u$  is the enthalpy of fusion per repeat unit of iPP,  $N$  is degree of polymerization,  $\phi_2$  is the volume fraction of iPP,  $R$  is the gas constant and  $\beta$  is a constant which is calculated from the solubility parameters of iPP ( $\delta_2$ ) and TBBPA ( $\delta_1$ ) along with the molar volume of TBBPA ( $V_1$ ), using the equation  $(\delta_1 - \delta_2)^2 V_1 / R$ . Five propylene units are considered as a repeat unit so that the molar volume of iPP repeat unit ( $V_u$ ) and that of TBBPA ( $V_1$ ) are similar to each other, as is assumed in Flory-Huggins theory. Similarly, the melting temperature of TBBPA at which the crystalline TBBPA is in equilibrium with the polymer solution can be calculated using equation 1.14 in Chapter 1.

$$\frac{1}{T_{m,1}} = \left[ 1 + \frac{R\beta\phi_2^2}{\Delta H_1} \right]^{-1} \left[ \frac{1}{T_{m,1}^0} - \frac{R}{\Delta H_1} \left\{ \left( 1 - \frac{1}{N} \right) \phi_2 + \ln(1 - \phi_2) \right\} \right] \quad (1.14)$$

where  $T_{m,1}$  is the melting temperature of crystalline TBBPA in a polymer solution,  $T_{m,1}^0$  is the melting temperature of neat TBBPA and  $\Delta H_1$  is the enthalpy of fusion for neat TBBPA. According to the calculation, liquid-liquid de-mixing is expected to occur only when the volume fraction of iPP is less than 0.2. Within the composition range of interest, in which the volume fraction of iPP is greater than 0.8, phase separation is expected to occur by the solidification of either TBBPA or iPP, provided the thermal transition is slow enough to maintain thermodynamic equilibrium.

iPP mixed with 10 vol.% of TBBPA at 200 °C forms a homogeneous mixture as shown in Figure 3.2a. This mixture undergoes phase separation upon cooling and a TBBPA-rich droplet phase begins to grow in the iPP-rich matrix phase when the temperature reaches about 160 °C (Figure 3.2b). The droplets continue to grow until the entire sample solidifies (~140 °C) (Figure 3.2c). As the temperature decreases, the mixture becomes more turbid due to a decrease in miscibility. Similar behavior was observed for a polymer solution containing 20 vol.% of TBBPA. In this case, phase separation initiates when the temperature reaches about 170 °C (Figure 3.2e), which is higher than that for 10 vol.% TBBPA mixture, and the droplets grow until the temperature reaches about 140 °C (Figure 3.2f). Due to the higher concentration of TBBPA and the longer droplet growth period, the mixture containing 20 vol.% of TBBPA develops larger droplets than 10 vol.% TBBPA samples. These observations indicate that the size of TBBPA particles strongly depends on the composition of the mixture under the same thermal processing conditions.

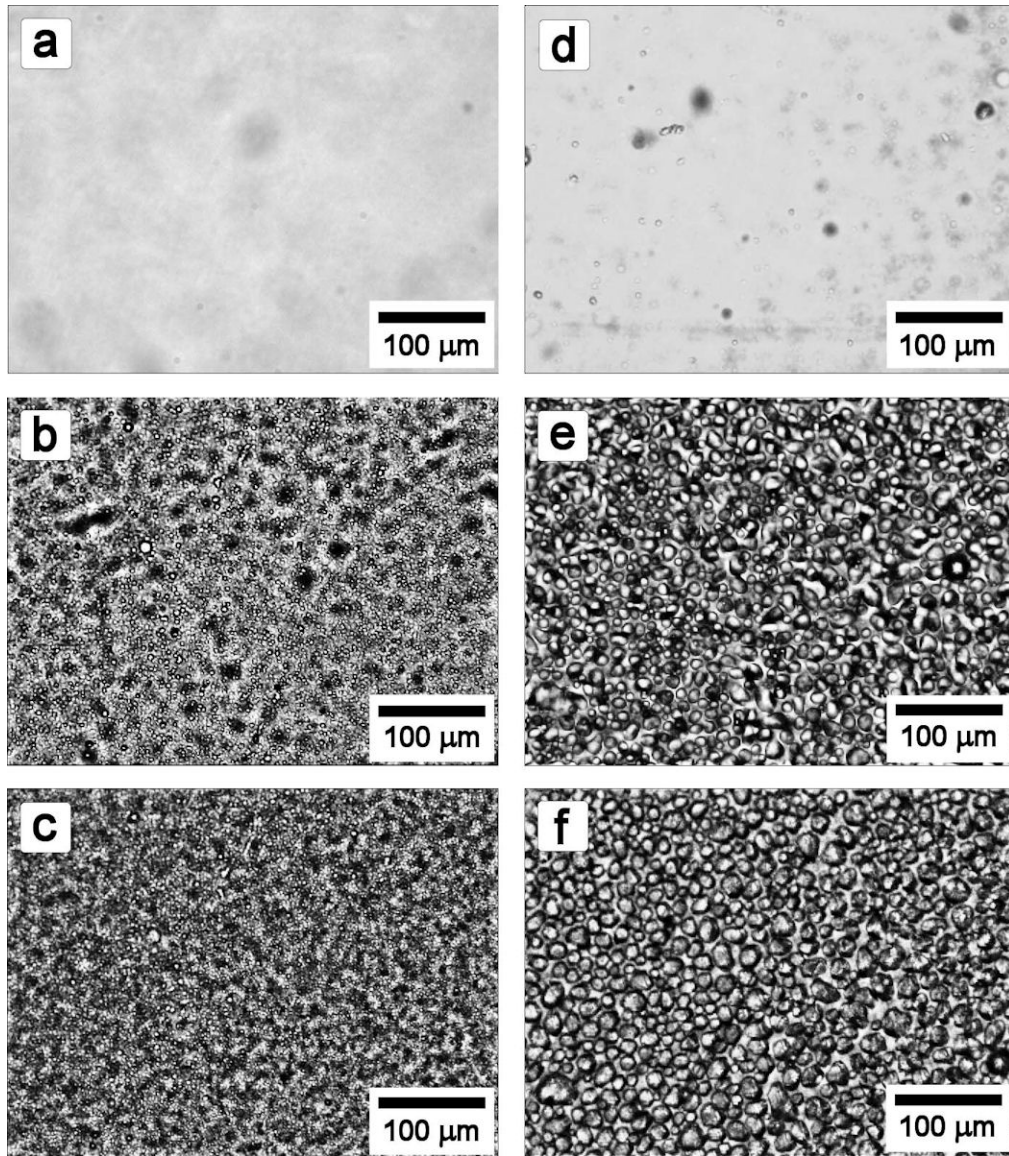


**Figure 3.2.** Photomicrographs taken by 45° polarized optical microscopy while mixtures of TBBPA and iPP were cooled from 200 °C at 10 °C/min. (a) iPP/TBBPA=9/1(v/v) at 200 °C, (b) iPP/TBBPA=9/1(v/v) at 160 °C, (c) iPP/TBBPA=9/1(v/v) at 140 °C, (d) iPP/TBBPA=8/2 (v/v) at 200 °C, (e) iPP/TBBPA=8/2(v/v) at 170 °C, (f) iPP/TBBPA=8/2(v/v) at 140 °C.

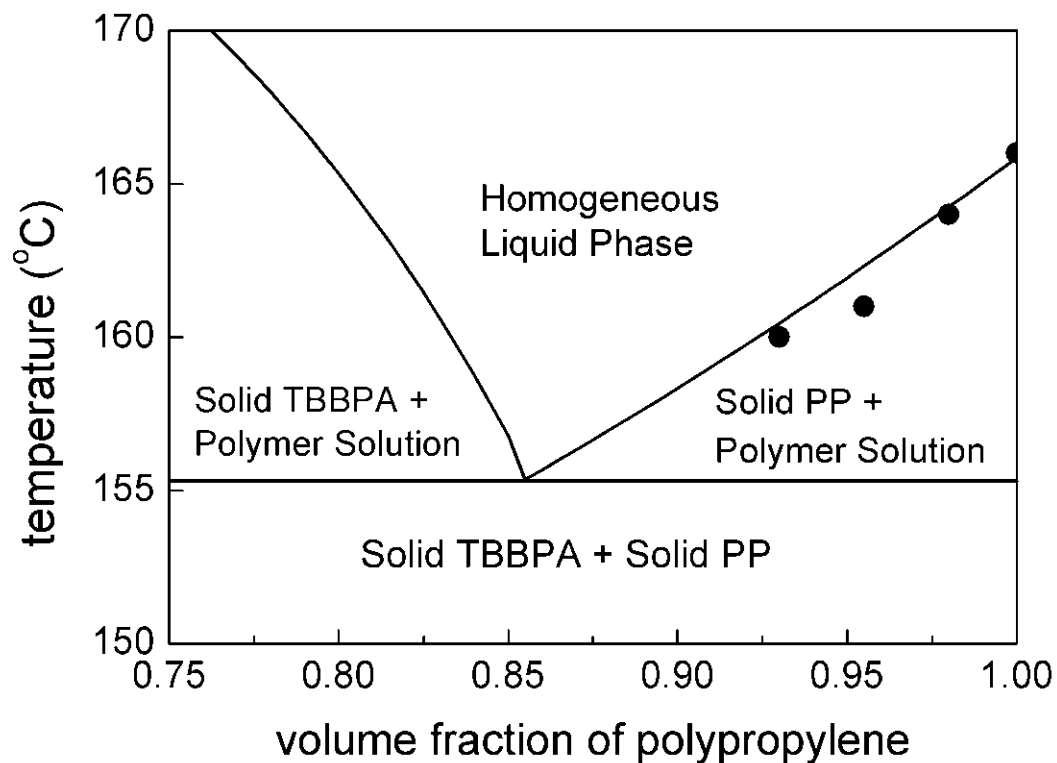


**Figure 3.3.** Equilibrium phase diagram for a mixture of TBBPA and iPP (Liquidus lines are calculated results and circles are melting temperatures measured by DSC at a 10 °C/min heating rate).

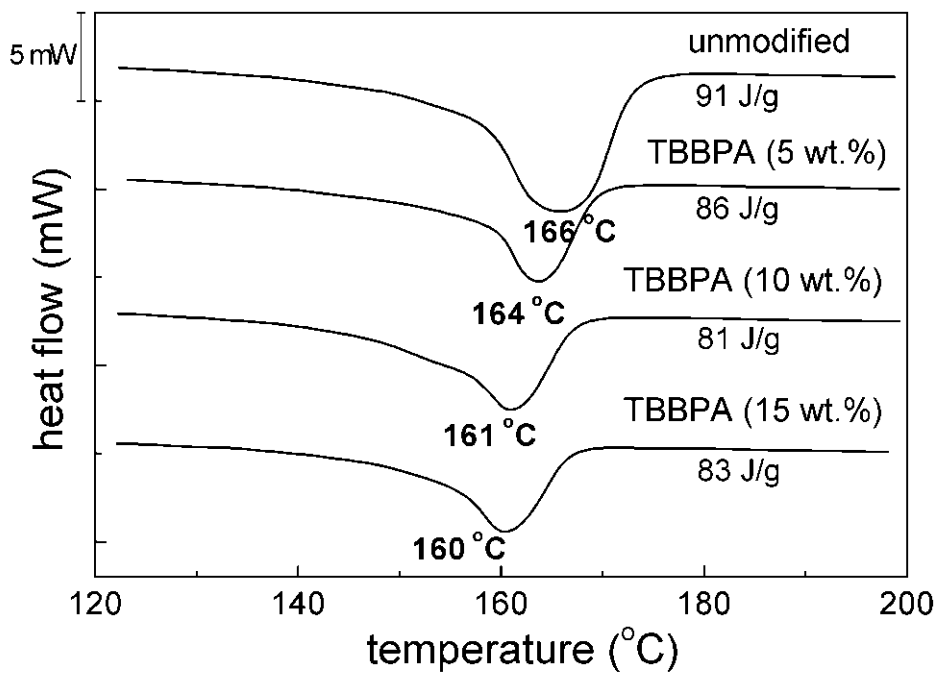


**Figure 3.4.** DSC thermograms of selected samples for melting temperature determination (Reheating run at 10 °C/min).

While a melting temperature depression is observed, which is expected for miscible mixtures, the glass transition temperature ( $T_g$ ) of iPP increases slightly as TBBPA content increases (Figure 3.5). If TBBPA crystals acted as a plasticizer, the  $T_g$  would be decreased. This is not the case. This indicates that TBBPA crystals do not enhance the mobility of iPP molecules. The increase in  $T_g$  could be due to a decrease in free volume of iPP in the presence of TBBPA crystals, but this is an interpretation with no independent confirmation.

### **3.4.2. Crystallization**

Crystallization of mixtures with different composition was studied using DSC, optical microscopy and wide-angle X-ray scattering (WAXS). Figure 3.6 shows DSC thermograms obtained by cooling each sample from 200 °C at 10 °C/min. With the addition of TBBPA, the width of the exothermic peak (due to crystallization) becomes much narrower and the crystallization temperature increases slightly. The crystallization temperature, however, is almost independent of TBBPA concentration in the range between 5 and 15 wt.%. This implies that the crystallization rate of iPP increases significantly with the addition of TBBPA, but also that this effect is saturated at 5 wt.% loading of TBBPA.

Spherulites of iPP were observed using cross-polarized optical microscopy. Figure 3.7 shows that the spherulites of iPP become smaller in size and more uniform in size distribution with the addition of TBBPA. This indicates that the diffusion of iPP molecules to the crystal growing sites becomes significantly enhanced due to the molten TBBPA which acts like a processing aid. It is also possible that TBBPA acts as a nucleating agent to enhance crystallization of iPP, but it seems less likely in this case

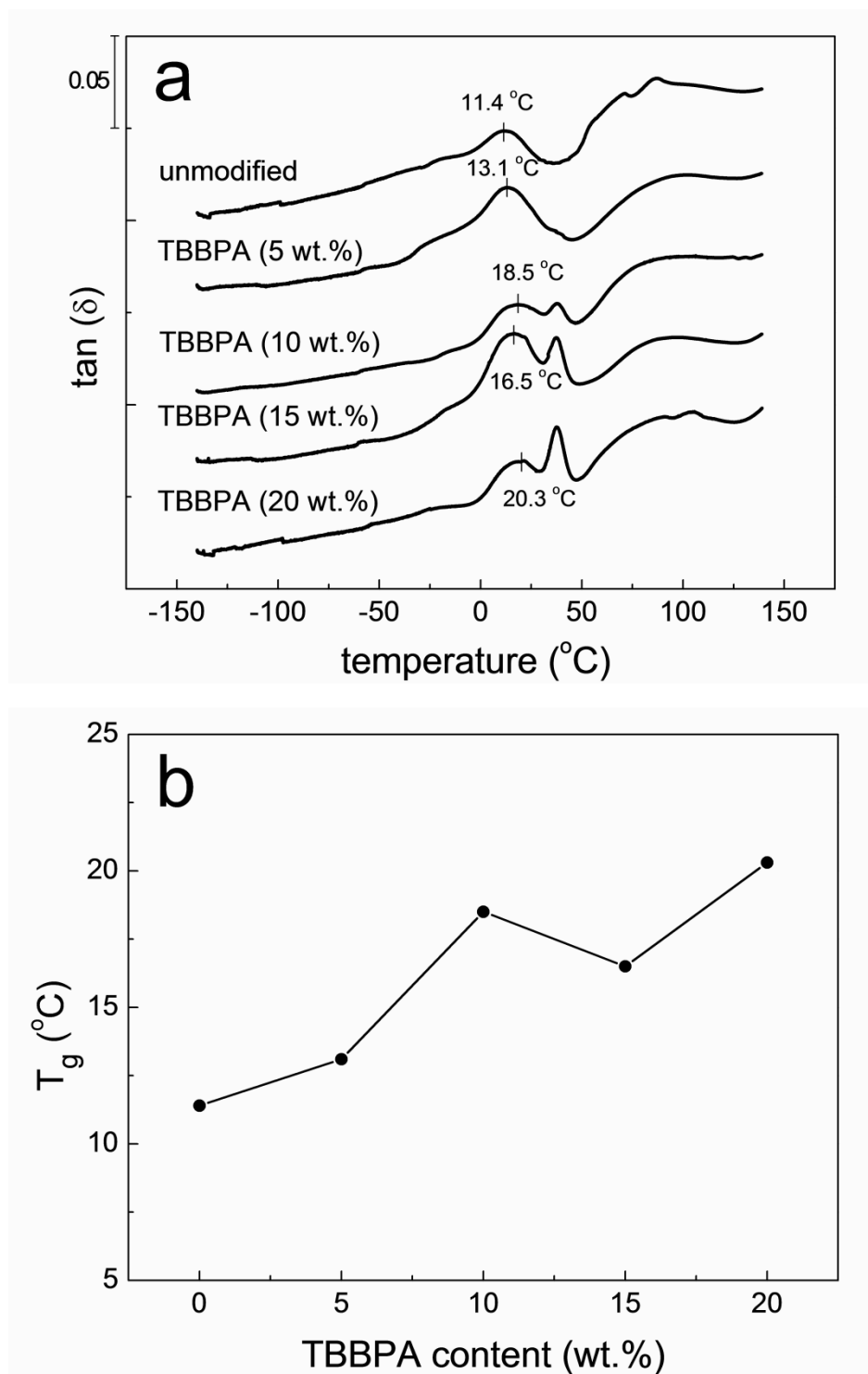


**Figure 3.5.** Dynamic mechanical analysis result measured at 1 Hz, 3 °C/min heating rate. (a) loss factor ( $\tan \delta$ ) versus temperature, (b)  $T_g$  versus TBBPA content.

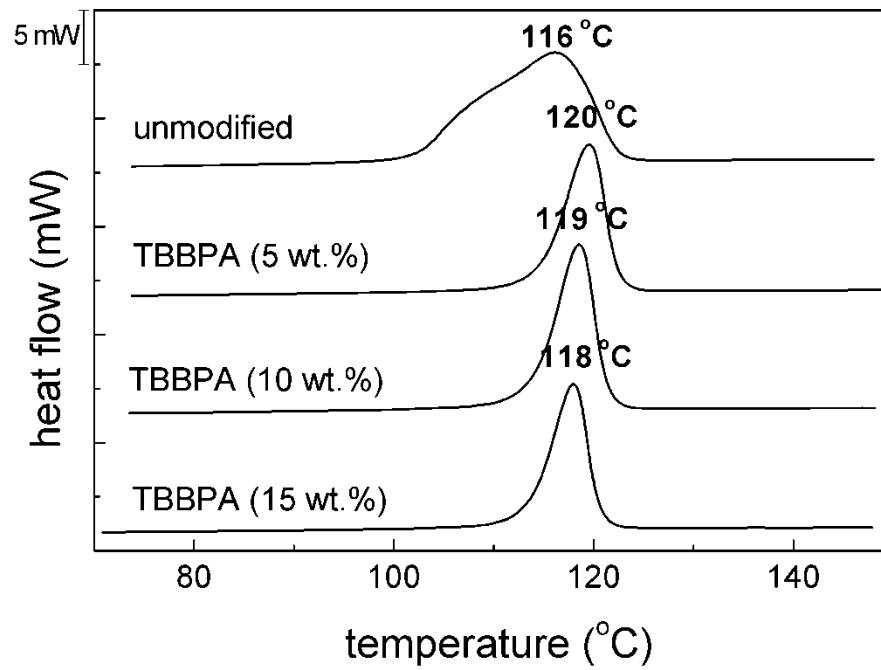


**Figure 3.6.** DSC thermograms of selected iPP/TBBPA mixtures obtained by cooling runs from 200 °C at 10 °C/min.

since the increase of crystallization temperature is not as high as expected from nucleating agents and the spherulite size does not decrease as much as would be expected. However, the small change in size of the iPP spherulites affects the endothermic melting process as shown in Figure 3.4, which shows melting temperature depression due to the decreased size of iPP spherulites in the presence of TBBPA.

Although TBBPA affects the rate of crystallization noticeably, it does not affect the crystal structure of iPP. WAXS results for neat iPP show that iPP crystals are mostly in the  $\alpha$ -form. The peak positions in WAXS do not change in the presence of TBBPA, indicating that the crystal structure of iPP does not change (Figure 3.8). The absence of a significant change in melting temperature excludes the possibility of producing  $\beta$ -form crystals of iPP, whose typical melting temperature is about 150 °C.<sup>59</sup>

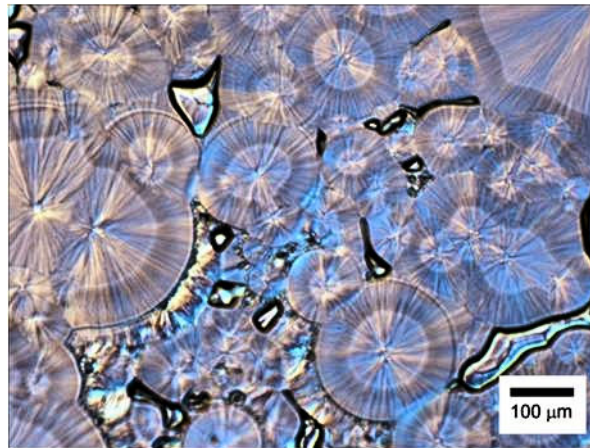
Isothermal crystallization kinetics were investigated using DSC by heating the sample to 200 °C to eliminate all of the crystals, followed by quenching to fixed temperatures (117 °C, 120 °C and 123 °C) and measuring heat flow as a function of time. Relative crystallinity was determined which is defined as

$$X_t = \frac{\int_0^t (dH(t) / dt) dt}{\int_0^\infty (dH(t) / dt) dt} \quad (3.1)$$

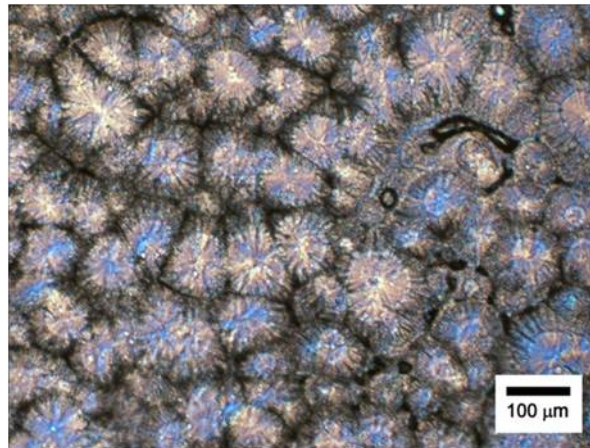
where  $dH(t)/dt$  is the heat evolution rate during the crystallization.  $X_t$  in equation 3.1 represents the volume fraction of the crystalline portion of the sample. The Avrami equation can be expressed using  $X_t$  as

$$1 - X_t = e^{-Kt^n} \quad (3.2)$$

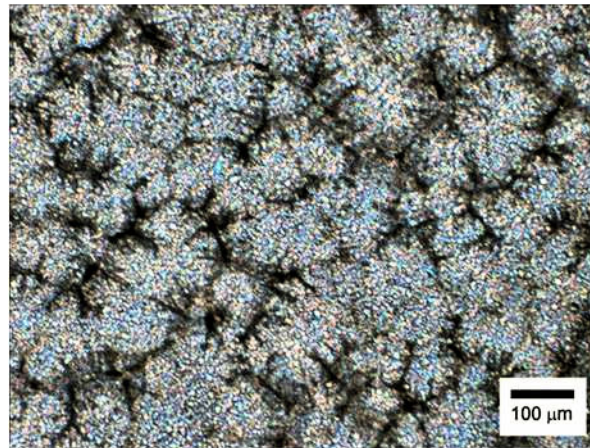
where  $n$  is a constant which depends on the mode of crystallization and  $K$  is a rate constant which depends on the temperature as well as nucleation modes.



(a)



(b)



(c)

**Figure 3.7.** Micrographs of iPP spherulites taken by cross-polarized optical microscopy at room temperature. (a) neat iPP, (b) 10 wt.% TBBPA/iPP, (c) 20 wt.% TBBPA/iPP.

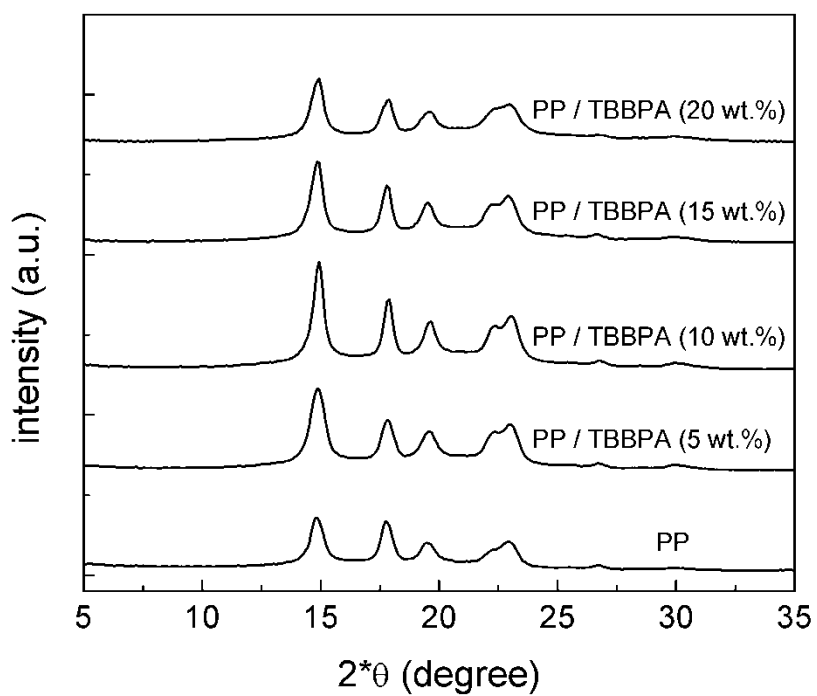
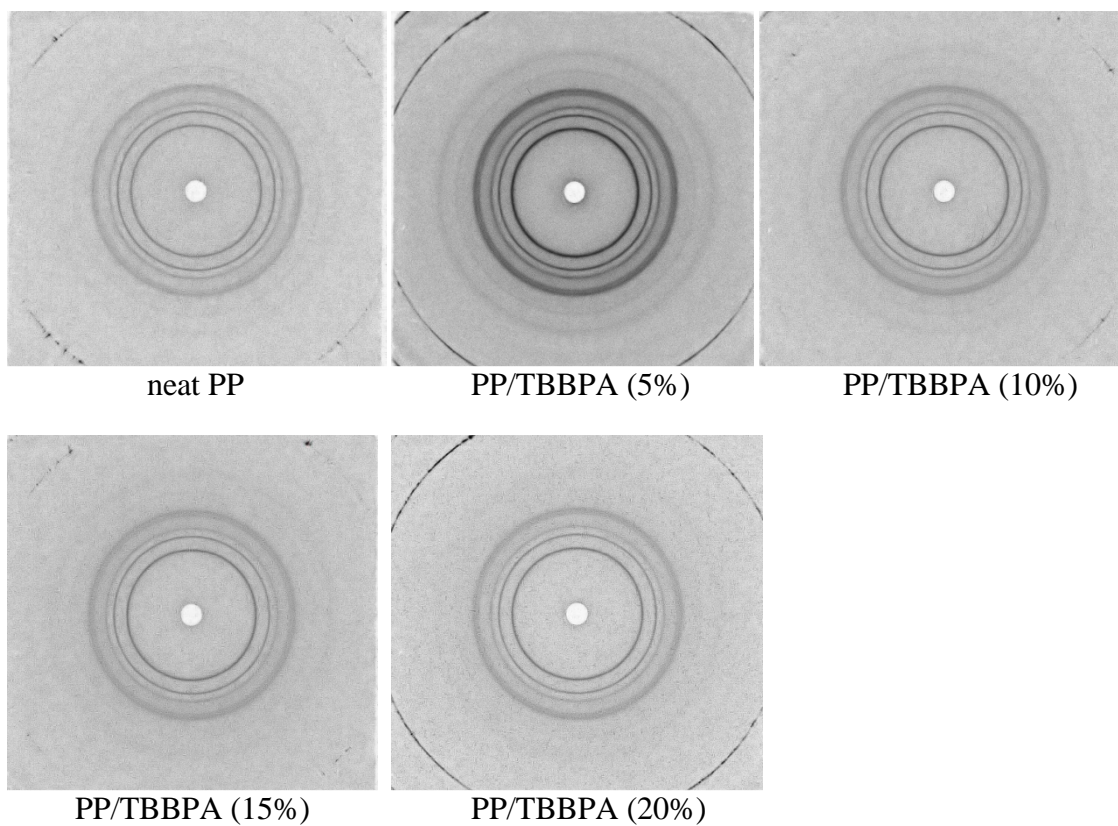


**Figure 3.8.** Wide-angle X-ray scattering results for mixtures of iPP and TBBPA.

Equation 3.2 can be linearized by taking double logarithms as

$$\ln \left\{ \ln \left( \frac{1}{1 - X_t} \right) \right\} = \ln(K) + n \ln(t) \quad (3.3)$$

The crystallization half-time ( $t_{1/2}$ ), which corresponds to a time at which 50% of ultimate crystallinity is reached, can be calculated by equation 3.4.

$$t_{1/2} = \left( \frac{\ln(2)}{K} \right)^{1/n} \quad (3.4)$$

Crystallization kinetics was evaluated quantitatively by the values of  $K$  and  $t_{1/2}$  and the mode of crystallization was estimated by the value of  $n$ . Figure 3.9 shows that crystallization rate increases noticeably when TBBPA is introduced to iPP, and that the effect of TBBPA on the crystallization of iPP is almost saturated at 5 wt.% TBBPA. When the samples were quenched to 117 °C, complete crystallization of neat iPP occurs in about 2.5 minutes, but complete crystallization of iPP/TBBPA mixtures occurs in about 0.5 minutes (Figures 3.9a). Effect of TBBPA concentration (5 wt.% – 20 wt.%) on the crystallization rate is negligible (Figure 3.9b). As the quenching temperature increases, the crystallization rate decreases for all of the samples. The same trend was observed for the effect of TBBPA on crystallization rate (Figures 3.9c - 3.9f).

Figure 3.10 examines the effect of TBBPA on the crystallization of iPP in a more quantitative fashion. The mode of crystallization as represented by the exponent ‘ $n$ ’ in the Avrami equation does not change much in the presence of TBBPA (Figure 3.10a). The value of ‘ $K$ ’ in the Avrami equation, which represents the crystallization rate, increases significantly in the presence of TBBPA (Figure 3.10b).

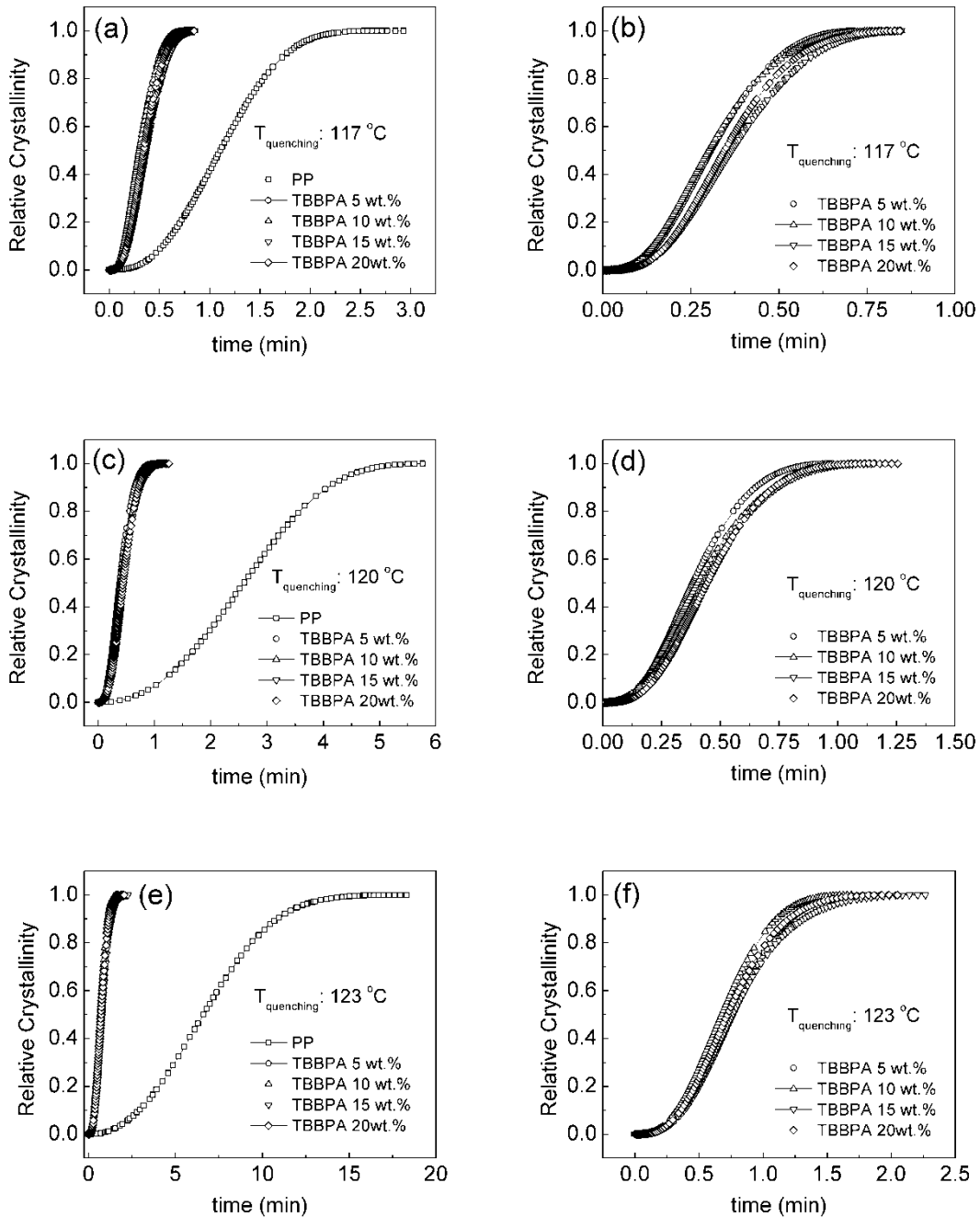


**Figure 3.9.** Relative crystallinity ( $X_t$  in equation 3.1) as a function of time as measured by quenching each molten sample to predetermined temperatures ( $T_q$ ). (a)  $T_q$ :  $117\text{ }^{\circ}\text{C}$ , (b) effect of TBBPA content at  $T_q$ :  $117\text{ }^{\circ}\text{C}$ , (c)  $T_q$ :  $120\text{ }^{\circ}\text{C}$ , (d) effect of TBBPA content at  $T_q$ :  $120\text{ }^{\circ}\text{C}$ , (e)  $T_q$ :  $123\text{ }^{\circ}\text{C}$ , (f) effect of TBBPA content at  $T_q$ :  $123\text{ }^{\circ}\text{C}$ .

The crystallization half-time ( $t_{1/2}$ ), which is a function of both ' $n$ ' and ' $K$ ', decreases significantly in the presence of TBBPA, indicating that TBBPA acts to increase the crystallization rate of iPP (Figure 3.10c). Since TBBPA is not likely to act as a nucleating agent for the crystallization of iPP as discussed above, the increased crystallization rate of iPP in the presence of TBBPA is most likely due to the enhanced diffusion of iPP molecules to the crystal growing sites because the liquid TBBPA can greatly reduce the viscosity of the mixtures, as will be discussed in the next section.

### **3.4.3. Viscosity**

Steady state shear viscosity was measured to evaluate the effect of TBBPA on processability. Figure 3.11 shows that the viscosity decreases as the amount of TBBPA increases when the test temperature is above the melting temperature of the mixture, indicating that TBBPA functions like a processing aid at the test temperatures (180 °C, 200 °C). Enhanced processability by TBBPA is a great advantage over conventional solid particle toughening in which processing becomes difficult due to the sharp increase of melt viscosity.

### **3.4.4. Morphology of Composites**

Size, shape and dispersion of TBBPA particles were examined with 1 mm thick compression-molded specimens that were conditioned at room temperature for a week before cryo-fracture (Figure 3.12). Addition of 5 wt.% of TBBPA to iPP produces very small particles (typical diameters are far below 1  $\mu\text{m}$ ) along with a few rod-like crystals.

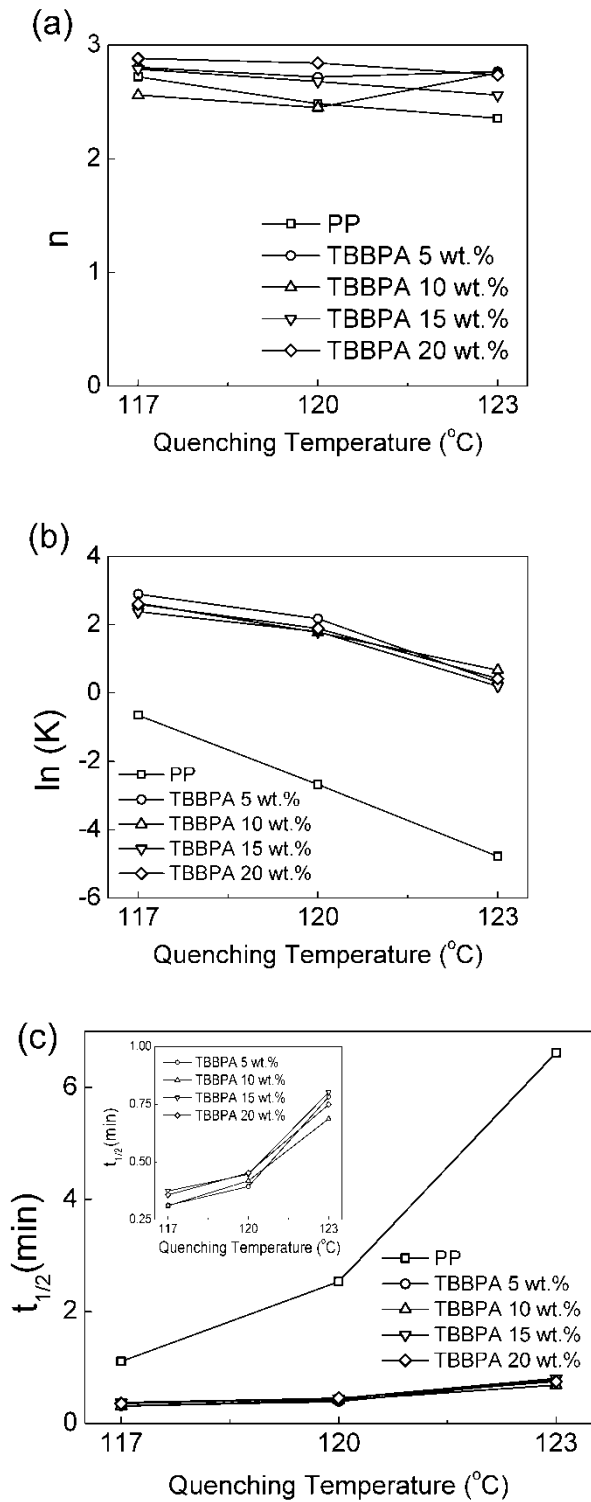


**Figure 3.10.** Crystallization kinetics as analyzed using the Avrami equation. (a)  $n$  versus quenching temperature, (b)  $\ln(K)$  versus quenching temperature, (c) crystallization half-time ( $t_{1/2}$ ) versus quenching temperature.

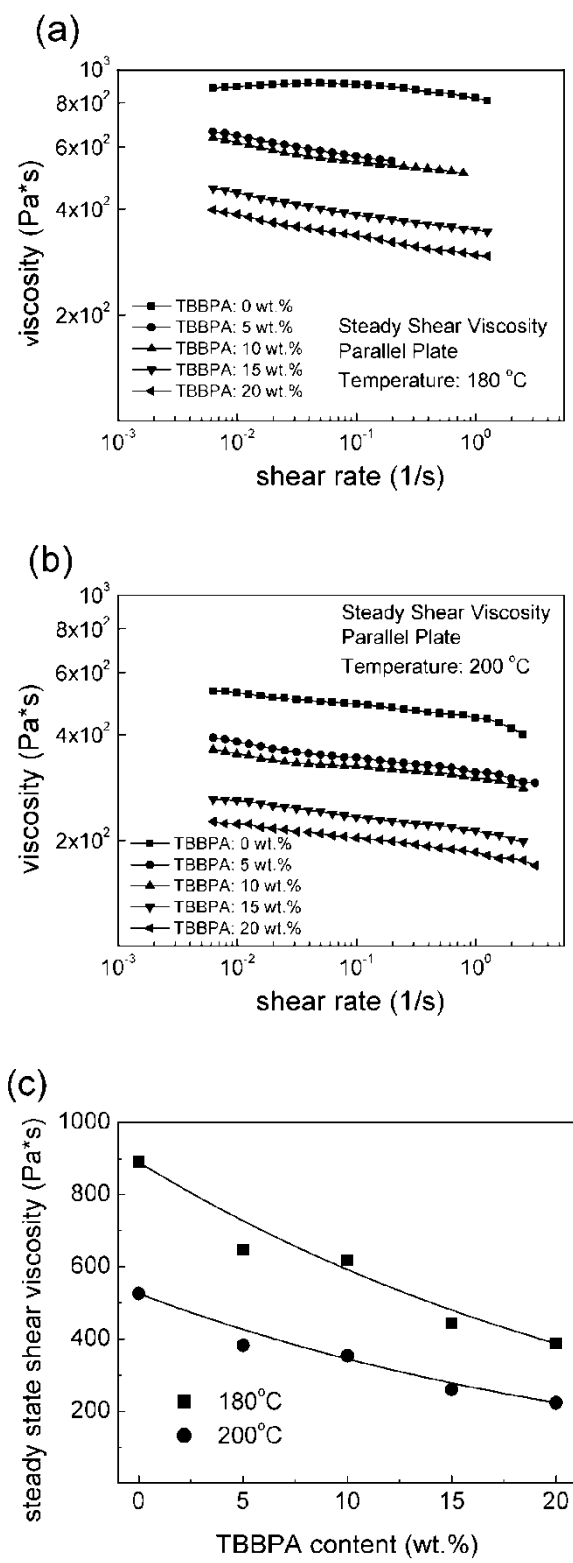


**Figure 3.11.** Steady state shear viscosity. (a) 180 °C, (b) 200 °C, (c) steady state shear viscosity as a function of TBBPA content (at a shear rate of  $0.01 \text{ s}^{-1}$ ).

As the amount of TBBPA increases, the average particle size also increases. Most of the particles larger than 1  $\mu\text{m}$  are not spherical; they are composed of anisotropic, faceted particles. This is most likely due to the unique crystal growth pattern of TBBPA in the iPP matrix that forms while the mixture is cooled. Even if the samples are cooled quickly using two compression molding machines, the resulting samples almost always show anisotropic particles. Samples with 20 wt.% TBBPA show significant number of anisotropic particles with sharp edges, some of which are almost 10  $\mu\text{m}$  in size. These particles are potentially detrimental to fracture toughness.

### **3.4.5. Tensile Properties**

Figure 3.13 shows the engineering stress-strain curve obtained from tension tests performed at 10 mm/min cross-head speed and the tensile properties thus obtained are summarized in Figure 3.14. It can be clearly seen that the yield stress (taken as the peak stress) decreases with increasing TBBPA concentration. This indicates de-wetting of TBBPA particles prior to plastic deformation (Figure 3.14a). Elongation-at-break increases as TBBPA content increases up to 15 wt.%. This results in an increase of tensile toughness (as calculated from the area under the stress-strain curve). However, 20 wt.% addition of TBBPA causes the elongation-at-break to decrease, possibly due to poor dispersion which produces oversized particles that might act as defects (Figure 3.14c). Young's modulus as calculated from the initial 2 % strain range does not change much (Figure 3.14b). It is known that the addition of soft particles causes significant decrease in modulus while rigid particles causes the modulus to increase noticeably.<sup>45</sup> In this regard, TBBPA acts like rigid particles but the expected increase in modulus is

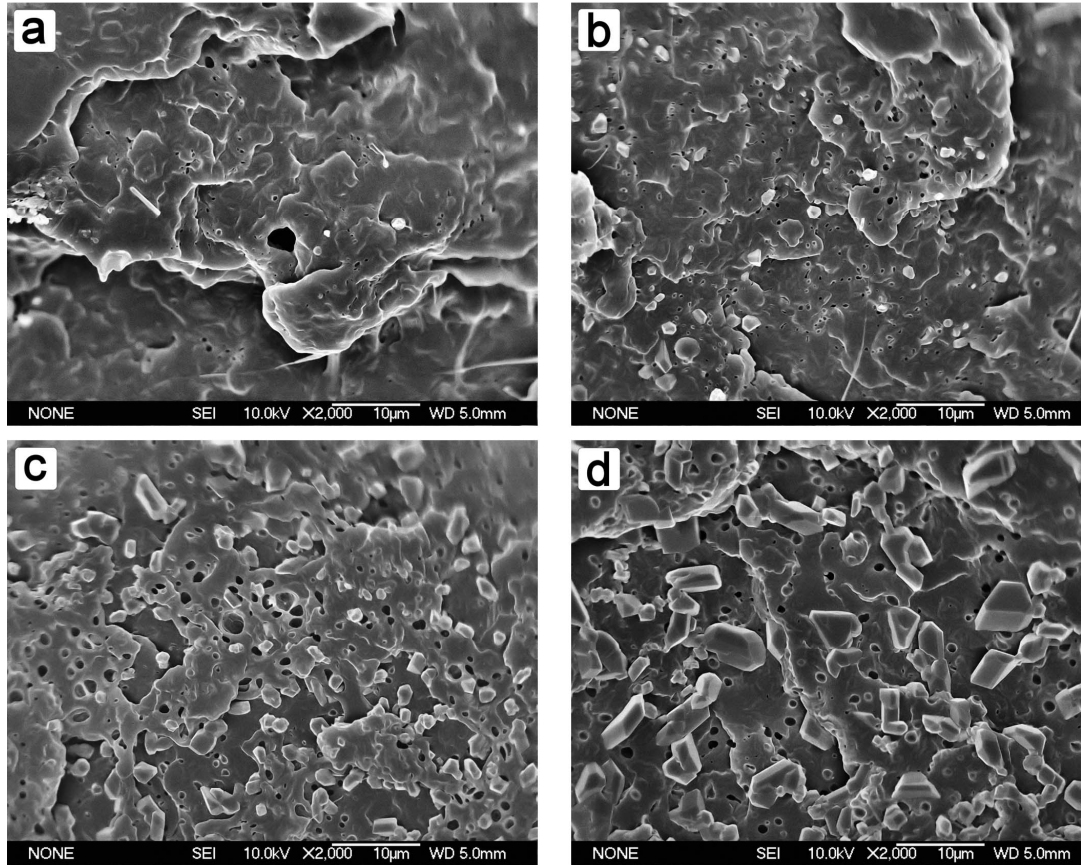


**Figure 3.12.** SEM micrographs of composite materials. (a) 5 wt.% TBBPA/iPP, (b) 10 wt.% TBBPA/iPP, (c) 15 wt.% TBBPA/iPP, (d) 20 wt.% TBBPA/iPP.

compromised by both the low mechanical properties of the TBBPA particle itself and weak adhesion to the polymer matrix.

The morphology around TBBPA particles clearly shows the de-wetting of the particles from the polymer matrix during tensile deformation (Figure 3.15). SEM micrographs were taken from tensile specimens of iPP/TBBPA (85/15, wt./wt.) which were recovered after the tension test, and sectioned along the direction of deformation to investigate the evolution of de-wetting around TBBPA particles. Figure 3.15a shows the morphology around TBBPA particles that were under tension, but did not undergo necking. De-wetting of polymer matrix around the TBBPA particles can be seen (marked with arrows) which suggests weak adhesion between the two components. The overall morphology shows elliptical cavities that are stretched parallel to the direction of tension (Figure 3.15b). In the necking region, de-wetted regions of polymer matrix are further stretched to form highly elongated cavities as marked with arrows in Figure 3.15c. The necking region shows highly elongated cavities (Figure 3.15d). De-wetting and the subsequent plastic flow (void growth) around TBBPA particles contributed to increased elongation-at-break and increased tensile toughness.

#### **3.4.6. Fracture Toughness**

The fracture toughness as measured from three point bending tests at room temperature is shown in Figure 3.16 and summarized in Table 3.2. Total fracture energy ( $J_Q$ ), which is the sum of energy release rate from brittle fracture response ( $J_{el}$ ) and the plastic component from J-integral work of fracture  $\left(2 \int P dx / \{B(W-a)\}\right)$ , is calculated by equation 3.5 as suggested by Lendes and Begley,<sup>60</sup>

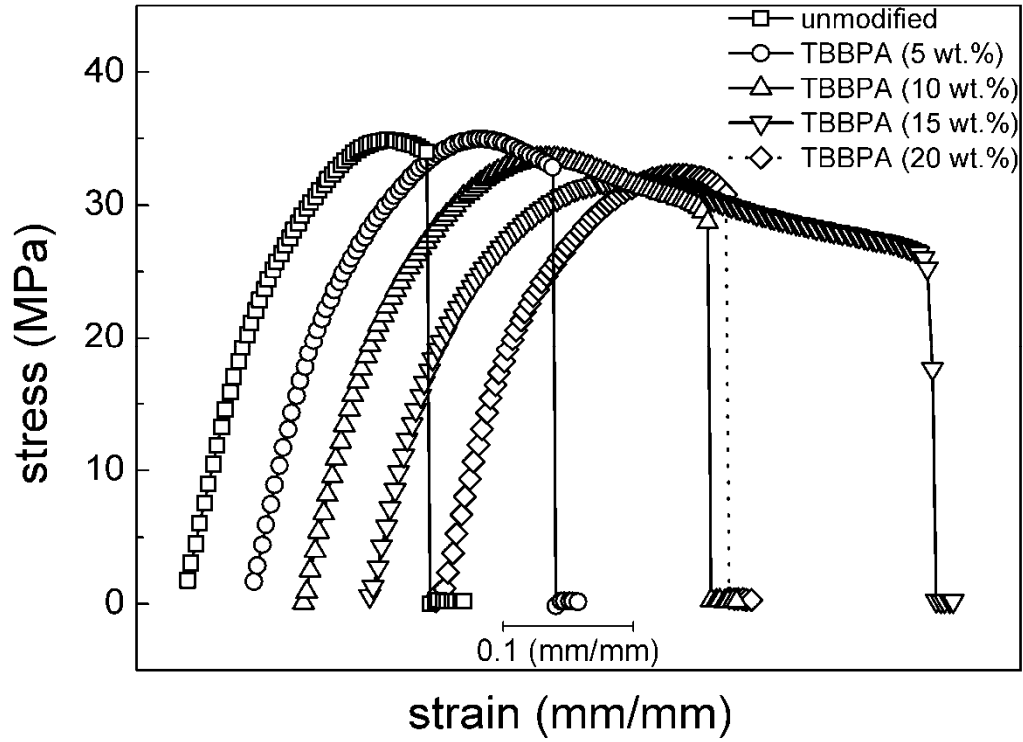


**Figure 3.13.** Engineering stress versus strain curve measured at room temperature (Curves are shifted along the strain axis for clarity).

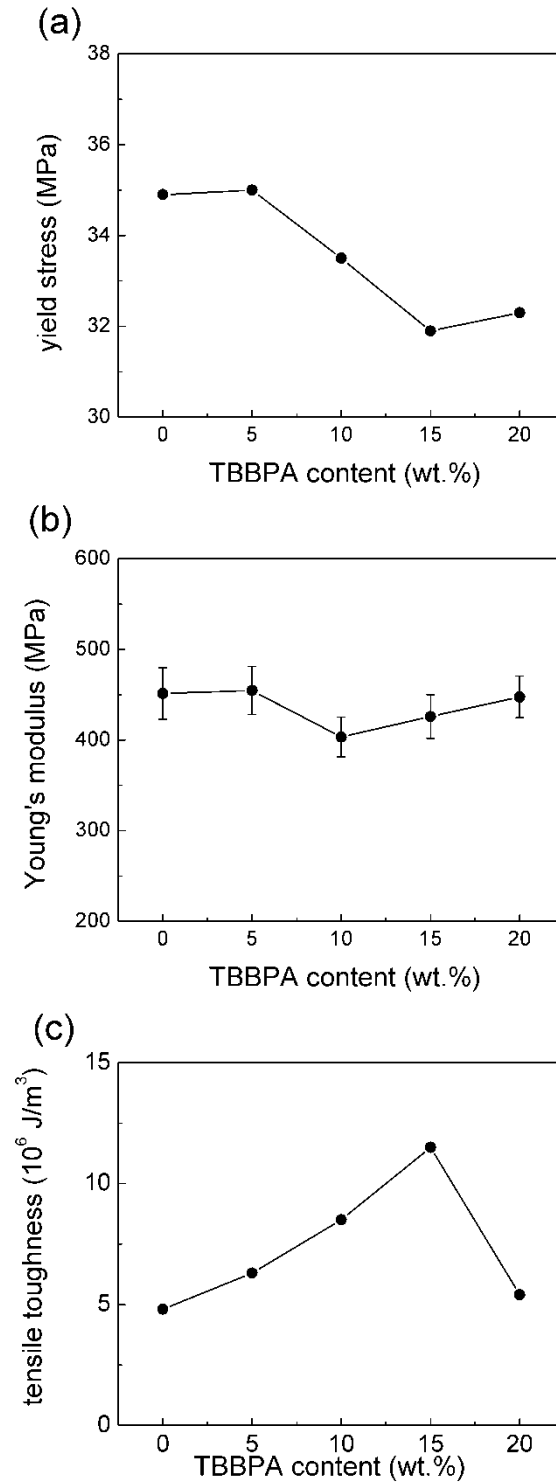


**Figure 3.14.** Summary of tensile properties measured at room temperature. (a) yield stress versus TBBPA content, (b) Young's modulus versus TBBPA content with error bars, (c) tensile toughness versus TBBPA content, as calculated from the area under the stress versus strain curve.

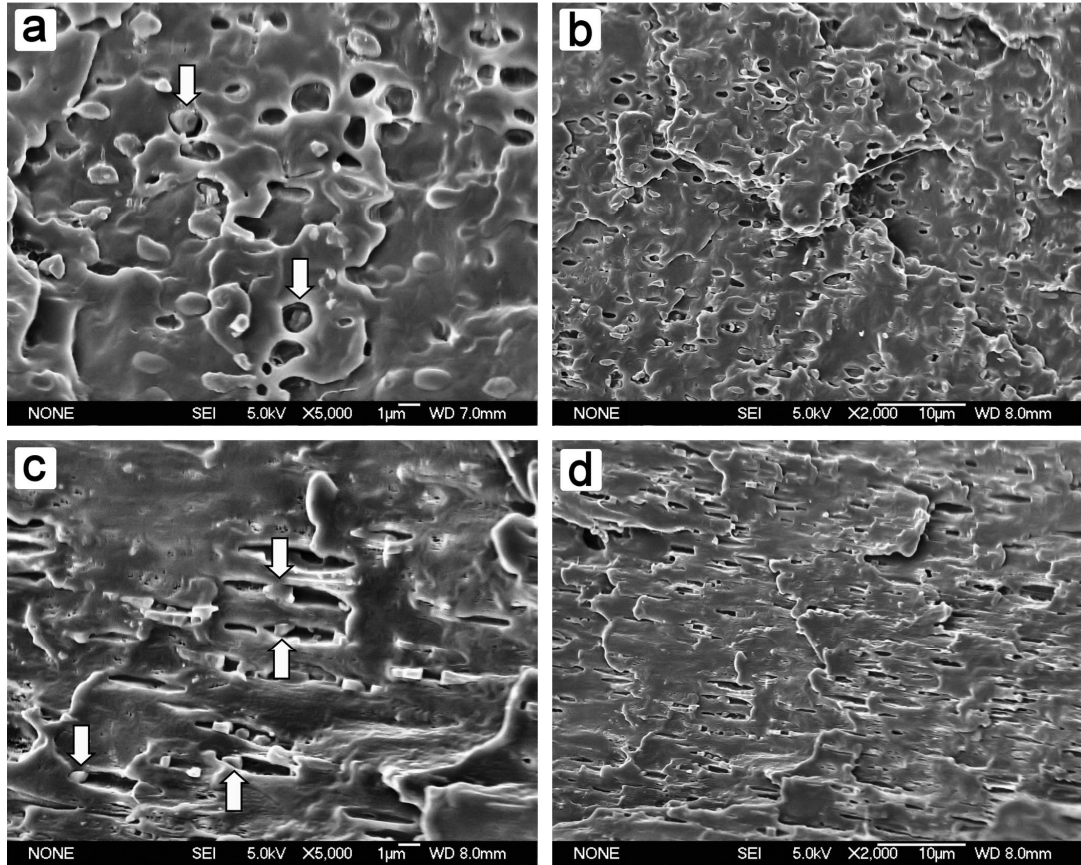


**Figure 3.15.** SEM micrographs of iPP + 15 wt.% TBBPA (Cross-sections are obtained by cryo-cutting of the tensile specimens after the tension test along the direction of deformation). (a) outside of necking region at high magnification, (b) outside of necking region at low magnification, (c) necking region at high magnification, (d) necking region at low magnification.

$$J_Q = J_{el} + \frac{2 \int P dx}{B(W-a)} = \frac{K_Q^2}{E/(1-\nu^2)} + \frac{2 \int P dx}{B(W-a)} \quad (3.5)$$

where  $P$  and  $x$  are load and displacement in three point bending test, respectively,  $B$  is the thickness,  $W$  is the width,  $a$  is the pre-crack length of SENB specimen,  $K_Q$  is stress intensity factor and  $E$  is Young's modulus. Poisson's ratio ( $\nu$ ) is assumed to have a typical value of 0.35. SENB specimens with 6 mm in thickness were tested at 50 mm/min cross-head speed. The stress intensity factor decreases as TBBPA content increases. This is most likely due to the large agglomerates that triggered brittle fracture during the deformation test. The total fracture energy of 10 vol % TBBPA/iPP composite is lower than that of neat iPP while further increase in TBBPA content (15 – 20 vol %) shows an increasing trend in total fracture energy due to an increase in the plastic component of the total fracture.

The trends in fracture toughness results do not agree with the tensile toughness results. As TBBPA content increases, tensile toughness increases mainly due to the increase in elongation-at-break, but fracture toughness decreases due to premature brittle failure. As discussed by Thio et al., this is not surprising since these two test methods are fundamentally different.<sup>49</sup> In case of the slow tensile test, the whole gauge volume responds to the applied stress. However, only the material directly in front of the notch tip, which exhibits a very low level of plastic response, will contribute to the measured fracture toughness. The presence of a sharp notch together with higher test speed result in a large increase of local strain rate in the fracture toughness test, compared to the slow strain rate in the tensile test.

**Table 3.2.** Fracture toughness calculated from three point bending test at 50 mm/min crosshead speed

TBBPA (vol.%)	$K_Q$ (MPa*m <sup>1/2</sup> )	$J_{el}$ (kJ/m <sup>2</sup> )	$2 \int Pdx / (B(W-a))$ (kJ/m <sup>2</sup> )	$J_Q$ (kJ/m <sup>2</sup> )
0	2.13	10.2	13.0	23.2
10	2.14	10.3	7.6	17.9
15	1.64	6.0	17.6	23.6
20	1.27	3.6	22.2	25.8

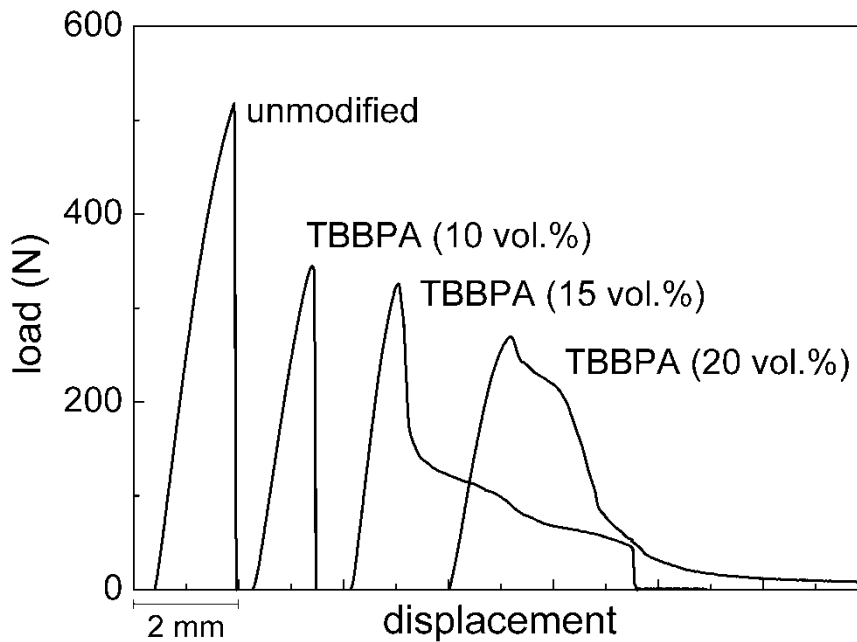
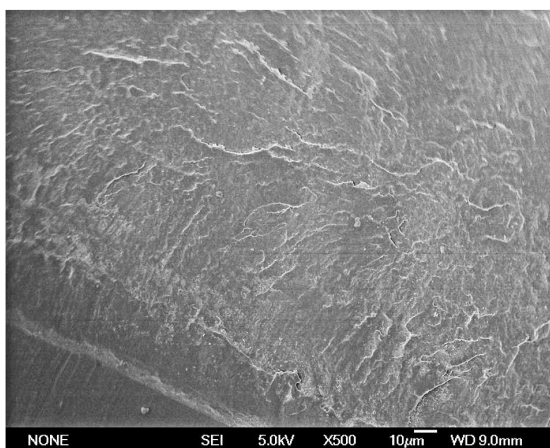


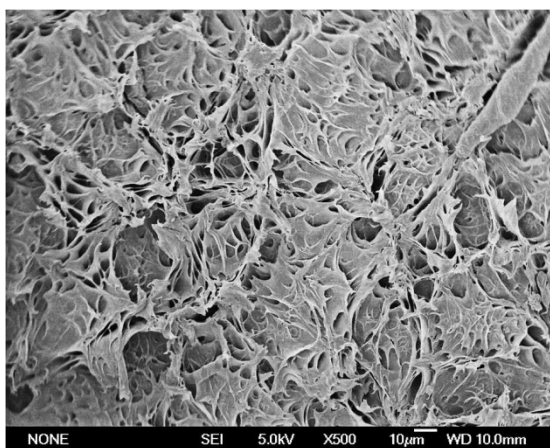
**Figure 3.16.** Load versus displacement curve from the three point bending test for single-edge notched bend specimens performed at room temperature with cross-head speed of 50 mm/min (Curves are shifted along the displacement axis for clarity).

Fractured surfaces after the three point bending tests were investigated by SEM (Figure 3.17). Neat iPP shows featureless, clean surfaces indicating highly brittle fracture behavior (Figure 3.17a). In contrast, TBBPA-containing samples exhibit highly stretched appearances near the crack tip in which strain is highly concentrated, indicating the occurrence of de-wetting followed by plastic flow (Figure 3.17b). However, the overall resistance to crack propagation becomes significantly lower as evident from the noticeably decreased peak load observed upon addition of TBBPA. This is likely due to the premature failure caused by oversized TBBPA particles (Figure 3.11). Since the crack propagates through the path with the least resistance, only the weakest material points in front of the crack contribute to the total fracture energy. If the propagating crack encounters oversized TBBPA particles, flaw-induced brittle fracture would result without any appreciable resistance from the polymer matrix. It seems that the initially promising response (de-wetting followed by plastic flow) cannot be maintained due to the large flaws caused by slow cooling of thick specimens and poor dispersion of TBBPA particles. A highly stretched morphology is observed only near the crack-tip region; the fractured surface becomes smooth as the distance from the crack tip increases (Figure 3.17c).

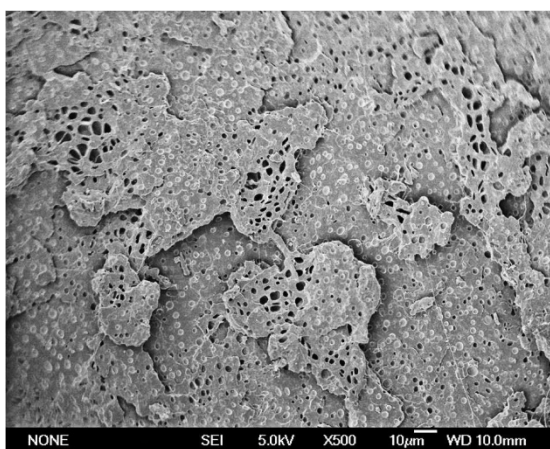
Several authors<sup>6,51</sup> have argued that the surface-to-surface interparticle distance, which is determined by the volume fraction of the particle and the size of the particle, is a key factor that governs the fracture behavior. According to this argument, crystallization of semi-crystalline polymers is initiated from the incoherent polymer-particle interface and forms low energy planes of oriented crystals with specific thickness in the near-interface layer of the polymer with specific thickness.



(a)



(b)



(c)

**Figure 3.17.** SEM micrographs of the fractured surface after the three point bending test. (a) neat iPP; near crack tip region, (b) TBBPA 10 vol.%; near the crack tip region, (c) TBBPA 10 vol.%; far-away region from the crack tip (scale bar is 10  $\mu\text{m}$ ).

If the thickness of this oriented crystalline layer between particles is below a certain critical value (critical ligament thickness, which depends on the polymer matrix), easily stretchable ligaments with reduced plastic resistance will percolate throughout the structure and promotes a plastic response of the entire material. If the surface-to-surface distance is above the critical ligament thickness, oriented layers of reduced plastic resistance around particles do not percolate through the structure and the overall plastic resistance is substantially elevated causing the fracture behavior to be governed by the extrinsic flaws that leads to premature brittle fracture. If these arguments are applied to our case, the fundamental requirement would be that TBBPA should crystallize first so that iPP crystals can grow from the surface of these TBBPA particles and form low energy crystal planes to facilitate plastic deformation. In this regard, the crystallization of neat TBBPA was investigated by DSC. In the first heating run in DSC, an endothermic melting peak appears at 187 °C, but no exothermic crystallization peak is observed in the subsequent cooling run (Figure 3.18a). At the end of the first cycle, TBBPA is likely in its super-cooled state. In the second heating run, an exothermic (crystallization) peak appears at 71 °C, followed by a melting peak at 167 °C (Figure 3.18b). It seems that the mobility of the super-cooled TBBPA increases enough at 71 °C so that the rearrangement of the unstable TBBPA takes place, which leads to crystallization of TBBPA. Those crystals melt at 167 °C. However, there is no exothermic (crystallization) peak in the subsequent cooling, even if the cooling rate is decreased from 10 °C/min to 5 °C/min. A third cycle performed at 5 °C/min rate shows the same behavior as the second cycle (result not shown). This indicates that the crystallization of neat TBBPA is slow and does not occur at 5 - 10 °C/min cooling rates.

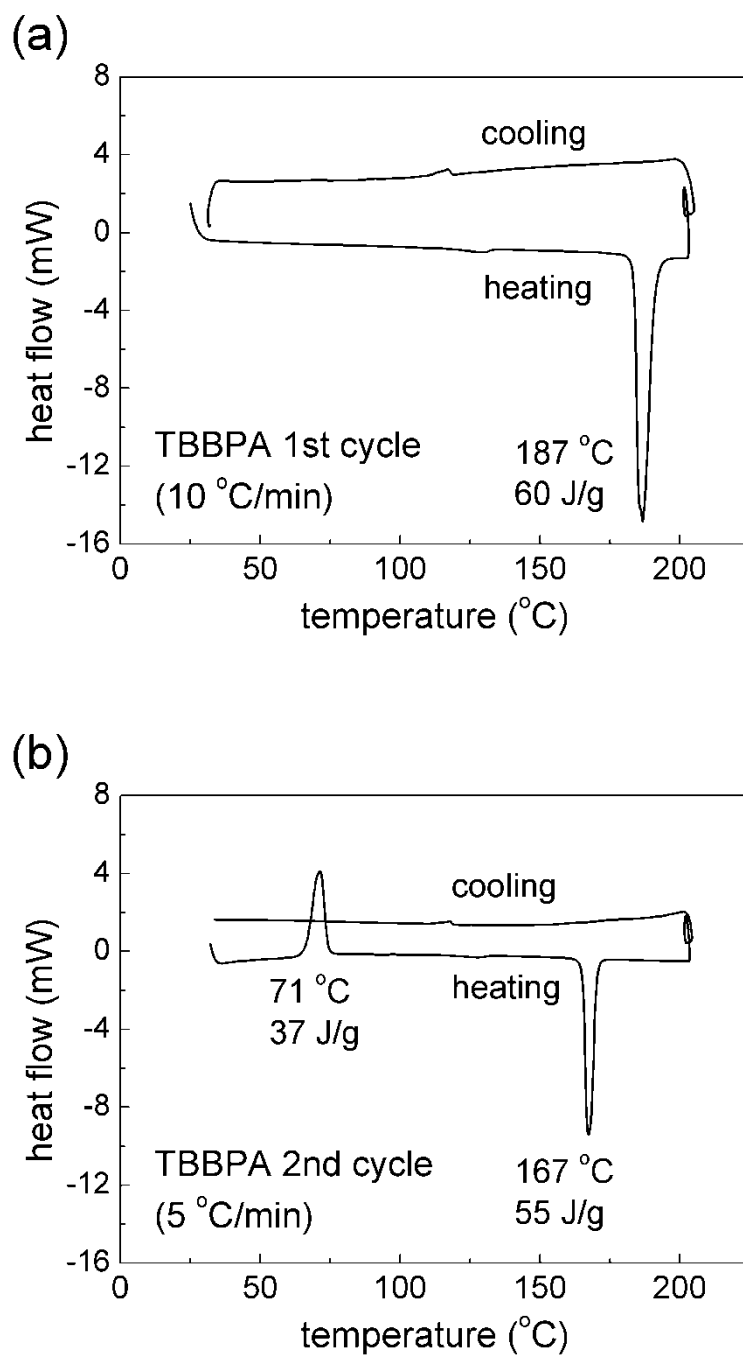


**Figure 3.18.** DSC thermograms of neat TBBPA. (a) first cycle of heating and cooling at 10 °C/min, (b) second cycle of heating and cooling at 5 °C/min.

Since the actual samples were prepared at much higher cooling rates, it is likely that iPP crystallizes first and TBBPA remains in a super-cooled liquid state during the cooling process. Since the super-cooled TBBPA is unstable, it would gradually crystallize to form large crystals during the conditioning step at room temperature (which is above the  $T_g$  of iPP) as shown in Figure 3.8.

The morphology along the crack propagation path was investigated for an iPP compound containing 15 vol.% TBBPA using optical microscopy, confocal microscopy and SEM. The sample was taken from the core section of the incompletely broken crack of the four point double crack specimen after fracture, followed by cryo-microtoming, as suggested by Sue et al.<sup>58</sup> (Figure 3.19). A stress-whitening zone is not observed by optical microscopy, indicating that the plastic resistance near the crack tip is not significant (Figure 3.20a). The substantial amount of large agglomerates of TBBPA particles in the micrograph clearly shows poor dispersion. Similar morphology is observed by confocal microscopy (Figure 3.20b). It can be seen that the crack propagates in nearly a straight direction, indicating that there is no appreciable toughening effect by a crack deflection mechanism. SEM shows that the particles not only aggregate to form large agglomerates, but also that the particles have anisotropic, sharp-edged shapes (Figure 3.20c). It is generally accepted that particles with sharp edges are more likely to induce brittle fracture and should be avoided to prevent premature brittle fracture. However, it is not possible to prevent the formation of these anisotropic crystals under the current experimental conditions. Preparation of 6 mm thick specimens for fracture toughness to ensure plane strain conditions inevitably results in relatively low cooling rates in the core sections of the specimens where large

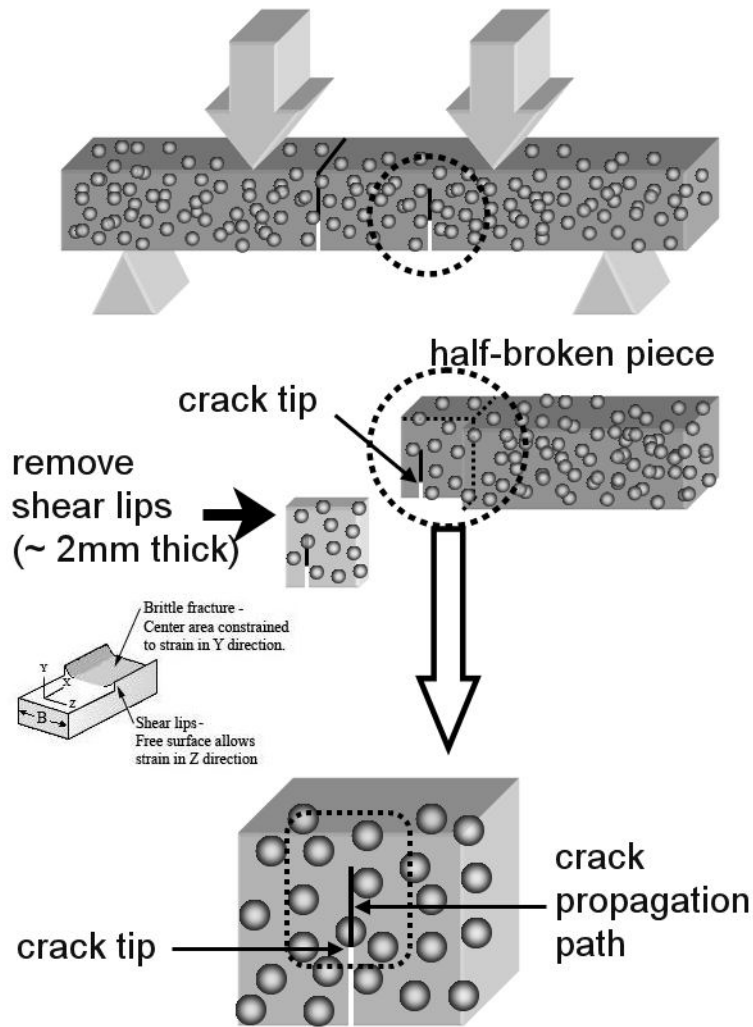
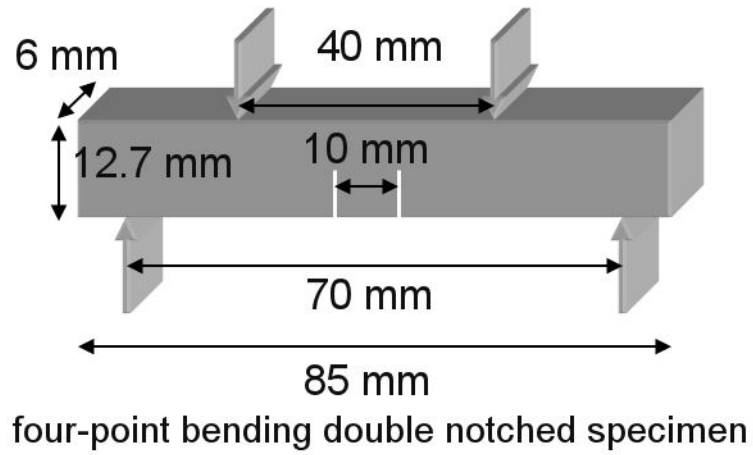


**Figure 3.19.** Four-point double notched specimen to investigate the crack propagation path.

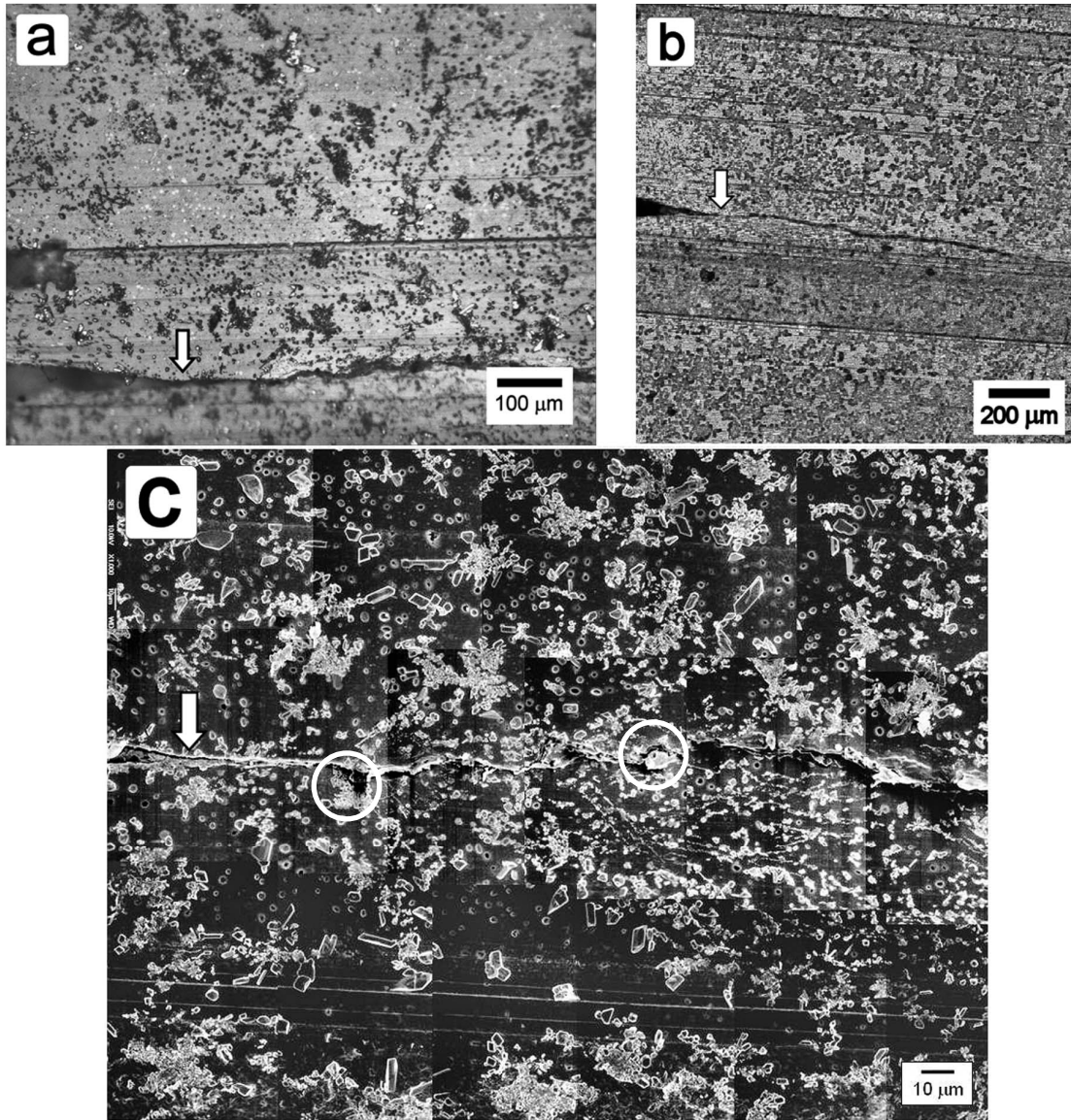


**Figure 3.20.** Morphology along the crack propagation path (Crack tip region is indicated with an arrow). (a) optical microscopy, (b) confocal microscopy, (c) SEM (oversized flaws in the crack path are indicated inside a circle).

anisotropic crystals of TBBPA form. The dependence of particle geometry on thermal treatment is currently one drawback of this strategy.

### 3.4.7. Effect of Diluent Identity

Interactions between the polymer and the crystallizable diluent may have strong effects on the properties of the composite materials. In this regard, phthalic anhydride (PA) was chosen as an alternative diluent for TBBPA to prepare composite materials with polypropylene and the results are discussed in comparison with iPP/TBBPA composites.

Table 3.3 summarizes the physical properties of PA and TBBPA. PA is expected to be less soluble in iPP compared to TBBPA due to the larger gap in solubility parameters with iPP. The melting temperature of PA is lower than that of TBBPA, which will affect the phase separation behaviors.

**Table 3.3.** Physical properties of phthalic anhydride and TBBPA

Properties	Unit	Phthalic Anhydride (PA)	TBBPA
Molar Mass	g / mol	148	544
Density	g / cm <sup>3</sup>	1.53	2.12
Melting Temperature	°C	131	187
Solubility Parameter	MPa <sup>1/2</sup>	22.5	20.2

Thermal properties of PA/iPP composites are shown in Figures 3.21 and 3.22. Melting temperature depression of iPP in the presence of PA is not significant, possibly due to the large gap in solubility parameters (Figure 3.21). However, the crystallization temperature of iPP increases significantly in the presence of PA (Figure 3.22). This observation indicates that PA is less soluble in iPP compared to TBBPA and functions as a nucleating agent for iPP during cooling.

Glass transition temperatures decrease as PA content increases in PA/iPP composites, although the change in temperature is only within 5 °C range (Figure 3.23). This indicates that PA crystals may act as a plasticizer for solid iPP.

Micrographs from optical microscopy support that PA acts more like a nucleating agent for iPP. The size of iPP spherulites decreases significantly by the addition of PA (Figure 3.24). This observation is in contrast with TBBPA/iPP composites, in which the size of iPP decreases only slightly (Figure 3.7). The size of iPP spherulites is reduced far below 10 μm by 10 wt.% addition of PA (Figure 3.24b). At 20 wt.% loading of PA, needle-like crystals of PA can be seen in iPP matrix (Figure 3.24c). This observation indicates that there is a limit in solubility of PA in iPP and that the excess amount PA beyond the solubility limit would form its own crystal.

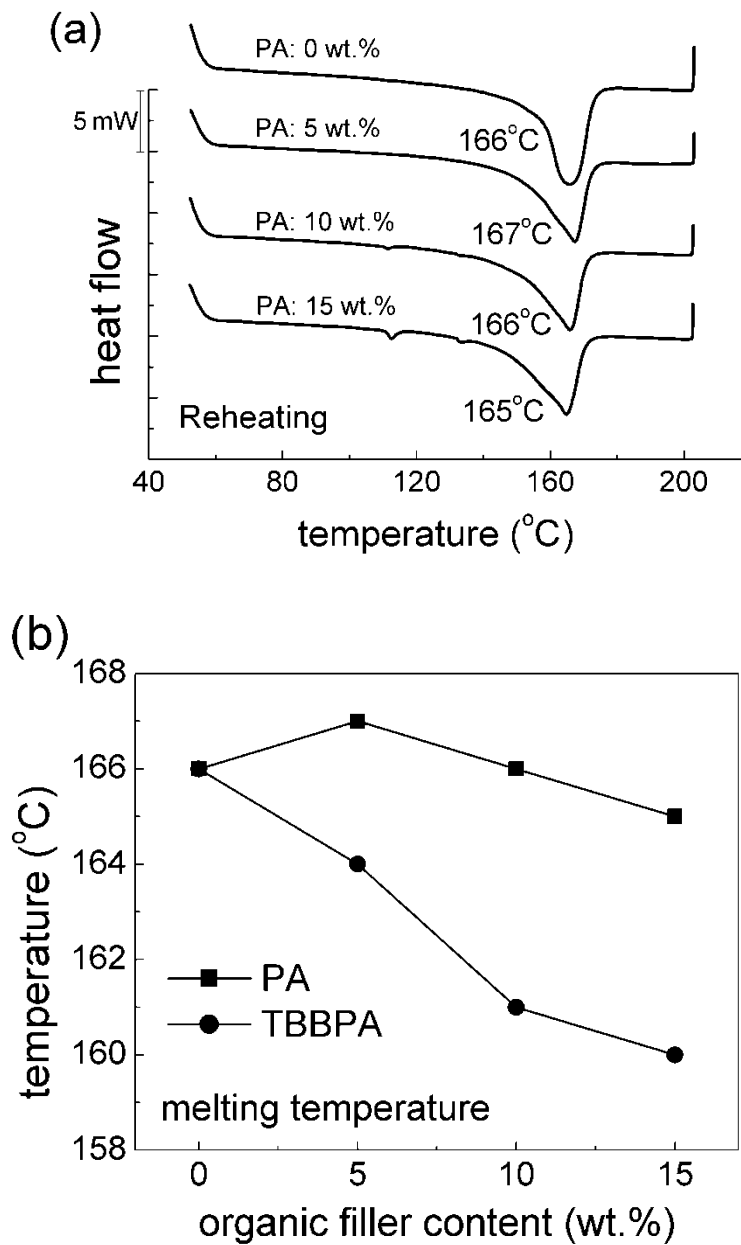


**Figure 3.21.** Melting temperature of PA/iPP composites as measured by DSC at 10 °C/min. (a) thermograms from DSC reheating runs, (b) melting temperature of PA/iPP composites and TBBPA/iPP composites.

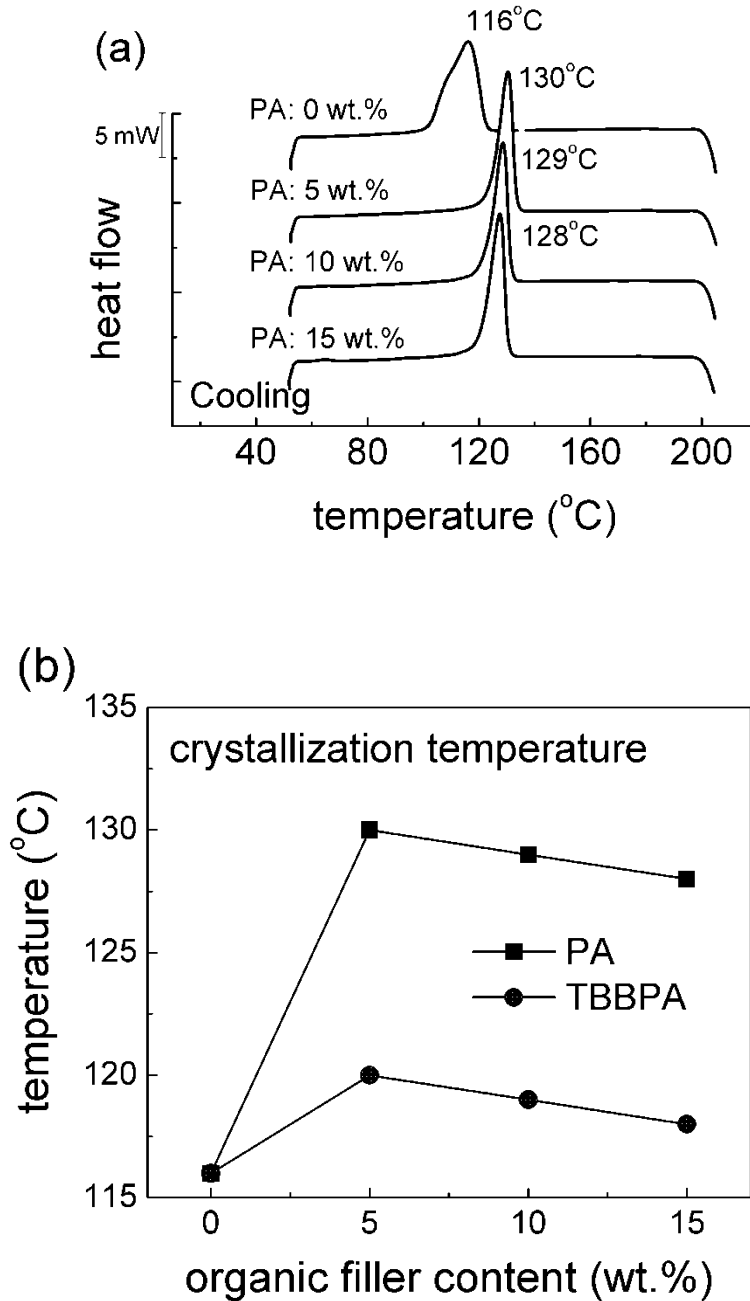


**Figure 3.22.** Crystallization temperature of PA/iPP composites as measured by DSC at 10 °C/min. (a) thermograms from DSC cooling runs, (b) crystallization temperature of PA/iPP composites and TBBPA/iPP composites.

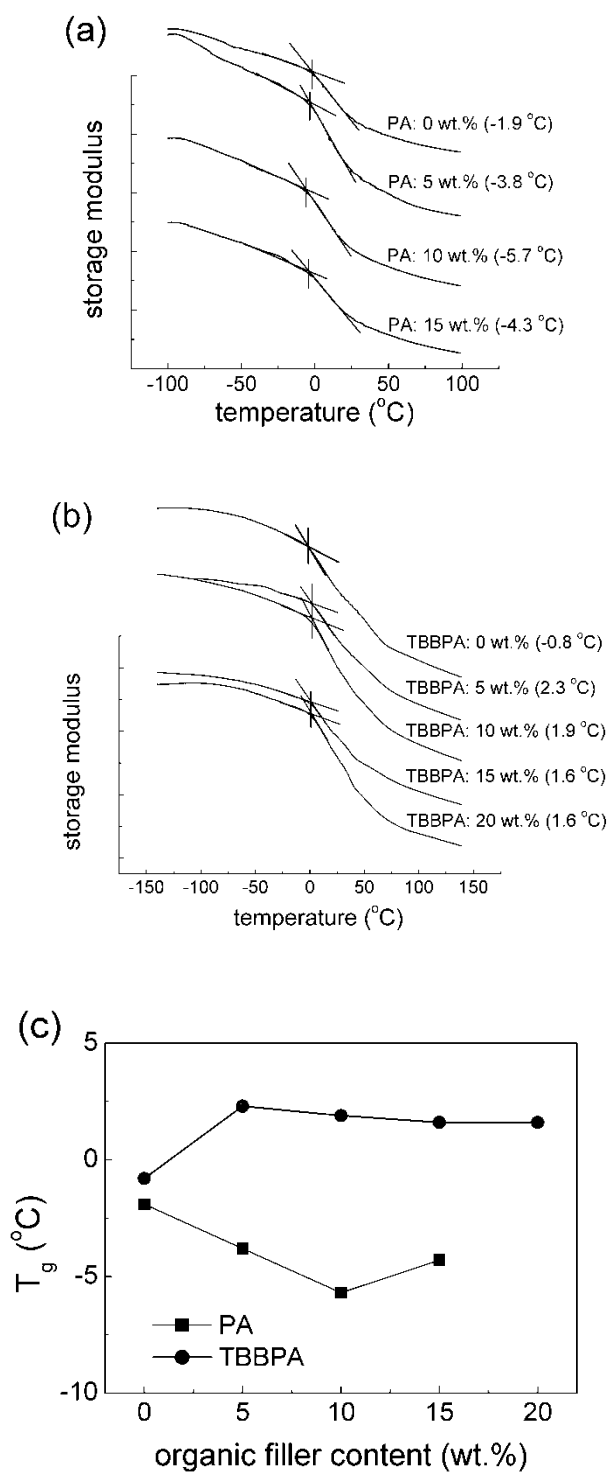
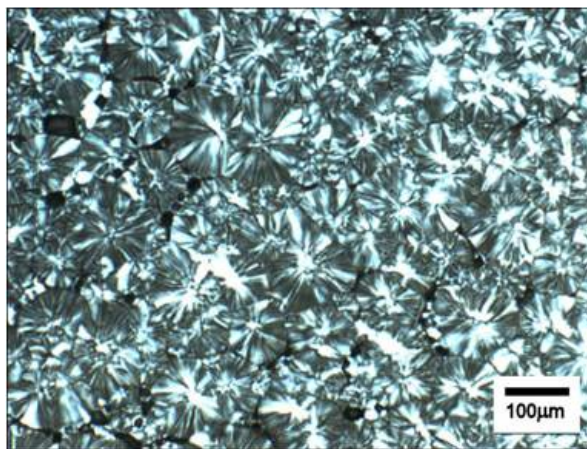
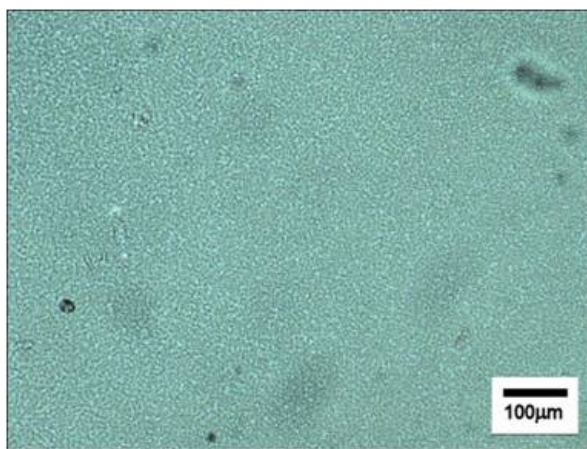


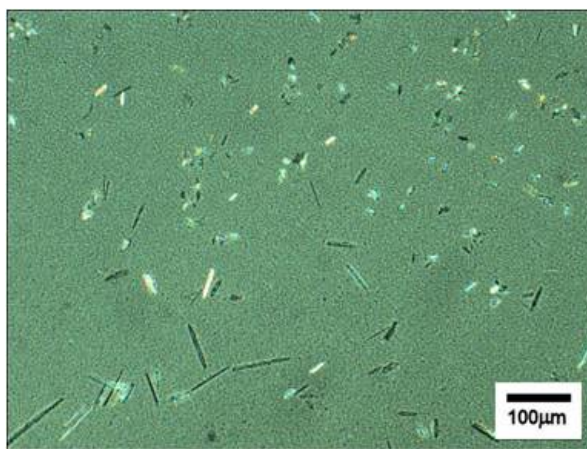
**Figure 3.23.** Glass transition temperature of PA/iPP composites as measured by DMA at 1 Hz, 3 °C/min heating rate. (a) PA/iPP composites, (b) TBBPA/iPP composites, (c) comparison of  $T_g$  between PA/iPP composites and TBBPA/iPP composites.



(a)



(b)



(c)

**Figure 3.24.** Micrographs of iPP spherulites taken by cross-polarized optical microscopy at room temperature. Each sample was cooled from 200 °C to room temperature at 10 °C/min. (a) neat iPP, (b) 10 wt.% PA/iPP, (c) 20 wt.% PA/iPP.

While PA also functions to decrease the viscosity of the mixture, PA is less effective compared with TBBPA. This becomes more evident as the testing temperature decreases. Although the melting temperature of PA is lower than that of TBBPA, PA is less soluble in iPP than TBBPA which causes more segregation between PA and iPP under shear process. The solubility of PA in iPP decreases as temperature decreases, and the segregation problem is likely to become more severe at lower temperatures. Steady state shear viscosity at 180 °C shows that the decrease in viscosity of the mixture is more noticeable for TBBPA than PA as the organic filler content increases (Figure 3.25a). This is most likely due to the better solubility of TBBPA in iPP compared to that of PA. At a higher test temperature (200 °C), the solubility of each organic filler in iPP increases and the difference in viscosity decrease between PA and TBBPA becomes less obvious, although TBBPA is still a better processing aid than PA at this temperature (Figure 3.25b).

Tensile properties of PA/iPP composites are very different from those of TBBPA/iPP composites as shown in Figures 3.26 and 3.27. Tensile yield stress of PA/iPP composites increases initially at 5 wt.% loading of PA, then decreases as PA content increases further (Figure 3.27a). Young's modulus of PA/iPP composites also increases at 5 wt.% loading of PA but does not change much as PA content increases further (Figure 3.27b). Tensile toughness, however, decreases as PA content increases (Figure 3.27c). PA is thought to act as a nucleating agent for iPP until it reaches the solubility limit and the stiffness of iPP increases, which causes the yield stress and Young's modulus to increase due to the increased stiffness of iPP itself.

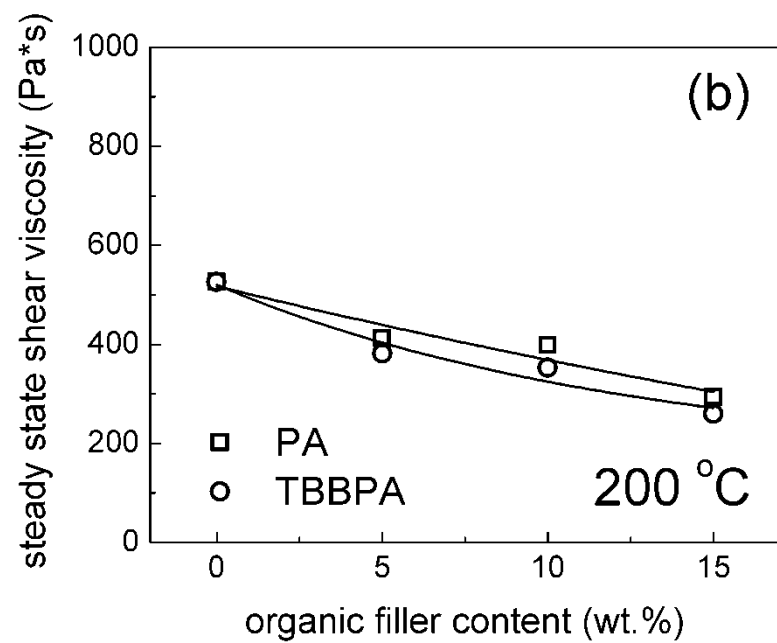
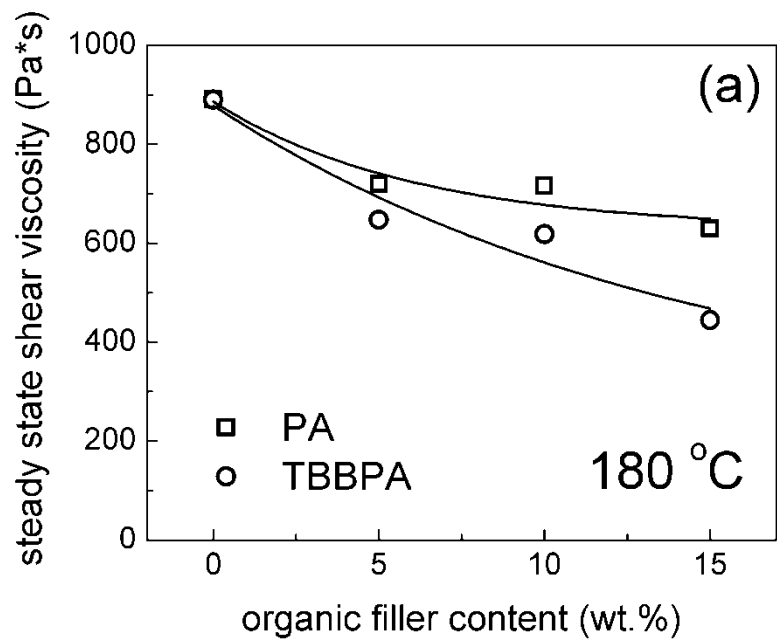


**Figure 3.25.** Steady state shear viscosity at the shear rate of  $0.01 \text{ s}^{-1}$ , using a parallel plate rheometer. (a) test temperature:  $180 \text{ }^\circ\text{C}$ , (b) test temperature:  $200 \text{ }^\circ\text{C}$ .

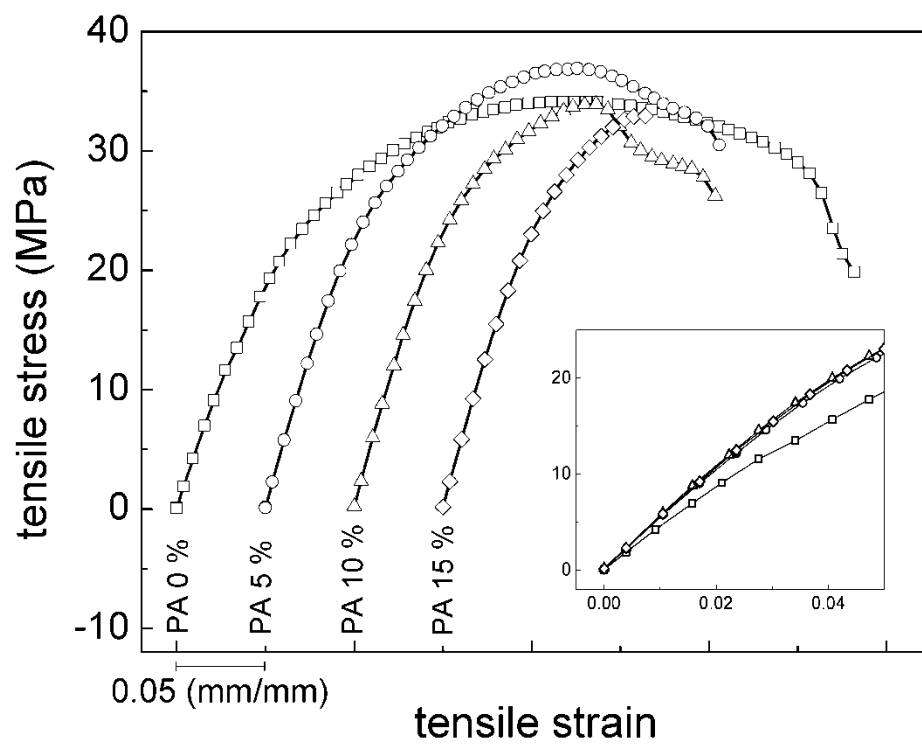


**Figure 3.26.** Engineering stress versus strain curve of PA / iPP composites. (curves are shifted along the strain axis for clarity). Inset plot is an initial response to compare the stiffness.

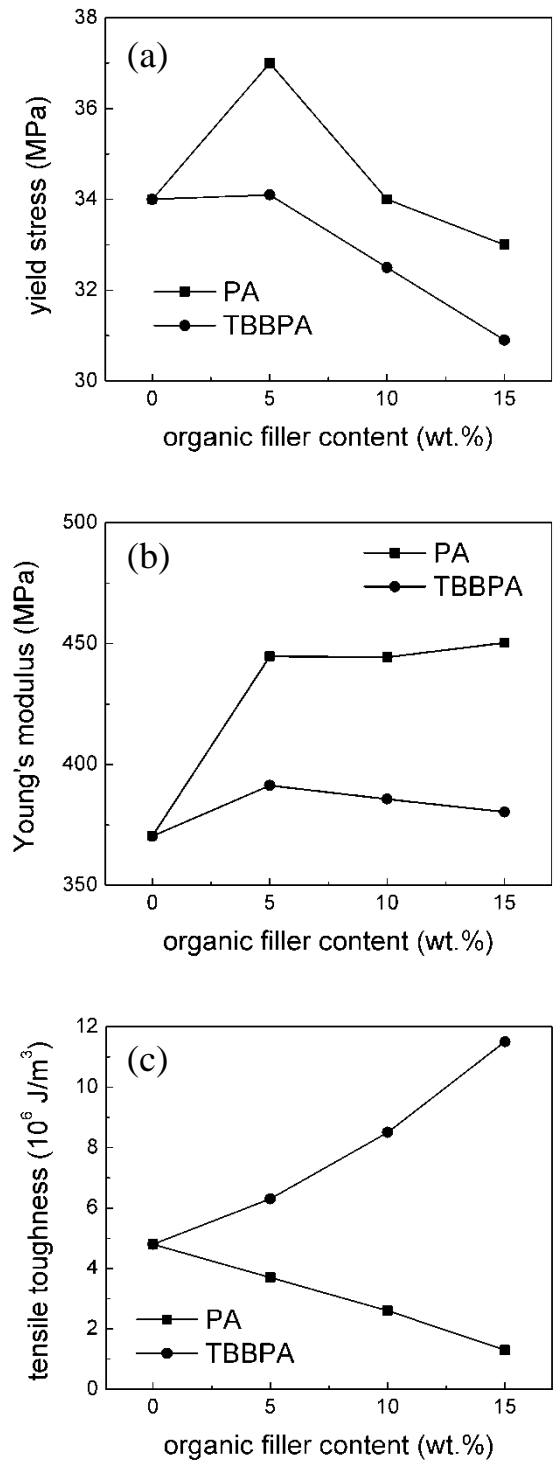


**Figure 3.27.** Summary of tensile properties. (a) yield stress, (b) Young's modulus, (c) tensile toughness as calculated from the area under the stress versus strain curve.

Further increase in PA content would yield insoluble PA in iPP that would form its own crystals. These PA crystals may act like organic fillers with weak interfacial strength with iPP, causing the yield stress to decrease (Figure 3.27a). Young's modulus does not change much for PA loading levels of 5 wt.% and higher, which indicates that PA initially acts as a nucleating agent to increase the stiffness of iPP matrix, but further increases in PA content cause formation of PA crystals and the modulus does not change (Figure 3.27b). However, PA/iPP composites become more brittle as PA content increases and the tensile toughness decreases, primarily due to the decreased elongation-at-break (Figure 3.27c).

Fracture toughness of PA/iPP composites as evaluated by stress intensity factor ( $K_Q$ ) increases at 5 wt.% loading of PA but decreases slightly as PA content increases further (Figure 3.28). Since  $K_Q$  probes the brittle response of the materials undergoing fracture, this behavior can be explained by the role of PA as a nucleating agent at low levels of loading that increases the stiffness (and brittleness) of iPP, which in turn forms its own crystals at higher levels of loading. It should be noted that only 3 mm thick single edge notched bend (SENB) specimens were used to compare the fracture toughness, which may induce ductile response even for brittle materials due to appreciable effect from the shear lips. When the specimen is not thick enough, unconstrained deformation at the free surfaces on both faces of the specimen occurs and the fracture response is affected by the easy deformation from those regions. This is clearly seen that the fracture behavior of neat iPP strongly depends on the thickness of the sample. If the thickness of the sample is 3 mm, plain strain condition is not met and the brittle neat iPP exhibits ductile response (Figure 3.28a). If, however, the thickness

of the sample is 6 mm, shear lip region is relatively small compared to the core section of the specimen and most part of the specimen undergoes constrained deformation (plain strain); neat iPP shows brittle response under this condition (Figure 3.16). This means that the specimen should be at least 6 mm thick to ensure plain strain to induce brittle fracture. The results shown in Figure 3.28 are, therefore, not accurate stress intensity factors and should be used for relative comparison purpose only between different samples tested at the same experimental conditions.

The morphology of PA/iPP composites shows that only a small amount of tiny crystals of PA exists at 5 wt.% loading (Figure 3.29a), but the size of PA crystals increases as PA content increases further (Figure 3.29b–d). This observation supports the previous discussion that PA initially acts as a nucleating agent, but further increases in PA content cause formation of PA crystals. The initial increase in stiffness (5 wt.% loading of PA) is likely due to the increased stiffness of iPP, since the PA particles are not likely to contribute to any change considering the amount and size of the particles (Figure 3.29a). It should be noted that while needle-like crystals of PA were observed by optical microscopy (Figure 3.24c), spherical particles of PA were observed by SEM (Figure 3.29). This is possibly due to the different cooling schemes (10 °C/min cooling for optical microscopy samples and rapid quenching from 200 °C to 40 °C for SEM samples).

Table 3.4 summarizes the qualitative difference in the effect of PA and TBBPA on the properties of polypropylene-based composite materials.

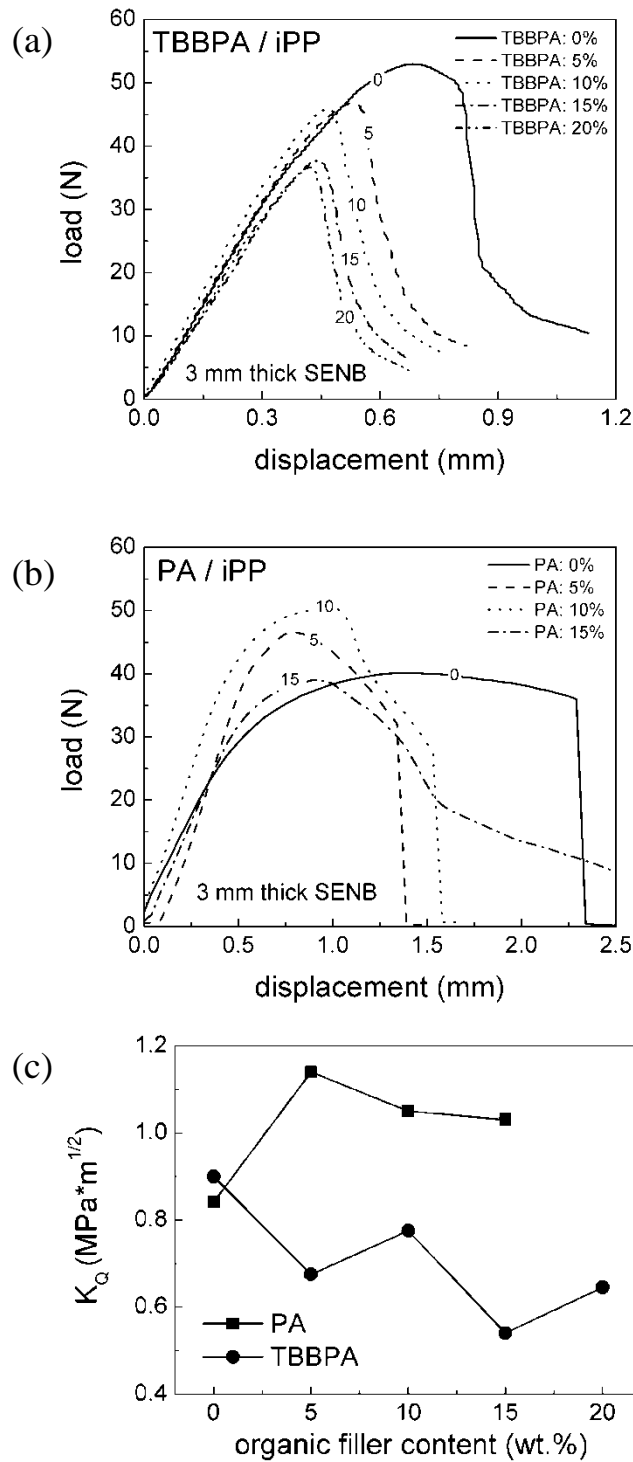
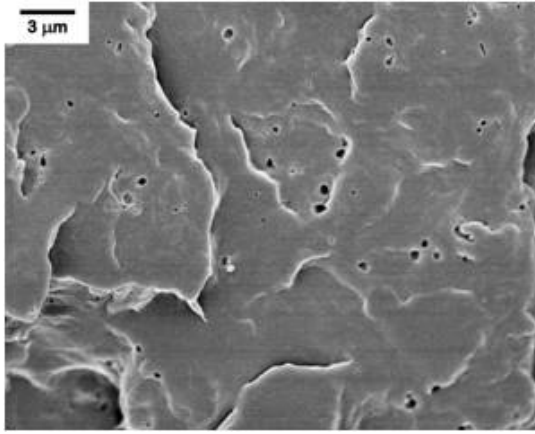
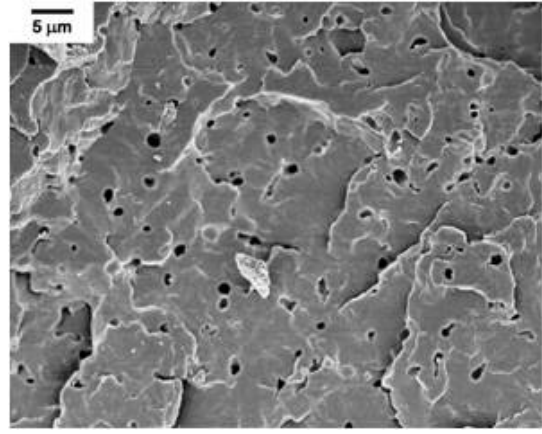


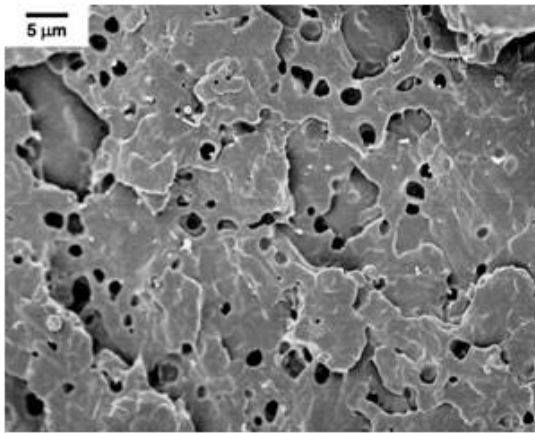
**Figure 3.28.** Fracture toughness as measured by stress intensity factor ( $K_Q$ ) using 3mm thick single edge notched bend (SENB) specimens. (a) load versus displacement for TBBPA / iPP composites, (b) load versus displacement for PA / iPP composites, (c) stress intensity factor as a function of organic filler content.



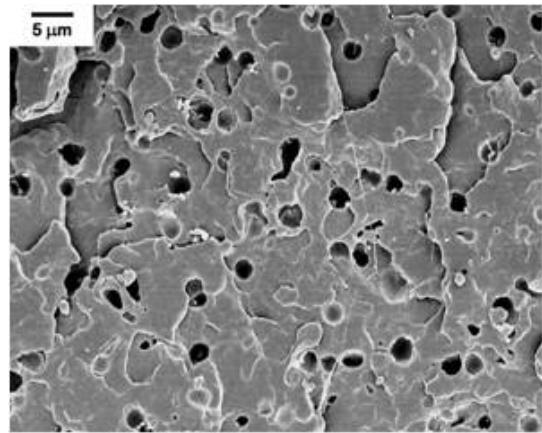
(a)



(b)



(c)



(d)

**Figure 3.29.** SEM micrographs of PA/iPP composite materials. (a) 5 wt.% PA in iPP, (b) 10 wt.% PA in iPP, (c) 15 wt.% PA in iPP, (d) 20 wt.% PA in iPP.

**Table 3.4.** Qualitative comparison between PA and TBBPA of their effect on material properties of polypropylene-based composites.

Properties	Phthalic Anhydride (PA)	Tetrabromo Bisphenol-A (TBBPA)
Solubility Parameter Difference between iPP and Organic Filler ( $\text{MPa}^{1/2}$ )	5	3
Young's Modulus	↑	–
Brittle Fracture Strength (Stress Intensity Factor)	↑	↓
Crystallization Temperature	↑↑	↑
Melting Temperature	–	↓
Glass Transition Temperature	↓	↑
Viscosity	↓	↓↓
iPP Spherulite Size	↓↓	↓

### 3.5. Conclusions

An organic crystalline compound (tetrabromobisphenol-A) was tested as a toughening agent for isotactic polypropylene (iPP), which forms a homogeneous mixture at high temperature and acts as a processing aid, but undergoes phase separation upon cooling to form crystalline particles and acts as a toughening agent. Viscosity decreased as tetrabromobisphenol-A (TBBPA) content increased at high temperature, indicating enhanced processability. The reduced viscosity facilitated the diffusion of iPP during crystallization and significantly accelerated the crystallization of iPP as a result. An increase in crystallization rate is beneficial to productivity in most polymer processing applications. Addition of TBBPA caused decreases in tensile yield stress, increases in elongation-at-break and tensile toughness and negligible changes in Young's modulus. This indicates that the interfacial adhesion between TBBPA particle and iPP matrix is weak and that as a consequence, the de-wetting of TBBPA particles occurs at the early stage of deformation. This was confirmed from the morphology of deformed regions determined by SEM. The fracture toughness as measured by three point bending test, however, decreased as TBBPA content increased. This is most likely due to the poorly dispersed, oversized particles. Micrographs taken along the crack propagation path showed large agglomerates of TBBPA particles with sharp edges, which could easily trigger premature brittle failure.

It was also found that the crystallization of TBBPA is very slow and small crystals do not form rapidly under these cooling conditions. Due to the slow crystallization of TBBPA, it is not clear whether iPP crystals can grow from the surface of TBBPA to form low energy crystal layers that should provide easy plastic

deformation, as other investigators have observed with rigid inorganic particles and soft rubber particles. In this regard, efficient organic crystalline compounds for toughening should form small crystals very quickly prior to polymer crystallization.

The effect of crystallizable diluents on the properties of iPP composites strongly depends on the identity of the diluents. Unlike the rigid particle toughening, organic diluents undergo phase separation upon cooling from initially homogeneous mixtures at high temperatures. In the process of solid-liquid or liquid-liquid phase separation, crystallization of iPP can be affected by the organic diluents that may induce significant changes in materials properties in the solid state. It was shown that phthalic anhydride, for example, can affect the crystallization of iPP and that the resulting properties of solidified composite materials are noticeably different from those of TBBPA/iPP composites. These observations show that organic diluents can modify virgin polymers by traditional mechanisms of rigid particle toughening and/or by chemical interaction with the virgin polymers.

## CHAPTER 4

### THERMALLY ACTIVE COMPOSITE SURFACES USING POLYMER-METAL HYBRID METHODS

Composite surfaces were prepared by wetting of nanoporous alumina templates with polymer melts. Mechanical abrasion was carried out on the surface of polymer/alumina composites at pre-determined temperatures ( $T_0$ ) so that the exposed flat surfaces were composed of a continuous alumina surface with polymer rods confined in the pores of the template with their axis perpendicular to the surface. We proposed that the wetting behavior would be temperature-modulated by the significant difference in thermal expansion behavior between the alumina and the polymer rods. Since the alumina is an excellent thermal conductor with a much smaller coefficient of thermal expansion than polymers, heat can be transferred from the alumina to the polymer efficiently in response to any change in temperature of the material, causing the polymer rods to expand (by heating) or contract (by cooling) more than the alumina does. This differential expansion is demonstrated by two kinds of polymers, fluorinated ethylene propylene copolymer (FEP) and styrene-ethylene/butylene-styrene triblock copolymer (SEBS). At low temperatures ( $T < T_0$ ), the surface property is dominated by the continuous, hydrophilic alumina and the surface shows instantaneous wetting. At high temperatures ( $T > T_0$ ), however, the surface property is governed by the expanded polymer rods and the surface becomes less hydrophilic. The reversibility of the thermal response depends on the properties of the polymers. While the expanded FEP rods do not return to the original state upon cooling, SEBS rods return to their original state.

These observations indicate that the wettability can be controlled by thermal changes using the simple structure of porous alumina filled with polymer rods.

#### **4.1. Introduction**

Interfacial properties, such as wetting behavior, play important roles in a number of scientific and industrial areas such as electronics, printing techniques, microfluidics and biomaterials.<sup>61</sup> While diverse modification procedures have been used for permanent alteration of wettability, control of wettability has also been demonstrated in which reversible control of the surface properties is achieved by photo-illumination, electric potential and thermal change.<sup>62</sup> The basic idea is to control the macroscopic surface properties by modifying the states of the molecules such as self-assembled monolayers (SAMs) or polymers that are confined on the surface. The switching of a SAM-modified surface is usually triggered by a change of molecular conformation in response to an external stimuli. Solid substrates modified by certain photo-, electro- or thermo-switchable polymer molecules have also demonstrated reversible property changes.<sup>63</sup> These strategies, however, require specially designed molecules to achieve the desired functionalities.<sup>64-66</sup>

More convenient preparations of 'smart surfaces' may be found from the well-known structure of nanoporous alumina membranes wetted by organic polymers. Most studies in this field, however, are focused on the fabrication of nano-rods and nano-tubes of polymers, or developing nanostructure induced by phase separation of block copolymers confined in nano-pores, to name a few. In the majority of the relevant work, nanoporous alumina template is removed subsequent to the wetting of the various polymers and analysis has been focused mainly on the nano-structured polymers

obtained. However, the composite structure of alumina and polymer can be utilized for different applications since these two materials have very different properties. One possible way is to use the structure as a composite surface that can react to thermal changes.

In this chapter, polymer-metal hybrid systems prepared by simple wetting of nanoporous alumina substrates with polymer melts are evaluated as composite surfaces that can respond to the external thermal stimuli. Since “high-energy” solids such as metal oxides are wettable by “low-energy” liquids, including polymer melts, any kind of “low-energy” polymers that can flow at elevated temperatures can be used to prepare polymer-metal hybrid systems. Significant difference in thermal conductivity and the coefficient of thermal expansion between the alumina template and the polymer is utilized to control the surface properties by changing the sample temperatures. Switchability and reversibility of the surfaces is investigated using different polymers, fluorinated ethylene propylene copolymer (FEP) and styrene-ethylene/butadiene-styrene triblock copolymer (SEBS). One of the advantages of using nano-scale porous templates is that the alumina template (pore diameter ~ 40 nm, pore-to-pore distance ~ 100 nm) allows fast thermal response time. For example, theoretical calculations based on the thermal properties of each component (alumina and polymer) show that thermal equilibrium can be reached within 10 nano seconds if the surrounding temperature changes from 20 °C to 40 °C.

## 4.2. Materials and Sample Preparation

### 4.2.1. Materials

Aluminum foil (99.99%) was purchased from Alfa Aesar. SEBS (Kraton, G-1657) was a gift from Kraton Polymers. FEP film was purchased from Sigma-Aldrich. Representative materials properties are summarized in Table 4.1.

**Table 4.1.** Materials properties

Properties	Units	Al <sub>2</sub> O <sub>3</sub>	FEP	SEBS
Coefficient of Thermal Expansion	m/(m·°C)	$8.1 \times 10^{-6}$	$1.3 \times 10^{-4}$	$3.0 \times 10^{-4}$
Thermal Conductivity	W/(m·°C)	18	0.2	0.2
Density	g / cm <sup>3</sup>	3.7	2.15	0.9
Melting Temperature	°C	-	270	-

### 4.2.2. Sample Preparation

Nanoporous alumina templates were prepared using a 2-step anodization as described by Masuda et al.<sup>9</sup> High purity aluminum foil (0.25mm thick) was electro-polished in a mixture of HClO<sub>4</sub> / C<sub>2</sub>H<sub>5</sub>OH (1/3) at 5 V for 15 minutes to reduce surface roughness. Anodization was performed in 0.3M oxalic acid solution at 40 V for 3 hours, after which chromic acid solution was used to etch the oxide layer. The second anodization was performed under the same conditions for 24 hours to obtain self-ordered nanoporous alumina with pore diameter of 40 nm (Figure 4.1).

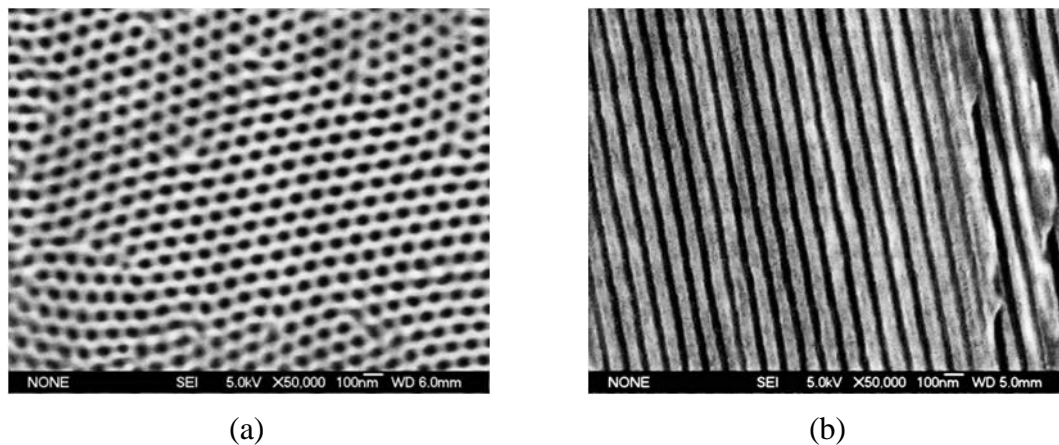


**Figure 4.1.** Morphology of nanoporous alumina templates. (a) top view, (b) side view.

SEBS film was prepared by dissolving SEBS pellets in toluene (10 wt.%), followed by slow evaporation of toluene to yield 250  $\mu\text{m}$  thick films. FEP film (250  $\mu\text{m}$ ) was washed with acetone and dried before use. Each polymer film was placed on top of the alumina template, wrapped with PTFE tape and sealed between two glass plates by clips. Each sample assembly was heated (200  $^{\circ}\text{C}$  for SEBS, 300  $^{\circ}\text{C}$  for FEP) under the vacuum to minimize air entrapment during wetting process and oxidation of the polymer films. Approximately 2 hours was spent for wetting to form polymer rods inside the pores of the alumina template. The pressure was slowly increased to 1 atm by introducing nitrogen gas and the temperature was also slowly decreased to room temperature. Only one of the two porous layers in the alumina template was used for wetting by polymer melt, and the other side was removed using 10% aqueous NaOH solution. Composite surfaces were prepared by pore-opening process using 5%  $\text{H}_3\text{PO}_4$  aqueous solution, followed by mechanical abrasion at several pre-determined temperatures ( $T_0$ ). Figure 4.2 summarizes the procedure.

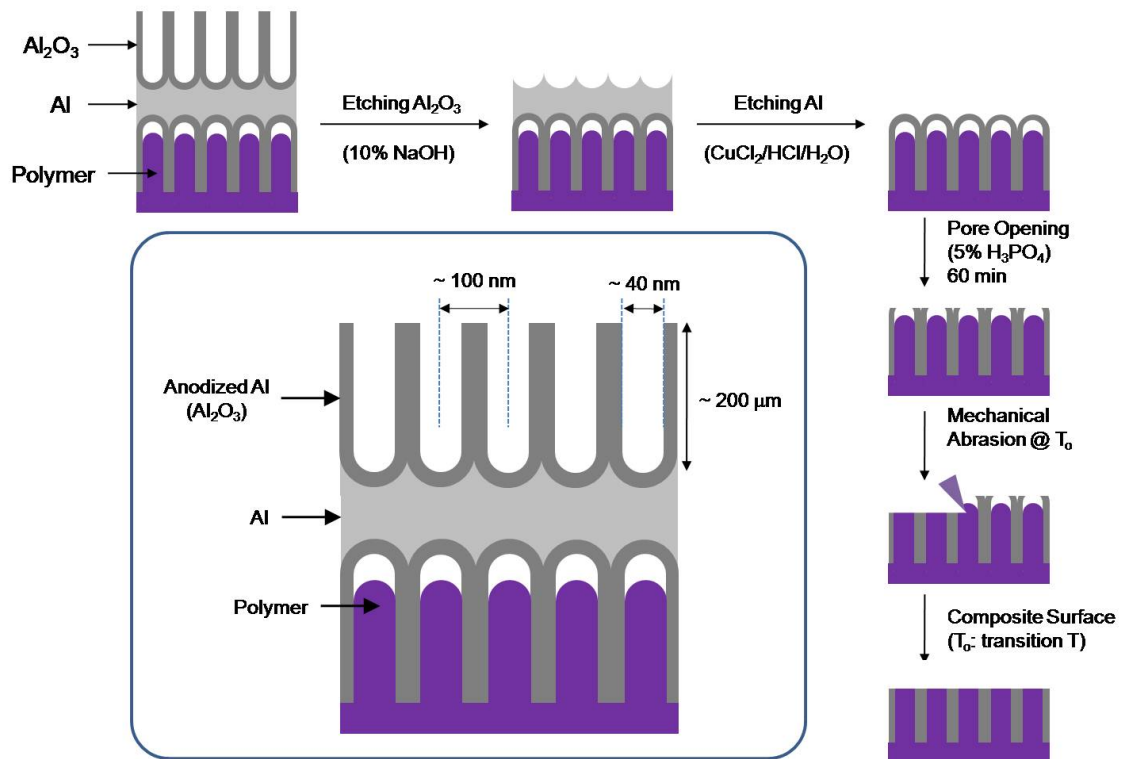


**Figure 4.2.** Scheme for preparing polymer-metal composite surfaces.

### **4.3. Characterization and Testing**

#### **4.3.1. Microscopy**

Scanning electron microscopy (SEM) and atomic force microscopy (AFM) were used to investigate the morphology of composite surfaces. The temperature at which the mechanical abrasion was done ( $T_o$ ) was changed and characterization was performed at room temperature. Three different  $T_o$ 's (0 °C, 20 °C, 40 °C) were selected and mechanical abrasion was executed in ice water (0 °C), at room temperature (20 °C) and in a heated water bath (40 °C) using a series of abrasive papers coated with different size alumina particles (20  $\mu\text{m}$   $\rightarrow$  10  $\mu\text{m}$   $\rightarrow$  5  $\mu\text{m}$   $\rightarrow$  1  $\mu\text{m}$   $\rightarrow$  0.1  $\mu\text{m}$   $\rightarrow$  0.05  $\mu\text{m}$ ).

#### **4.3.2. Contact Angle Measurements**

Surface wettability was characterized by measuring contact angles at different temperatures using a goniometer equipped with a temperature controller. Since the mechanically abraded samples have a significant amount of scratches at the micrometer scale on the surface and failed to produce reliable results, wettability was measured with samples that had undergone the pore-opening process only (Figure 4.2). Large temperature differences were needed to observe the effect of temperature, possibly due to incomplete wetting (filling) of the polymers. Contact angle was measured at 20 °C first, then the temperature was increased to 60 °C for next measurement, after which the temperature was decreased to 20 °C to investigate the reversibility of the thermal response. Advancing contact angles were measured from snapshot images using Image-J software.

## 4.4. Results and Discussion

### 4.4.1. Morphology

Figure 4.3 shows surface morphologies of the composite materials prepared at different abrasion temperatures ( $T_o$ ). When the surface abrasion was performed at 0 °C and temperature was subsequently increased to 20 °C (room temperature), the material undergoes heating and the polymer rods expand more than the alumina template (Figure 4.3a). If the surface abrasion was performed at 40 °C and temperature was subsequently decreased to 20 °C (room temperature), the material undergoes cooling and the polymer rods contract more than the alumina template (Figure 4.3b). Since room temperature (20 °C) abrasion resulted in physically flat surfaces that could not be characterized clearly by SEM, morphology analysis was performed by AFM. Figure 4.3c shows that there is negligible physical roughness (height image), but slight chemical roughness exists as can be seen in the phase image. These observations indicate that the transition temperature ( $T_o$ ) at which the change in surface morphology occurs can be controlled by simply changing the abrasion temperature ( $T_o$ ).

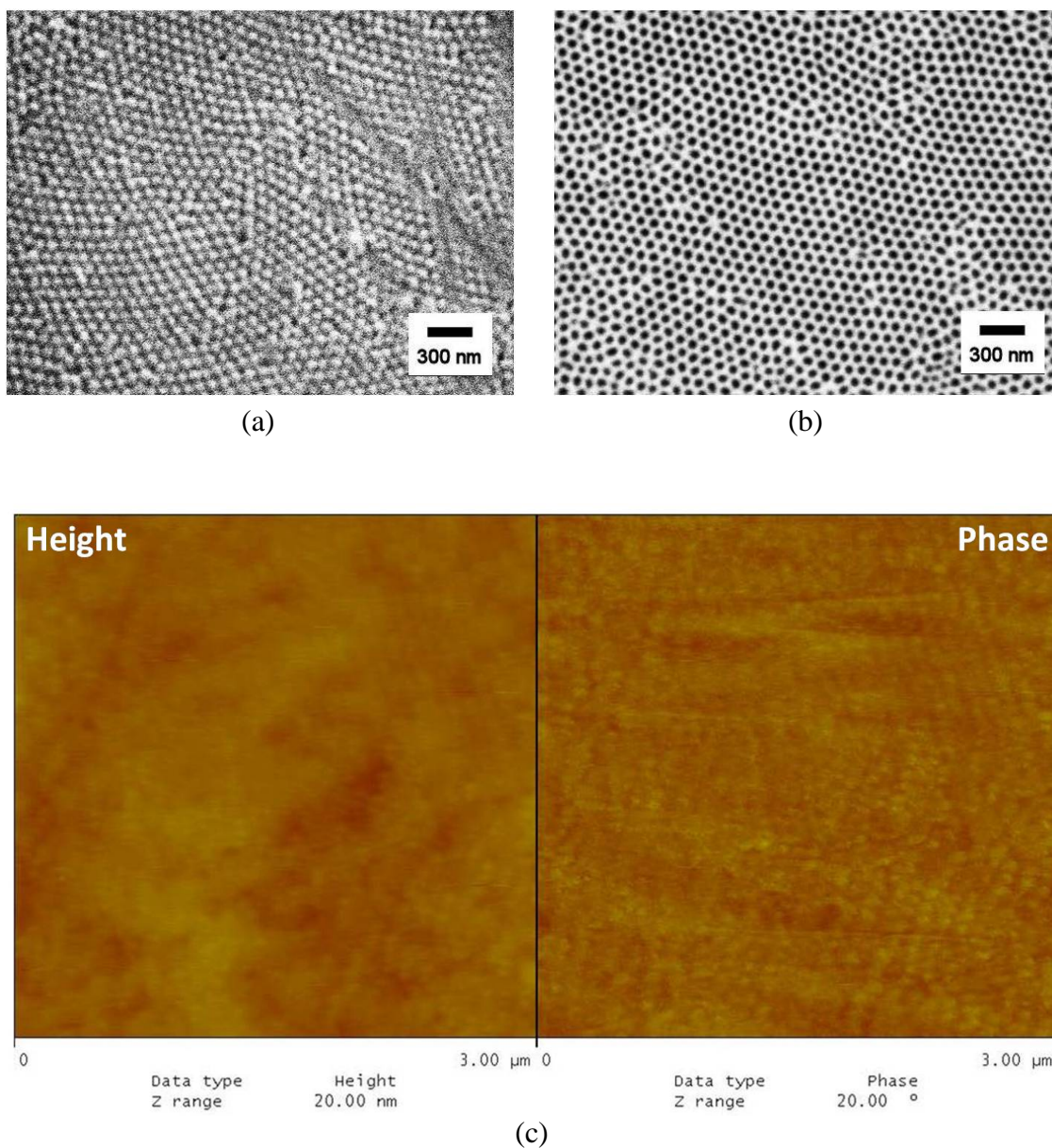
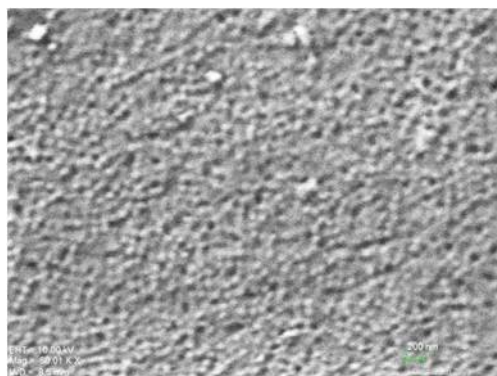
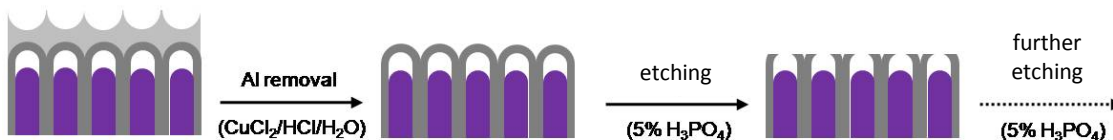


**Figure 4.3.** Surface morphology of composite materials (SEBS in porous alumina template) prepared at different abrasion temperature ( $T_0$ ). (a)  $T_0 = 0$  °C (SEM), (b)  $T_0 = 40$  °C (SEM), (c)  $T_0 = 20$  °C (AFM).

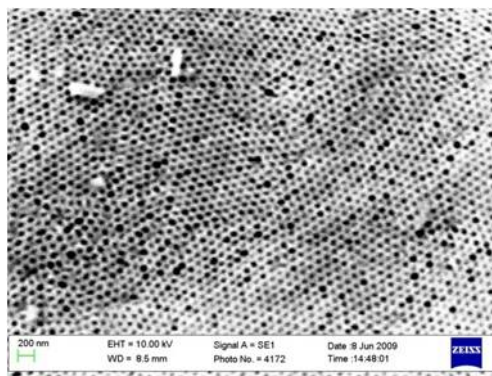
#### 4.4.2. Wettability

Surface properties (wettability) of the composites at different temperatures were probed using a goniometer equipped with a temperature controller and a heating chamber using water as a working fluid. In order to preserve the undamaged surface of alumina template, mechanical abrasion was not done; composite surfaces were prepared by applying 5% phosphoric acid solution at room temperature for 60 minutes to open the pores (Figure 4.2). Incomplete wetting of the polymers was confirmed by empty holes after the sample was soaked in 5% phosphoric acid solution to completely etch the closed end of alumina template (Figure 4.4). After 60 minutes of etching, most of the pores are open (Figure 4.4c). For longer than 60 minutes of etching time, the initially flat alumina surface becomes rough due to excessive etching. However, polymer rods were not seen even after excessive etching, indicating that the polymers did not fill the pores completely. The expected morphology of the sample after the pore-opening step (60 minutes etching in 5% phosphoric acid solution) would exhibit open pores containing incompletely filled polymers inside.

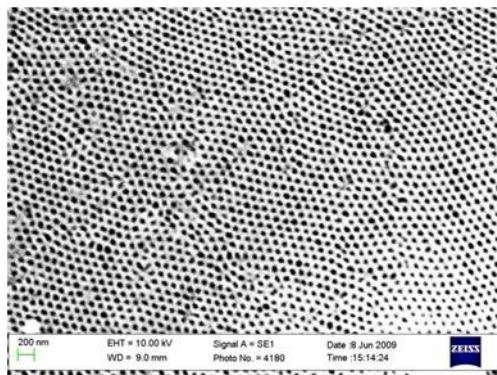
Initial composite surfaces at room temperature were composed of alumina surface containing nano-pores. Since the alumina is hydrophilic, these surfaces exhibit instant wetting at room temperature (Figures 4.5a and 4.5d). When the temperature was increased to 60 °C, polymer rods are expected to expand and protrude above the nanoporous alumina surface. The surface properties should be dictated by these polymer bumps under these conditions. Both FEP/alumina surfaces and SEBS/alumina surfaces show finite advancing angles at 60 °C, indicating that the surfaces are not completely hydrophilic because of the polymer bumps on the surface (Figures 4.5b and 4.5e).



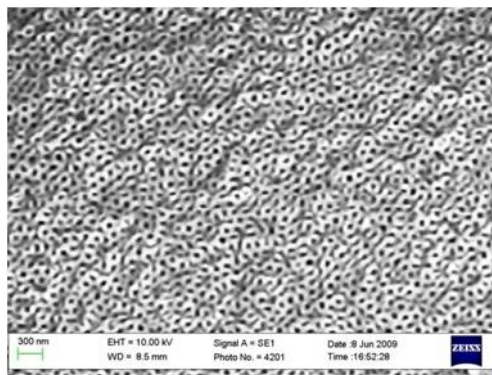
(a)



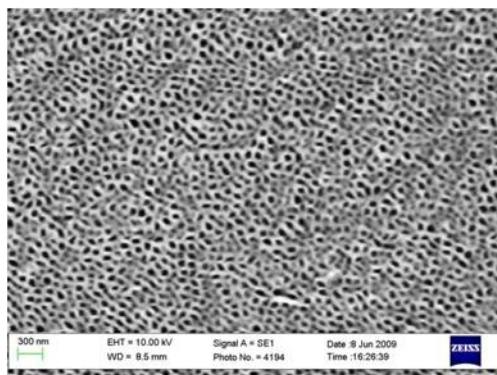
(b)



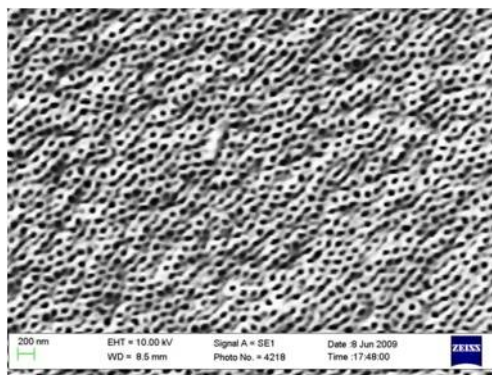
(c)



(d)



(e)



(f)

**Figure 4.4.** Etching of closed-end of alumina template containing polymers inside the pores (pore-opening) using 5% phosphoric acid solution at different etching times. (a) 0 minute, (b) 30 minutes, (c) 60 minutes, (d) 90 minutes, (e) 120 minutes, (f) 150 minutes. After complete removal of the alumina layer, empty holes were observed.

Reversibility of the thermal response was tested by cooling the surface from 60 °C to room temperature and measuring the contact angle again at room temperature. FEP / alumina surfaces show finite advancing angle under these conditions, indicating the expanded FEP rods do not return to their original state upon cooling (Figure 4.5c). SEBS / alumina surfaces, however, show instant wetting, implying that most of the expanded SEBS rods return to their original position (Figure 4.5f). Fluoropolymers, including FEP, are soft materials with very low friction coefficient while SEBS is a highly elastic thermoplastic material. FEP rods can presumably escape from the alumina pores upon heating because of the low friction between the FEP rods and the alumina pores. In contrast, SEBS is a relatively “sticky” material and adheres to the alumina pores more firmly. Upon heating, SEBS rods expand and protrude above the alumina surface, but the SEBS/alumina interface in the pores is still maintained and holds the SEBS rods inside the pores. Upon cooling, SEBS rods contract and return to their original state due to the elastic nature of the material. Although more careful experiments are necessary to confirm this argument, the observation clearly indicates that the reversibility of the thermal response depends on the properties of the polymers (frictional properties and elasticity).

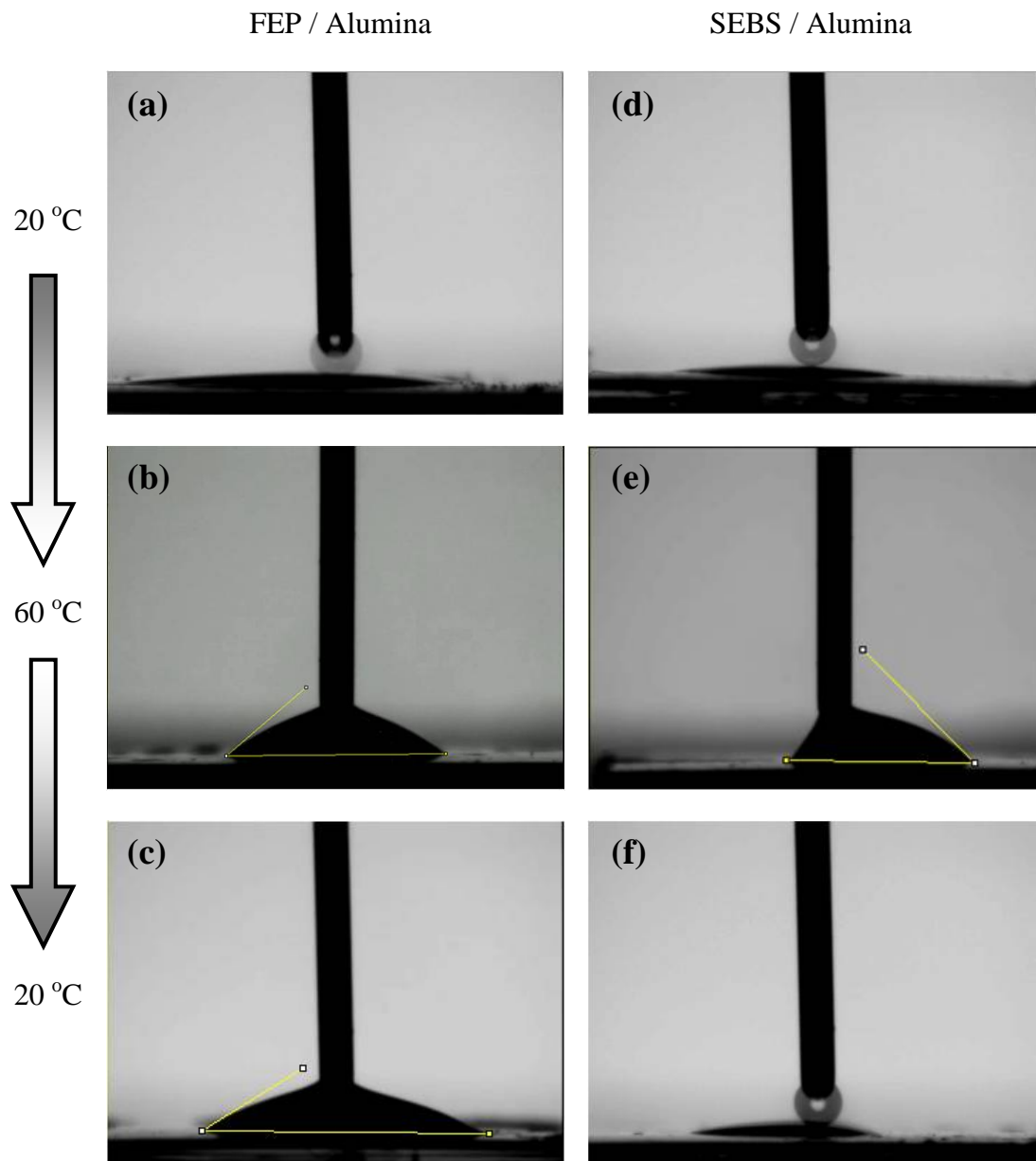


**Figure 4.5.** Contact angles of composite surfaces (FEP/alumina, a-c; SEBS/alumina, d-f) measured at different temperatures. Temperature was changed from 20 °C to 60 °C then returned to 20 °C. (a) FEP/alumina at 20 °C, instant wetting; (b) FEP/alumina at 60 °C,  $\theta_{adv}= 40^\circ$ ; (c) FEP/alumina at 20 °C,  $\theta_{adv}= 32^\circ$ ; (d) SEBS/alumina at 20 °C, instant wetting; (e) SEBS/alumina at 60 °C,  $\theta_{adv}= 44^\circ$ ; (f) SEBS/alumina at 20 °C, instant wetting.

## 4.5. Conclusions

Thermally active composite surfaces were developed using the well-known structure of nanoporous alumina membrane filled with polymers. Unlike more complex methods of preparing such surfaces, the method described in this chapter is relatively simple. The resulting surface can be distinguished from others in some aspects: a practically unlimited number of polymers could be used to prepare thermally functional surfaces, the transition temperature at which the surface properties change can be easily controlled, the response time is predicted to be within a few nano-seconds (depending on the surrounding temperature changes), to name a few.

This concept was demonstrated with a nanoporous alumina template (pore size ~ 40 nm) in combination with either FEP or SEBS. Both polymers showed the expected morphology changes as temperature changed. The surface was composed of alumina with empty holes if the sample temperature was below the pre-determined transition temperature. Expanded polymer bumps were observed on the surface if the sample was subjected to a temperature that was above the transition temperature. When the sample temperature was the same as the transition temperature, the surface was physically almost flat but slight inhomogeneities in chemical composition were detected by AFM. Surface properties (wettability) changed as a function of temperature. Due to experimental difficulties, precise control over the transition temperature could not be demonstrated. The reversibility in thermal response strongly depends on polymer properties. This phenomenon was discussed in terms of polymer properties such as elasticity and friction coefficient.

## APPENDIX

### ALIGNED STRUCTURES USING A HIGH MELTING IONIC LIQUID (MOLTEN SALT) UNDER AN ELECTRIC FIELD

As a simple extension of the work described in Chapter 2, an attempt was made to prepare aligned structures with long-range order using a high melting ionic liquid (1-butyl-4-methylpyridinium chloride) mixed with a compatible polymer (copolymer of vinyl alcohol and ethylene) by cooling the mixtures under an electric field. Thermal analysis of the mixtures showed that the crystallization is suppressed if the composition is close to 1/1 ratio. Crystallinity was observed only if the mixture is either ionic liquid-rich or polymer-rich. Since ordered structure is expected to form by the crystal growth of the ionic liquid under an electric field, ordered structures were observed only in ionic liquid-rich mixtures. These mixtures exhibited sharp increases in electric current under an electric field when the solid samples were melted, likely due to enhanced ionic conductivity in the liquid state. Cross-sections of the solidified samples showed layers of crystals from the ionic liquid. However, reproducibility of such structures was not satisfactory, most likely due to the contamination of the ionic liquid by water during sample preparation steps. Ionic liquids are extremely hygroscopic and easily absorb water from the air. In spite of this practical difficulty, it was demonstrated that long range-ordered structures can be prepared using the high melting ionic liquid under an electric field.

## A.1. Introduction

Ionic liquids, commonly defined as salts that are fluid at near-ambient temperatures (less than  $\sim 100$  °C) and consist of ionic species only, receive keen interest due to their attractive properties such as non-volatility, high ionic conductivity, high polarity and non-flammability.<sup>67-68</sup> They are characterized by weak interactions, owing to the combination of a large cation and a charge-delocalized anion.<sup>69</sup> This results in a low tendency to crystallize due to flexibility (anion) and asymmetry (cation). Their ionic conductivity is comparable to many organic electrolyte solutions with an absence of decomposition or significant vapor pressure up to  $300 \sim 400$  °C. Ionic liquids are basically composed of organic ions that may undergo almost unlimited structural variations because of the easy preparation of a large variety of their components. Thus, various kinds of salts can be used to design the ionic liquid that has the desired properties for a given application.<sup>69</sup> Ionic liquids are particularly useful as substitutes for traditional solvents, most of which are volatile organic compounds (VOCs). Replacement of conventional solvents by ionic liquids would prevent the emission of VOCs, a major source of environmental pollution. Ionic liquids are not intrinsically “green” – some are extremely toxic – but they can be designed to be environmentally benign, with large potential benefits for sustainable chemistry. While there are about 600 molecular solvents in use today, there are potentially at least a million binary ionic liquids and  $10^8$  ternary ionic liquids.<sup>68</sup> This diversity enables the solvent to be designed and tuned to optimize yield, selectivity, substrate solubility, reaction rates and product separation.<sup>70</sup>

If high-melting ionic liquids – a broader definition of an ionic liquid as any salt that melts below the temperature used – are mixed with other compounds, the melting point is depressed to produce liquids with significant ionic character at suitable temperatures. These are known as eutectic mixtures. A particular example of this is hydroxyethyltrimethylammonium chloride (choline chloride, melting point ~ 300 °C) mixture with urea in a 1:2 ratio, that has a melting point of 12 °C.<sup>71</sup> Cooper and coworkers demonstrated that aluminophosphate zeolite analogues could be prepared by using ionic liquids and eutectic mixtures.<sup>67</sup> They used an imidazolium-based ionic liquid which acts as both solvent and template, leading to four zeotype frameworks under different experimental conditions.

These observations in the literature indicate that high melting ionic liquids might be useful for the development of unique morphologies in polymer systems if techniques similar to those described in Chapter 2 are applied. The negligible volatility of ionic liquids would offer excellent thermal stability during thermal mixing step, the ability to form eutectic mixtures with other components would show solid-liquid phase separation as seen in Chapter 2, and the high ionic conductivity would offer additional possibility to control the direction of crystal growth under an external electric field.

In the work described here, eutectic mixtures of a high-melting ionic liquid and a polymer were used to prepare long range-ordered structures by applying an electric field while the mixture underwent phase separation induced by the solidification of the high-melting ionic liquid. It was expected that the crystallization of the ionic liquid would be affected by the electric field due to its high polarity, which would form oriented crystals of ionic liquids in the direction parallel to the electric field.

1-butyl-4-methylpyridinium chloride (melting point ~ 163 °C) and poly (vinyl alcohol-co-ethylene) (melting temperature ~ 167 °C) were used to prepare polymer mixtures. A direct current power supply was used to apply the electric field during solidification of the polymer mixtures. The expected effect of the electric field on the alignment of the ionic component in the mixture is illustrated in Figure A.1. Thermal properties and the morphology of the mixtures were investigated using differential scanning calorimetry (DSC) and field emission scanning electron microscopy (SEM), respectively.

## A.2. Materials and Sample Preparation

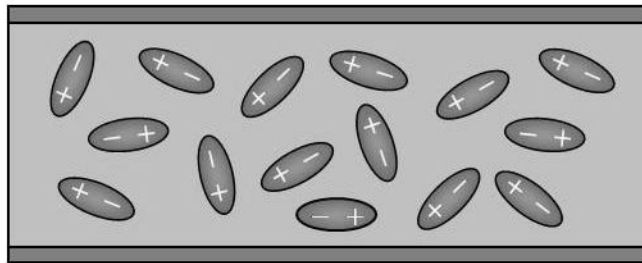
### A.2.2. Materials

Both 1-butyl-4-methylpyridinium chloride and poly (vinyl alcohol-co-ethylene) were purchased from Sigma-Aldrich. Representative properties of the materials are summarized in Table A.1.

**Table A.1.** Materials properties

Properties	Units	1-butyl-4-methylpyridinium chloride	poly (vinyl alcohol-co-ethylene)
Melting Temperature	°C	163	167
Crystallization Temperature	°C	108	144
Glass Transition Temperature	°C	-	55
Ethylene Content	mol %	-	44

(a) unpolarized



(b) Polarized

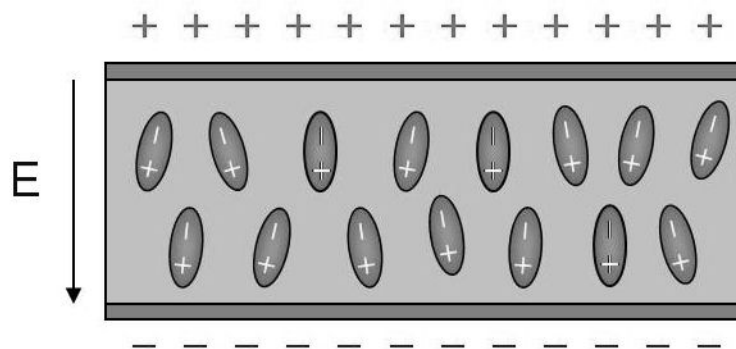


**Figure A.1.** Expected influence of the electric field on the ionic component in the mixture. (a) Without electric field (unpolarized state), (b) With electric field (polarized).

### **A.2.2. Sample Preparation**

Mixtures of the ionic liquid and the polymer were prepared by premixing powders of each component in compositions that ranged from 10 to 90 wt.% ionic liquids at 10 wt.% intervals, followed by thermal mixing at 200 °C for 5 hours in sealed glass vials immersed in an oil bath. After completion of thermal mixing, samples were quenched using liquid nitrogen to prevent macroscopic phase separation. Plaque specimens (10 mm × 10 mm × 0.25 mm) were prepared using compression molding machines as described in Chapter 2. Each plaque specimen was placed between aluminum/Kapton composite films which were connected to the high voltage power supply. Samples were melted inside a convection oven at 200 °C for 5 minutes using nitrogen as a purging gas, and then taken out of the oven for fast cooling. The electric field was applied during melting and cooling steps. Figure A.2 shows the schematics of the sample preparation used in this work.

### **A.3. Characterization**

Similar characterization methods as described in Chapter 2 were used. Thermal properties were measured by differential scanning calorimetry (DSC) at 10 °C/min. Morphology of the cross-section of the samples was investigated by field emission scanning electron microscopy (SEM).

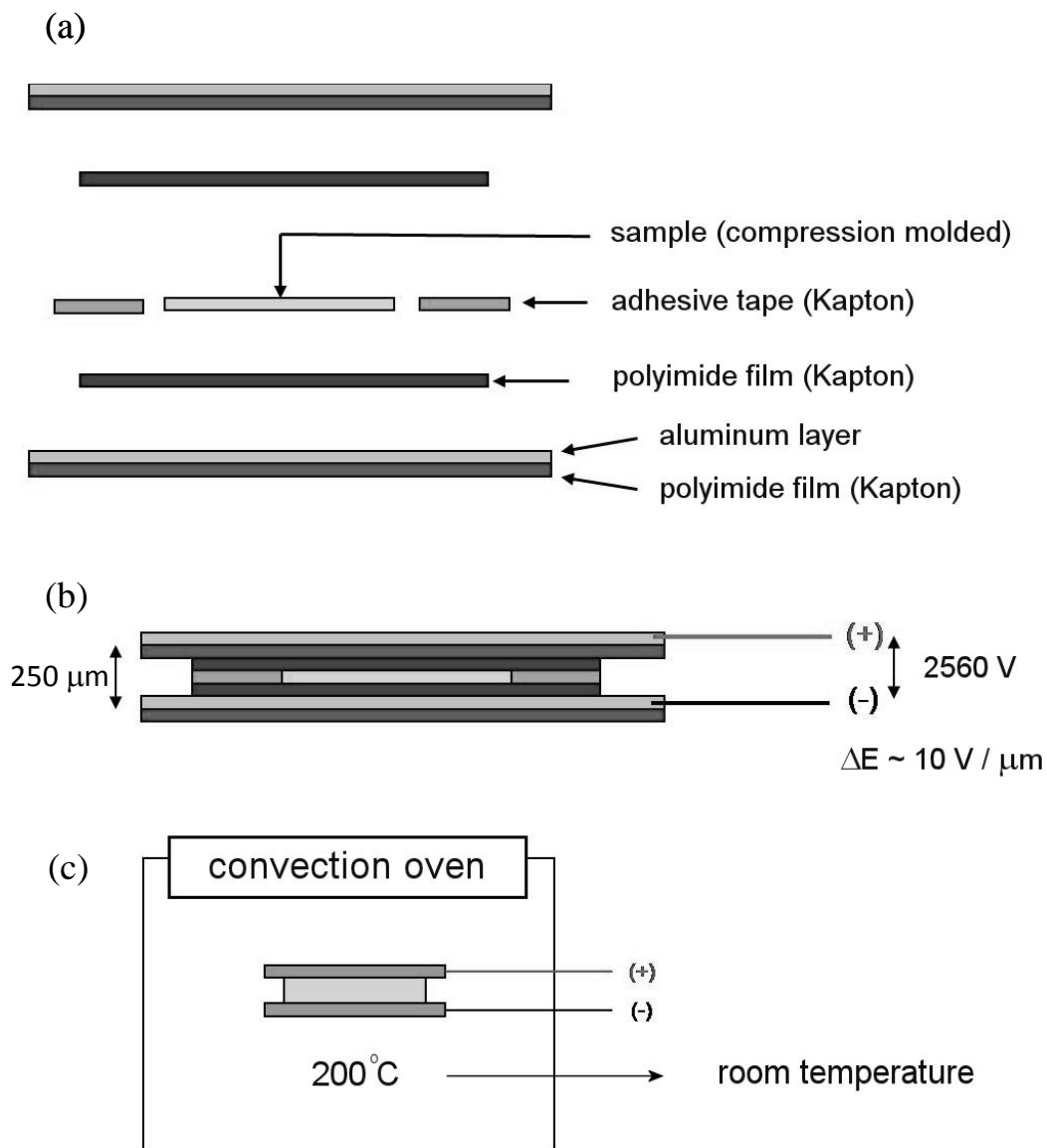


**Figure A.2.** Schematic description of sample preparation. (a) sample is sealed between the Kapton films and then placed between the aluminum/Kapton composite films, (b) positive and negative poles from the high voltage generator are connected to the aluminum layers of the composite films, (c) electric field is applied while the sample is melted inside the convection oven at 200 °C for 5 minutes and cooled at room temperature.

## A.4. Results and Discussion

### A.4.1. Thermal Properties

DSC thermograms of the mixtures are shown in Figure A.3 and the melting temperatures (taken from the peak maxima) as well as the glass transition temperatures (taken from the mid-point of the two inflection points) are shown in Figure A.4.

Melting temperatures of the mixtures show a decreasing trend compared with those of pure components, which is a characteristic behavior of eutectic mixtures (Figure A.4a). Melting temperature depression is more significant in the polymer-rich regime, which can be understood in the same way as discussed in Chapter 2. However, melting peaks were not observed if the composition of the mixture is close to 50% of ionic liquid / 50% of polymer. In fact, if the polymer content in the mixture is between 40% and 60%, no melting peaks were observed (Figure A.3). The reason for this observation is not clear. However, there is a possibility that each component might hinder the crystallization of the other component due to potential ionic interaction between the ionic liquid and the polar polymer. If one component exists in excess, part of that component might interact with the other component and fail to crystallize, but the remaining amount of that component can still be crystallized. This reasoning can explain the change in melting temperatures of the mixture. However, further work is required to understand this phenomenon clearly.

Glass transition temperatures ( $T_g$ ) of the mixtures decrease as the ionic liquid content in the mixture increases (Figure A.4b). This indicates that the ionic liquid functions as a plasticizer for the polymer, as reported by other investigators.<sup>72-73</sup>

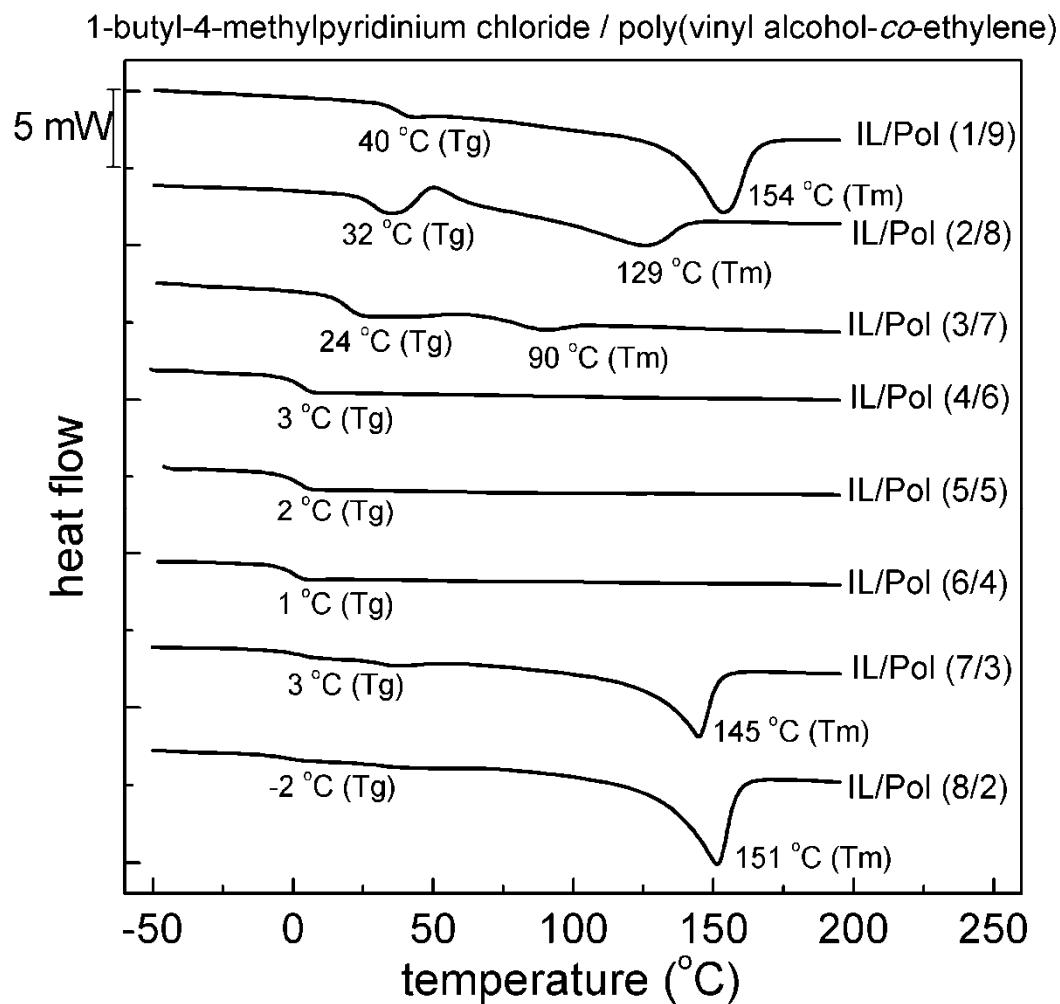


**Figure A.3.** DSC thermograms of the ionic liquid / polymer mixtures as measured by heating at 10 °C/min. IL stands for ionic liquid and Pol stands for polymer.

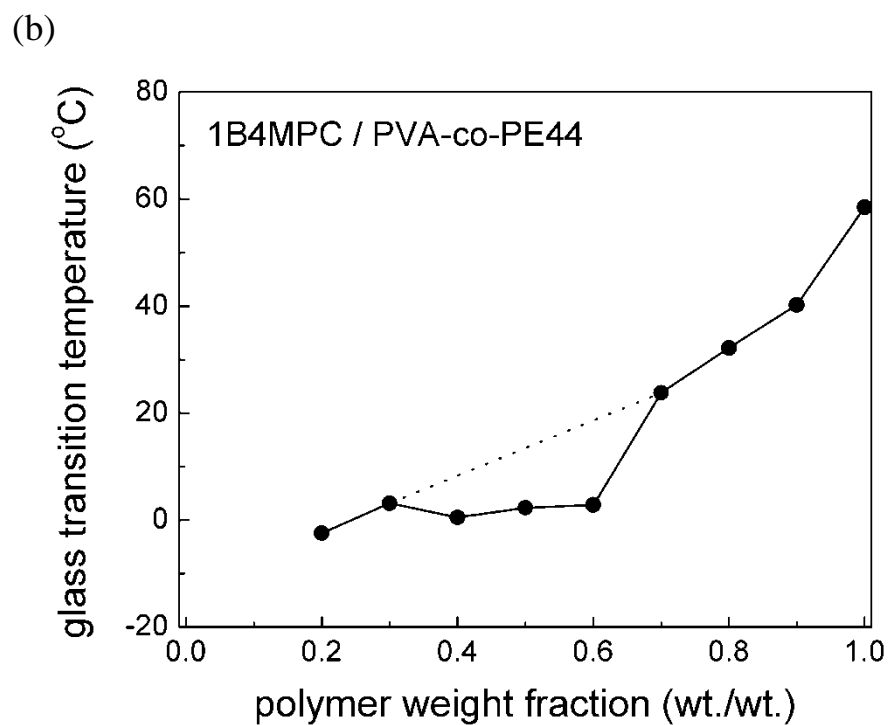
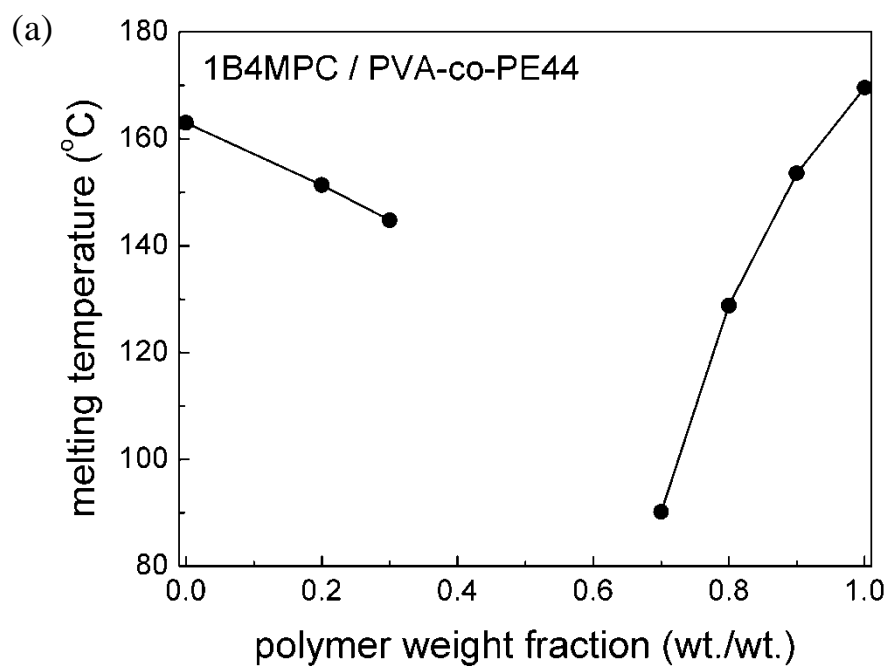


**Figure A.4.** (a) melting temperatures of the mixtures, (b) glass transition temperatures of the mixtures.

#### **A.4.2. Effect of Electric Field on the Morphology**

The response of the samples to the electric field and the resulting morphology were observed under selected electric field strengths (0 V/ $\mu\text{m}$ , 0.1 V/ $\mu\text{m}$  and 10 V/ $\mu\text{m}$ ). Due to the relatively weak interactions between the anion and cation in ionic liquids, electric field strength would have important effect on the morphology of the mixtures. If the electric field is weak, crystallization of ionic liquid molecules would not be affected. If, however, the electric field is strong, segregation between anions and cations may occur and crystallization of the ionic liquid may be suppressed. The viscosity of the polymer systems should also be considered since the mobility of the crystallizing ionic liquid in the polymeric medium is expected to be affected by the viscosity of the system.

When no electric field or a low strength electric field (0.1 V/ $\mu\text{m}$ ) was applied during the sample (ionic liquid / polymer = 80 / 20) preparation step (melting and cooling with a compression molding machine under electric field), the direct current power supply showed no change in electric current value. However, a change in electric current value was observed when high strength electric field (10 V/ $\mu\text{m}$ ) was applied. Figure A.5 shows the change in temperature and electric current as a function of time during melting and cooling under an electric field of 10 V/ $\mu\text{m}$ . A room temperature sample was introduced into the compression molding machine maintained at 200 °C at  $t = 0$  sec. It takes time ( $\sim 50$  sec) for the temperature of the sample to increase to its melting temperature. While the mixture is in the solid state, electric current did not change. However, an abrupt increase in current was observed after 50 seconds from the initial introduction of the sample into the compression molder. The temperatures of both

upper and lower plates of the compression molding machine initially decreased due to the contact with the cold sample, but then began to increase after ~ 50 seconds, at which point the electric current abruptly increased. This indicates that the mixture was melted at that point and ionic conduction occurred in the liquid state (Figure A.5a). The current was maintained at the elevated value while the mixture is in the liquid state. When the sample was subject to cooling, the electric current decreased as the temperature of the sample decreased (Figure A.5b), although the applied electric field strength was not changed. This implies that the ionic flow is strongly affected by the physical state of the ionic liquid (mobile liquid or immobile solid) and/or the viscosity of the sample that affects the mobility of the ionic liquid.

When the ionic liquid content in the mixture was decreased, the change in electric current also decreased. Virtually no change in electric current was observed when the ionic liquid content was below 60 wt.%. It seems that there is a minimum concentration of ionic liquid below which electric field would not be effective for the mixtures used in this study.

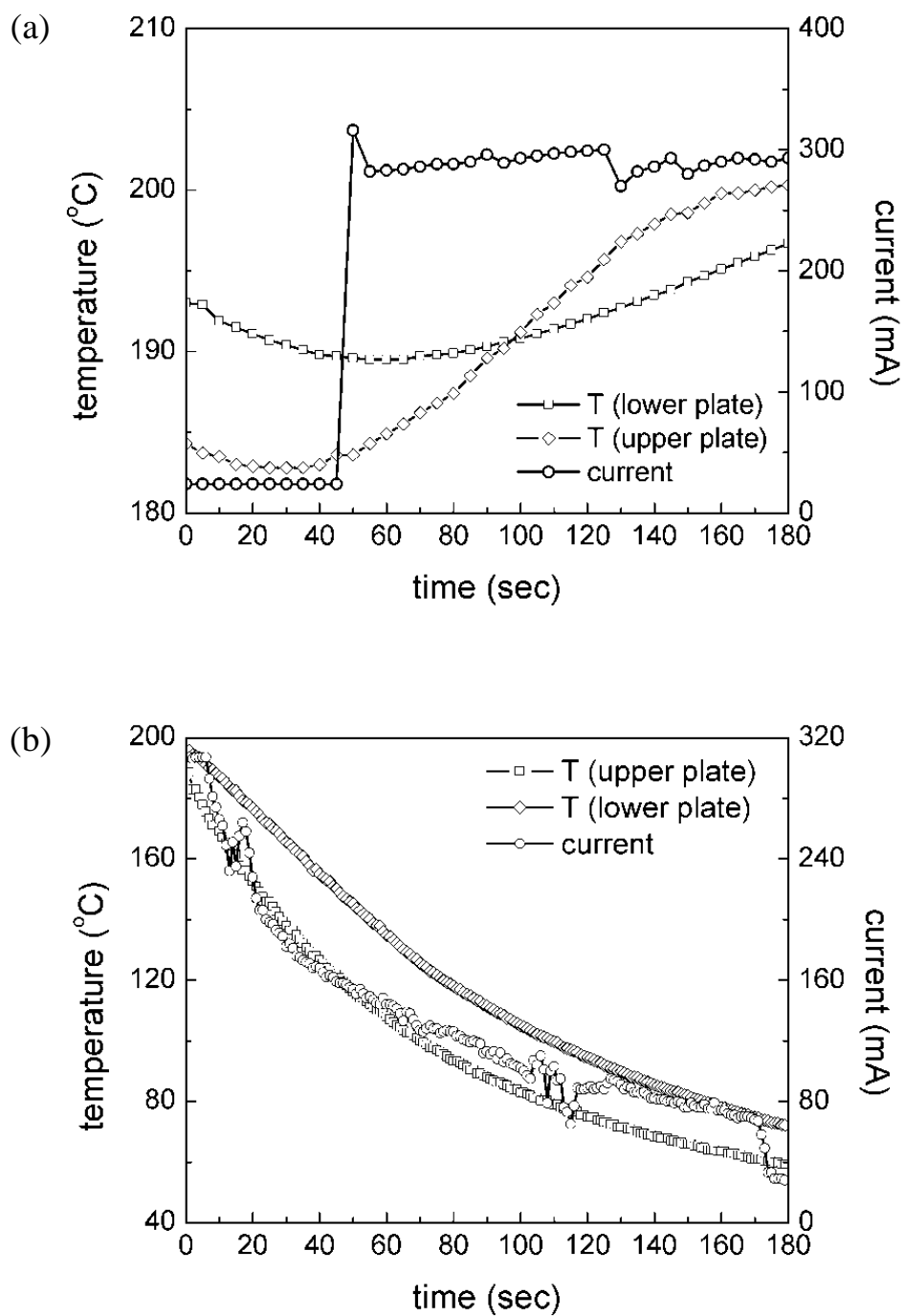


**Figure A.5.** Change in temperature and electric current during melting and cooling of the samples under the influence of  $10 \text{ V}/\mu\text{m}$  of electric field. The mixture was composed of 80 wt.% ionic liquid and 20 wt.% polymer. (a) melting, (b) cooling.

The morphology of the solidified samples was examined by SEM. Each sample was immersed in liquid nitrogen for 3 minutes before being cut with a sharp razor blade. Figure A.6 shows that an aligned structure was produced under the electric field when the initial composition of the mixture was highly ionic liquid-rich (~ 80 wt.%). When the ionic content was decreased to 70 wt.%, an aligned structure was still observed but the alignment was less perfect (Figure A.6b). The effect of the electric field was apparently lost when the ionic content in the mixture was below 60 wt.%. DSC thermograms (Figure A.3) show that crystalline ionic liquid exists if its content in the mixture is 70 wt.% or higher. Crystallization of the ionic liquid in the mixture occurs in this composition regime and the electric field affects the crystallization. If the ionic liquid content in the mixture was in the range between 40 wt.% and 60 wt.%, crystallinity of the mixture was essentially absent. Since the crystallization of the ionic liquid is suppressed in this composition regime, aligned structure induced by the crystal growth of the ionic liquid is not likely to occur. If the composition of the mixture was polymer-rich (polymer content in the mixture is 70 wt.% or higher), crystallization of polymer would occur but that of ionic liquid would not occur. In this case, aligned structure due to the crystallization of ionic liquid is not expected. These observations indicate that aligned structure can be obtained from the mixtures of high melting ionic liquids and compatible polymers under an electric field if the initial composition of the mixture is highly ionic liquid-rich.

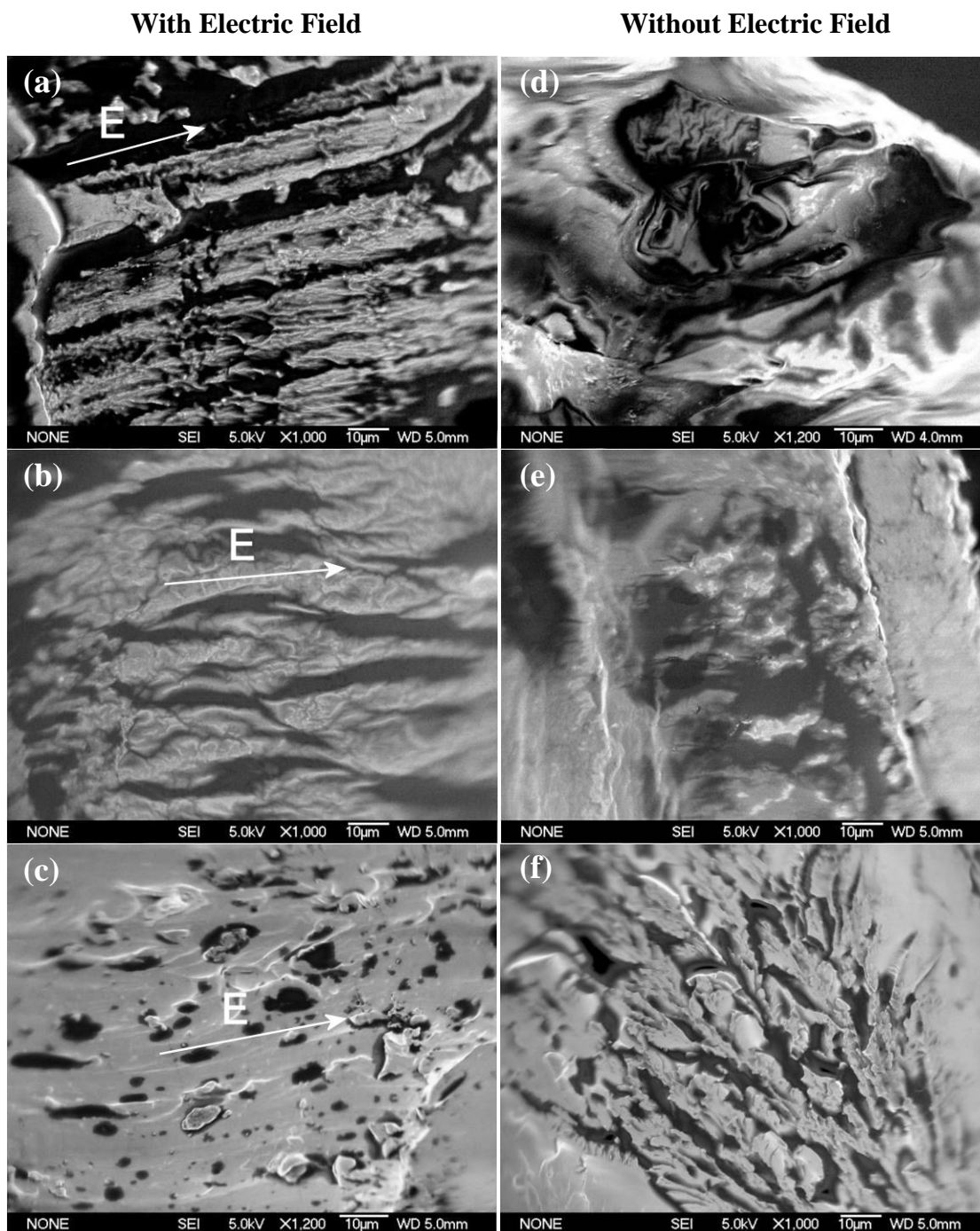


**Figure A.6.** Morphology of the cross-sections of the solidified mixtures prepared with an electric field (a – c) and without an electric field (d – f). The strength of electric field was  $10 \text{ V}/\mu\text{m}$ . (a) ionic liquid / polymer: 8/2, (b) ionic liquid / polymer: 7/3, (c) ionic liquid / polymer: 5/5, (d) ionic liquid / polymer: 8/2, (e) ionic liquid / polymer: 7/3, (f) ionic liquid / polymer: 5/5.

It should be noted that reproducibility of the ordered structure was not satisfactory. Even if the sample composition and the strength of the electric field were set properly to produce aligned structures, disordered morphologies were observed in some cases. The reason for this is not clear, but one possibility is the water contamination of the ionic liquid during sample preparation step. Most ionic liquids, including the one used in this work, are extremely hygroscopic. Figure A.7 shows TGA thermogram of the ionic liquid used in this work, which was exposed in the air for less than one minute while the sample was placed inside the heating chamber of the TGA. The temperature was increased to 100 °C at 10 °C/min and held for 10 minutes. Mass change of the ionic liquid shows that the sample contained about 10 wt.% of volatile material which evaporated below 100 °C. This indicates that drying of ionic liquid would be crucial to avoid water contamination especially when the intended application of the ionic liquid is potentially affected by the existence of water in the system.

#### **A.5. Conclusions**

It was demonstrated that long range-ordered structures could be produced using a high melting ionic liquid mixed with a compatible polymer under an electric field. High concentration ionic liquid (70 wt.% or above) and a strong electric field ( $\sim 10 \text{ V}/\mu\text{m}$ ) were required to obtain such structures. Under these conditions, crystals of ionic liquid aligned in the direction parallel to the applied electric field were observed. If the electric field was not applied or the concentration of the ionic liquid was below 70 wt.%, a disordered structure was observed. This result shows that high melting ionic liquids are potentially useful to control the morphology of polymer systems.

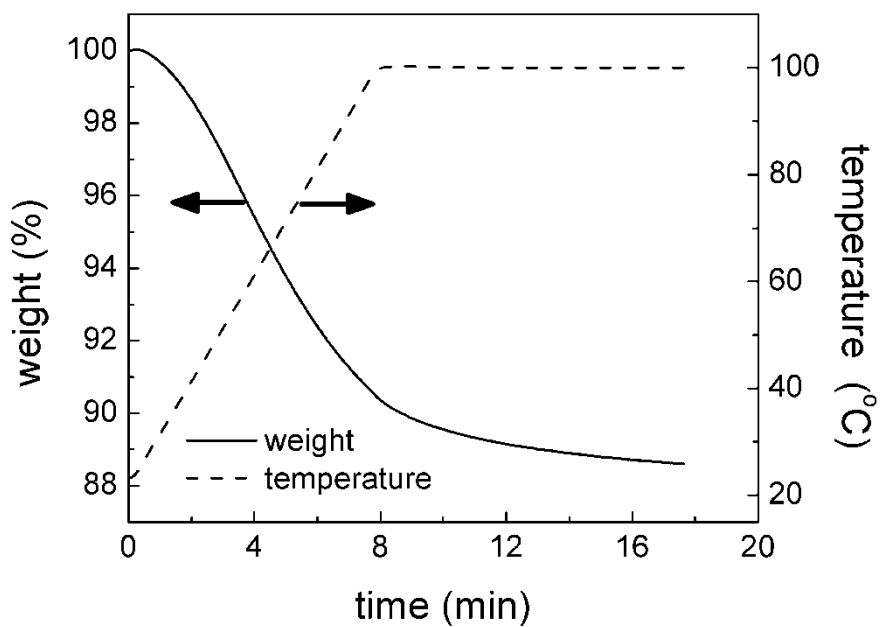


**Figure A.7.** TGA thermogram of pure 1-butyl-4-methylpyridinium chloride. Sample was exposed to air for less than one minute while being placed inside the TGA chamber.

## A.6. Future Work

This work was an initial attempt to use a high melting ionic liquid as a structure-directing agent under an electric field. While there is significant work in the literature describing the use of ionic liquids as a replacement for traditional solvents<sup>68, 74</sup> and as a new type of plasticizers,<sup>72</sup> there has not been attempts to use ionic liquids to develop ordered structures of polymer systems. High ionic conductivity and high polarity of the ionic liquids are potentially beneficial to induce long range-ordered structures under external fields.

It was found that the resulting structure depends strongly on the composition of the polymer systems, the interaction between the ionic liquid and the polymer, the strength of the electric field and presumably water contamination of the ionic liquids. A systematic study to optimize the strength of the electric field for selected polymer-ionic liquid mixtures could be done in the future. Due to the potential ionic interaction between the polar polymer and the ionic liquid that is likely to affect the phase transition of such systems, careful study to investigate the phase separation process should be done. A more efficient way to avoid potential water contamination of the ionic liquid should be found.

## BIBLIOGRAPHY

1. Callister, W. D., *Fundamentals of Materials Science and Engineering*. John Wiley & Sons, Inc: New York, 2001.
2. Burghardt, W. R. *Macromolecules* **1989**, 22, 2482-2486.
3. Flory, P. J., *Principles of Polymer Chemistry*. Cornell University Press: Ithaca, NY, 1953.
4. Mandelkern, L., *Crystallization of Polymers*. 2nd ed.; Cambridge University Press: Cambridge, 2002.
5. Young, R. J.; Lowell, P. A., *Introduction to Polymers*. 2nd ed.; Chapman & Hall: London, 1991.
6. Wu, S. *J. Appl. Polym. Sci.* **1988**, 35, 549-561.
7. Li, A. P.; Muller, F.; Birner, A.; Nielsch, K.; Gosele, U. *J. Appl. Phys.* **1998**, 84, (11), 6023-6027.
8. Thompson, G. E.; Wood, G. C. *Nature* **1981**, 290, 230-232.
9. Masuda, H.; Fukuda, K. *Science* **1995**, 268, 1466-1468.
10. Kim, S. J.; Lim, J. H.; Choi, J. S. *Polym. Sci. Tech.* **2006**, 17, (6), 742-751.
11. Jessensky, O.; Muller, F.; Gesele, U. *Appl. Phys. Lett.* **1998**, 72, (10), 1173-1175.
12. Nielsch, K.; Choi, J.; Schwirn, K.; Wehrspohn, R. B.; Gesele, U. *Nano Lett.* **2002**, 2, 677-680.
13. Moon, S. I.; McCarthy, T. J. *Macromolecules* **2003**, 36, 4253-4255.
14. Xiang, H.; Shin, K.; Kim, T.; Moon, S. I.; McCarthy, T. J.; Russell, T. P. *Macromolecules* **2004**, 37, 5660-5664.
15. Shin, K.; Xiang, H.; Moon, S. I.; Kim, T.; McCarthy, T. J.; Russell, T. P. *Science* **2004**, 306, 76.
16. Steinhart, M.; Wendorff, J. H.; Greiner, A.; Wehrspohn, R. B.; Nielsch, K.; Schilling, J.; Choi, J.; Gesele, U. *Science* **2002**, 296, 1997.
17. Xiang, H.; Shin, K.; Kim, T.; Moon, S. I.; McCarthy, T. J.; Russell, T. P. *Macromolecules* **2005**, 38, 1055-1056.
18. deGennes, P. G. *Rev. Modern Phys.* **1985**, 57, (3), 827-863.

19. Zhang, M.; Dobriyal, P.; Chen, J. T.; Russell, T. P. *Nano Lett.* **2006**, 6, (5), 1075-1079.
20. Steinhart, M.; Wehrspohn, R. B.; Gesele, U.; Wendorff, J. H. *Angew. Chem.* **2004**, 43, 1334-1344.
21. Lloyd, D. R.; Kinzer, K. E.; Tseng, H. S. *J. Membrane Sci.* **1990**, 52, 239-261.
22. Matsuyama, H.; Teramoto, M.; Kudari, S.; Kitamura, Y. *J. Appl. Polym. Sci.* **2001**, 82, 169-177.
23. Kim, W. K.; Char, K.; Kim, C. K. *J. Polym. Sci., Part B: Polym. Phys.* **2000**, 38, 3042-3052.
24. Witte, P. V. d.; Dijkstra, P. J.; Berg, J. W. A. V. d.; Feijen, J. *J. Membrane Sci.* **1996**, 117, 1-31.
25. Matsuyama, H.; Yuasa, M.; Kitamura, Y.; Teramoto, M.; Lloyd, D. R. *J. Membrane Sci.* **2000**, 179, 91-100.
26. Matsuyama, H.; Berghmans, S.; Batarseh, M. T.; Lloyd, D. R. *J. Membrane Sci.* **1998**, 142, 27-42.
27. Narkis, M.; Siegmann, A.; Puterman, M.; DiBenedetto, A. T. *J. Polym. Sci., Polym. Phys. Ed.* **1979**, 17, 225-234.
28. Smith, P.; Pennings, A. J. *J. Polym. Sci., Polym. Phys. Ed.* **1977**, 15, 523-540.
29. Smith, P.; Pennings, A. J. *Polymer* **1974**, 15, 413-419.
30. Alwattari, A. A.; Lloyd, D. R. *J. Membrane Sci.* **1991**, 64, 55-68.
31. Kitaigorodsky, A. I., *Molecular Crystals and Molecules*. Academic Press: New York, 1973.
32. Glusker, J. P.; Lewis, M.; Rossi, M., *Crystal Structure Analysis for Chemists and Biologists*. VCH Publishers: New York, 1994.
33. Brandrup, J.; Immergut, E. H.; Grulke, E. A., *Polymer Handbook*. 4th ed.; Wiley: New York, 1999.
34. Dobbs, J. M.; Wong, J. M.; Johnston, K. P. *J. Chem. Eng. Data* **1986**, 31, 303-308.
35. Poerschmann, J.; Kopinke, F. D. *Environ. Sci. Tech.* **2001**, 35, 1142-1148.
36. Barton, A. F. M., *CRC Handbook of Polymer-Liquid Interaction Parameters and Solubility Parameters*. CRC Press: 1990.

37. Chadwick, G. A., *Metallography of Phase Transformations* Butterworths: London, 1974.
38. Chalmers, B., *Principles of Solidification*. John Wiley & Sons: New York, 1964.
39. Vicsek, T. *Phys. Rev. Lett.* **1984**, 53, (24), 2281-2284.
40. Langer, J. S. *Rev. Mod. Phys.* **1980**, 52, 1.
41. Witten, T. A.; Sander, L. M. *Phys. Rev. Lett.* **1981**, 47, 1400.
42. Mullin, J. W., *Crystallization*. 4th ed.; Elsevier: London, 2001.
43. Bucknall, C. B., *Toughened Plastics*. Applied Science Publishers: London, 1977.
44. Kinloch, A. J.; Young, R. J., *Fracture Behavior of Polymers*. Applied Science Publishers: London, New York, 1983.
45. Liang, J. Z.; Li, R. K. Y. *J. Appl. Polym. Sci.* **2000**, 77, 409-417.
46. Lazzeri, A.; Bucknall, C. B. *J. Mater. Sci.* **1993**, 28, 6799.
47. Lazzeri, A.; Bucknall, C. B. *Polymer* **1995**, 36, 2895.
48. Bartczak, Z.; Argon, A. S.; Cohen, R. E.; Weinberg, M. *Polymer* **1999**, 40, 2347-2365.
49. Thio, Y. S.; Argon, A. S.; Cohen, R. E.; Weinberg, M. *Polymer* **2002**, 43, 3661-3674.
50. Muratoglu, O. K.; Argon, A. S.; Cohen, R. E.; Weinberg, M. *Polymer* **1995**, 36, 921-930.
51. Bartczak, Z.; Argon, A. S.; Cohen, R. E.; Weinberg, M. *Polymer* **1999**, 40, 2331-2346.
52. Bartczak, Z.; Argon, A. S.; Cohen, R. E.; Kowalewski, T. *Polymer* **1999**, 40, 2367-2380.
53. Wilbrink, M. W. L.; Argon, A. S.; Cohen, R. E.; Weinberg, M. *Polymer* **2001**, 42, 10155-10180.
54. Lesser, A. J.; McCarthy, T. J.; Yoon, J.; Yordem, O. S. 12/057850, 2008.
55. Yoon, J.; McCarthy, T. J.; Lesser, A. J. In SPE Antec, Milwaukee, 2008; Milwaukee, 2008; pp 6-10.

56. Barton, A. F. M., *CRC Handbook of Solubility Parameters and Other Cohesion Parameters*. 2nd Ed. ed.; CRC Press Inc.: 1991.
57. Hansen, C. M. *Prog. Org. Coat.* **2004**, 51, 109-112.
58. Sue, H. J.; Pearson, R. A.; Parker, D. S.; Huang, J.; Yee, A. F. *ACS Div. Polym. Chem. Polym. Prep.* **1998**, 29, 147.
59. Zhao, S.; Cai, Z.; Xin, Z. *Polymer* **2008**, 49, 2745-2754.
60. Landes, J. D.; Begley, J. A. *ASTM STP* **1977**, 632.
61. Isaksson, J.; Tengstedt, C.; Fahlman, M.; Robinson, N.; Berggren, M. *Adv. Mater.* **2004**, 16, (4), 316-320.
62. Lahann, J.; Mitragotri, S.; Tran, T.; Kaido, H.; Sundaram, J.; Choi, I. S.; Hoffer, S.; Somorjai, G. A.; Langer, R. *Science* **2003**, 299, 371-374.
63. Crevoisier, G. D.; Fabre, P.; Corpart, P. F.; Leibler, L. *Science* **1999**, 285, 1246-1249.
64. Isaksson, J.; Robinson, N. D.; Berggren, M. *Thin Solid Films* **2006**, 515, 2003-2008.
65. Abbott, N. L.; Gorman, C. B.; Whitesides, G. M. *Langmuir* **1995**, 11, (1), 16-18.
66. Liu, Y.; Mu, L.; Liu, B.; Zhang, S.; Yang, P.; Kong, J. *Chem. Commun.* **2004**, 1194-1195.
67. Cooper, E. R.; Andrews, C. D.; Wheatley, P. S.; Webb, P. B.; Wormald, P.; Morris, R. E. *Nature* **2004**, 430, (26), 1012-1016.
68. Rogers, R. D.; Seddon, K. R. *Science* **2003**, 302, 792-793.
69. Armand, M.; Endres, F.; MacFarlane, D. R.; Ohno, H.; Scrosati, B. *Nat. Mater.* **2009**, 8, 621-629.
70. Freemantle, M. *Chem. Eng. News* **1998**, 76, 32.
71. Abbott, A. P.; Capper, G.; Davies, D. L.; Rasheed, R. K.; Tambyrajah, V. *Chem. Commun.* **2003**, 70-71.
72. Scott, M. P.; Brazel, C. S.; Benton, M. G.; Mays, J. W.; Holbrey, J. D.; Rogers, R. D. *Chem. Commun.* **2002**, 1370-1371.
73. Rahmana, M.; Brazel, C. S. *Polym. Degrad. Stab.* **2006**, 91, (12), 3371-3382.
74. Wilkes, J. S. *Green Chem.* **2002**, 4, 73-80.